Fundamental properties of graphene hybrid structures

Hideyuki Jippo

Doctoral Program in Nano-Science and Nano-Technology

Submitted to the Graduate School of

Pure and Applied Sciences

in Partial Fulfillment of the Requirements

for the Degree of Doctor of Philosophy in

Science

at the

University of Tsukuba

Abstract

Graphene has attracted much attention in the field of nanoelectronics because of its unique electronic and geometric properties. A honeycomb network with atom thickness leads to massless electron/hole around the Fermi level that allow the material to be applied to high-speed electronic devices in the post-silicon era. On the other hand, electronic properties of graphene are fragile against the other foreign materials, such as metal electrodes and insulating substrates, because the electron system of graphene is distributed normal to their atomic network that intrinsically form interfaces with such foreign materials.

High contact resistance between graphene and metal electrodes is one of the serious issues for designing graphene-based electronic devices. In addition to the high contact resistance, it has been experimentally reported that the resistance also depends on the metal species and the process conditions. Several theoretical studies reported geometries, electronic structures, and transport properties of interfaces between graphene and metal surfaces. Although much effort has been devoted to unravel the fundamental properties of interfaces, the comprehensive understanding has not yet been achieved. Therefore, this is motivating us to gain theoretical insight into the fundamental properties at the interface between graphene and metal electrodes for realizing graphene-based electronic devices.

This fragility of electronic structure of graphene on the insulating substrates is another serious problem. Experiments have shown the degradation of the carrier mobility and the variation of the transport properties of graphene adsorbed on SiO_2. The surface treatment of SiO_2 even changes the electronic transport properties of graphene. From a theoretical perspective, several studies on the geometrical and electronic properties of graphene on SiO_2 have been reported using first-principles methods. However, a theoretical study of the electronic transport properties of graphene on SiO_2 has not been reported.

In this thesis, we study electronic transport properties of armchair graphene nanoribbons (AGNRs) bridged between two Au electrodes using first-principles calculations. The transport properties sensitively depend on the ribbon width, even though the ribbon width reaches 12 nm. The variation of transport properties is ascribed to the detailed electronic structure of AGNRs, which sensitively depend on their width.

We have also found that the energy band structure and the symmetry of π states of the AGNRs play the important role for determining the transport properties. We also investigate transport properties of the hybrid structures of graphene/Ti electrodes.

We also study the electronic transport properties of AGNRs on SiO_2/Si using first-principles calculations. Models with channel lengths of 9.91 and 15.1 nm are examined and compared. We also investigate the differences in the electronic transport properties between OH- and O-terminated SiO_2 surfaces. The AGNRs show *p*-type conducting properties on the SiO_2/Si surfaces. Regardless of the channel length, the on/off current ratio is 10^5 for the AGNRs on O-terminated surface. This ratio is consistent with recent experiments and smaller by factors of 10^8 for the 9.91 nm channel length and 10^{15} for the 15.1 nm channel length compared to our results for freestanding AGNRs. For AGNRs on OH-terminated SiO_2/Si, even smaller on/off ratio is obtained on the *p* side due to the interaction between the AGNRs and the OH groups of the SiO_2 surface.

Acknowledgement

I would like to express my grateful appreciation for my academic supervisor and main research advisor, Prof. Susumu Okada (Univ. of Tsukuba). He gave me a chance and a considerable support to take the Ph. D. I have spent a very exciting year thorough the fruitful discussions with him.

I also give special thanks to Prof. Yoshiyuki Miyamoto (AIST; Cooperative Graduate School), Prof. Kazuhiro Marumoto (Univ. of Tsukuba), and Prof. Takazumi Kawai (NEC; Cooperative Graduate School) for their kindly accept of inviting for my co-research advisors in their busy schedules. Their educational comments were very useful to write this thesis.

Last of all, I would like to thanks a lot to all past and current co-researchers; Prof. Yoshitada Morikawa in my master's studies at Osaka University, and Prof. Taisuke Ozaki (Univ. of Tokyo), Dr. Takahiro Yamasaki, and Dr. Chioko Kaneta after joining Fujitsu Labs. Ltd. I'm deeply grateful to Dr. Mari Ohfuchi. She game me much helpful advice for all of my research at Fujitsu Labs. Ltd.

Contents

Chapter 1. Introduction 1

1.1. Graphene 1

1.1.1. Fundamental characteristics 1

1.1.2. Physical properties 2

1.1.3. Fabrication methods 3

1.2. Graphene nanoribbons 7

1.3. Problems for graphene-based electronic devices 10

1.4. Objective and framework of this thesis 10

Chapter 2. Computational methods 12

2.1. Density functional theory 12

2.1.1. Born-Oppenheimer approximation 12

2.1.2. Hohenberg-Kohn theorems 13

2.1.3. Kohn-Sham equations 14

2.1.4. Local density approximation 16

2.1.5. Hellmann-Feynman force 17

2.2. Electronic structure calculations 19

2.2.1. Linear combination of atomic orbitals 19

2.2.2. Pseudopotential methods 20

2.3. Non-equilibrium Green's function method 22

2.3.1. Configurations and calculation procedures 22

2.3.2. Equilibrium state 25

2.3.3. Non-equilibrium state 29

Chapter 3. Graphene/metal electrode hybrid structures 31

3.1. Introduction 31

3.1.1. Contact resistance 31

3.1.2. Experimental studies 34
3.1.3. Theoretical studies 35
3.2. Computational details 38
3.3. Models 40
3.3.1. Equilibrium lattice parameters 40
3.3.2. Interfacial structures of graphene/metal surface 41
3.3.3. Electronic properties of graphene/metal hybrid structures 44
3.3.4. Discussion about the effect of different equilibrium interfacial spacing 47
3.3.5. Discussion about the effect of an artificial electric field 50
3.3.6. Structural model for transport calculations 52
3.4. Results and discussions 55
3.4.1. Current densities for the hybrid structure of graphene/Au electrodes 55
3.4.2. Origin of *N*-family dependence 57
3.4.3. Origin of *W* dependence 63
3.4.4. Hybrid structure of graphene/Ti electrodes 66
3.4.5. Discussions 71
3.5. Conclusions 72
Chapter 4. Graphene/insulator hybrid structures 73
4.1. Introduction 73
4.2. Computational details 75
4.3. Models 79
4.3.1. AGNRs 79
4.3.2. SiO_2/Si 81
4.3.3. AGNRs on SiO_2/Si 86
4.4. Results and discussions 88
4.4.1. Effect of different SiO_2 surface terminations to transport properties 88
4.4.2. Channel length dependence of transport properties 96

4.5. Conclusions 100

Chapter 5. Summary 101

Bibliography 103

Chapter 1. Introduction

In this chapter, we firstly introduce fundamental characteristics of graphene in Sec. 1.1 and graphene nanoribbons in Sec. 1.2. We then present the problems of the graphene for device applications in Sec. 1.3. We finally indicate the objective and the framework of this thesis in Sec. 1.4.

1.1. Graphene

For future nanoelectronics, explorations of new nano-materials are promised in order to realize high-speed transistors, batteries, sensors, and high-frequency devices. Recently various two-dimensional (2D) thin film materials have attracted attention as the new nano-materials because of their unique and intriguing physical properties. The most fascinating point of them is an atom thickness, which enables us to control material properties by stacking heterogenous materials and to get clean interface without dangling bonds. As examples of the 2D thin film materials, we show geometric structures of graphene [1], *h*-BN [2, 3], silicene [4], transition metal dichalcogenides [5, 6, 7] in Fig. 1.1. We focus on the graphene in this thesis, because it has a lot of curious physical properties ascribed to a sp^2 honeycomb network of carbon atoms. The graphene is also interesting in terms of the starting material of sp^2 carbon allotropes, such as a fullerene (0D) [8], a carbon nanotube (1D) [9], and a graphite (3D) [10].

1.1.1. Fundamental characteristics

Graphene is a two-dimensional sheet of sp^2-bonded carbon atoms with a honeycomb network as shown in Fig. 1.2(a). The lattice parameter *a* of the unit cell is 2.46 Å and the C-C bond length is 1.42 Å. The graphene is a monolayer of graphite and its existence has been theoretically predicted for a long time [11, 12]. Geim *et al.* first succeeded to exfoliate graphene from highly oriented pyrolytic graphite (HOPG) using a scotch tape and reported their high career mobility [1]. Following the exfoliation, the graphene has been studied intensely for various applications owing to their unique physical properties. It has been demonstrated that graphene is applicable for a field effect transistor (FET), a spintronics, a high-frequency photo diode, a photo

transistor, a two-dimensional plasmon device, a terahertz laser, a transparent electrode, an optical intensity modulation, an optical pulse compression, a solar cell, and a storage battery.

1.1.2. Physical properties

For each carbon atom in graphene, $2s$, $2p_x$, and $2p_y$ orbitals are hybridized to make sp^2 orbitals, which generate σ bands. The rest $2p_z$ orbital, which is distributed normal to the atomic network, forms π bands and its electrons are called the π electrons. The electronic states around the Fermi energy in graphene are determined by the π electrons. The primitive unit cell contains two inequivalent carbon atoms belonging to sublattices of A and B. The existence of two sublattices causes the unique electronic states around the Fermi energy. Figure 1.2(c) shows the energy band structure of graphene using a first-principles calculation. We can find that the linear conduction and valence bands consisting of the π-electrons are crossing at the *K* and *K'* points in the first Brillouin zone [Fig. 1.2(b)]. Electron hopping between the two sublattices leads to the bonding and the anti-bonding states at the Fermi energy and the *K* point. The *K* and *K'* points are called the Dirac points. As a result, quasiparticles in graphene exhibit the symmetric linear dispersion relation approximated by $E = \hbar k v_F$ as if they are massless relativistic particles with the Fermi velocity $v_F \approx c/300$, where c is the speed of light. This character gives the high carrier mobility of graphene up to 100,000 $cm^2V^{-1}s^{-1}$. Thus graphene is expected to be applicable for the fast and low power consumption devices.

In addition to the high carrier mobility, carriers in graphene can travel submicrometer distances (~300nm) without scattering, which is a favorable characteristic for quantum-effect and spintronics devices. Since graphene is highly sensitive to the environmental conditions because of its pure two-dimensionality, it is applicable to chemical and biological sensors. Graphene also shows uniform adsorption properties to lights of wide range of wavelength from a microwave to an ultraviolet due to the characteristic zero band gap property. The optical transmittance of a monolayer graphene is about 97.7 %. Graphene is a rare material with both the high transparency and the high electric conductivity. Thus, it could be applicable to the transparent electrodes. We can also observe peculiar quantum transport properties such as an absent of backscattering [13-15], an anomalous quantum Hall effect [16], and a Klein tunneling [17, 18], because

carriers in graphene behave like a 2D gas of massless Dirac fermions [19, 20]. Moreover, the high energy of the optical phonon originated from the strong and anisotropic sp^2 bonding and the low mass of carbon atoms give graphene the high thermal conductivity. Graphene is also mechanically strong and flexible.

1.1.3. Fabrication methods

The simplest method for obtaining graphene is the mechanical exfoliation from HOPG. In the method, graphite flakes are repeatedly peeled off with adhesive tape to cleave them in two and make them thinner and thinner. The flakes are deposited on an insulating substrate. The exfoliation method is suitable approach to know the physical properties of graphene itself, but alternative fabrication methods are essential for mass production of high-quality graphene for industrial applications.

One of the actively studied methods is a chemical vapor deposition (CVD) of graphene on the metal catalysts [21-25]. In this method, graphene is synthesized by introducing hydrocarbon gases such as methanol and ethanol on substrates with catalytic thin films or foils such as Cu, Ni, Co, and Fe. The carbon components are deposited on the metal surface through the chemical decomposition from the hydrocarbon gases by the metal catalysts. They are self-assembled to form the honeycomb network on the metal surface. Low-temperature growth due to using the metal-catalyzed reaction is consistent with the present semiconductor processes. The CVD is also powerful approach to obtain large-area graphene. However, the difficulty of controlling grain boundaries in the metal catalysts, which prevent epitaxial growth of graphene, is one of the disadvantages of this technique. It is also a crucial issue to transfer from the metal surface to the insulated substrate for the device application. The transfer process may affect the physical properties of graphene.

The thermal decomposition of SiC is another popular method of producing graphene [26-30]. When SiC substrates are annealed at high temperatures, only Si atoms desorb from the surface and the rest C atoms form graphene. The remaining SiC under the graphene can serve as a graphene substrate for electronics applications. The 6H-SiC and 4H-SiC, which have the six-fold rotational symmetry of lattice matching with the graphene, are usually used for this method. The fabricated graphene is epitaxial in essential owing to the

nature of the single crystal of SiC. The disadvantages of this method are the high cost of SiC and the high temperature process.

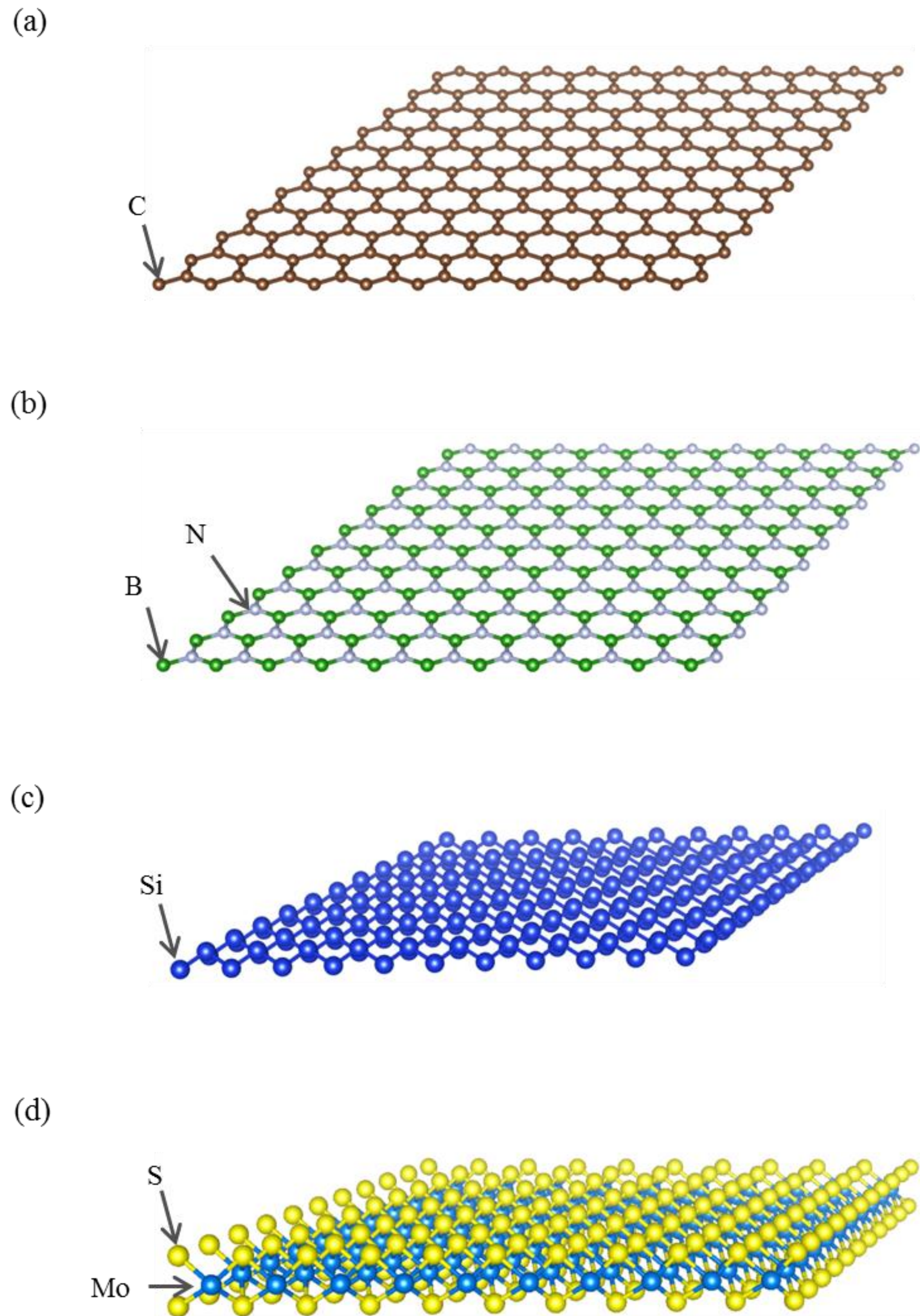

Fig. 1.1: Geometric structures of two-dimensional thin film materials. (a) Graphene, (b) h-BN, (c) silicene, and (d) monolayer of transition metal dichalcogenides.

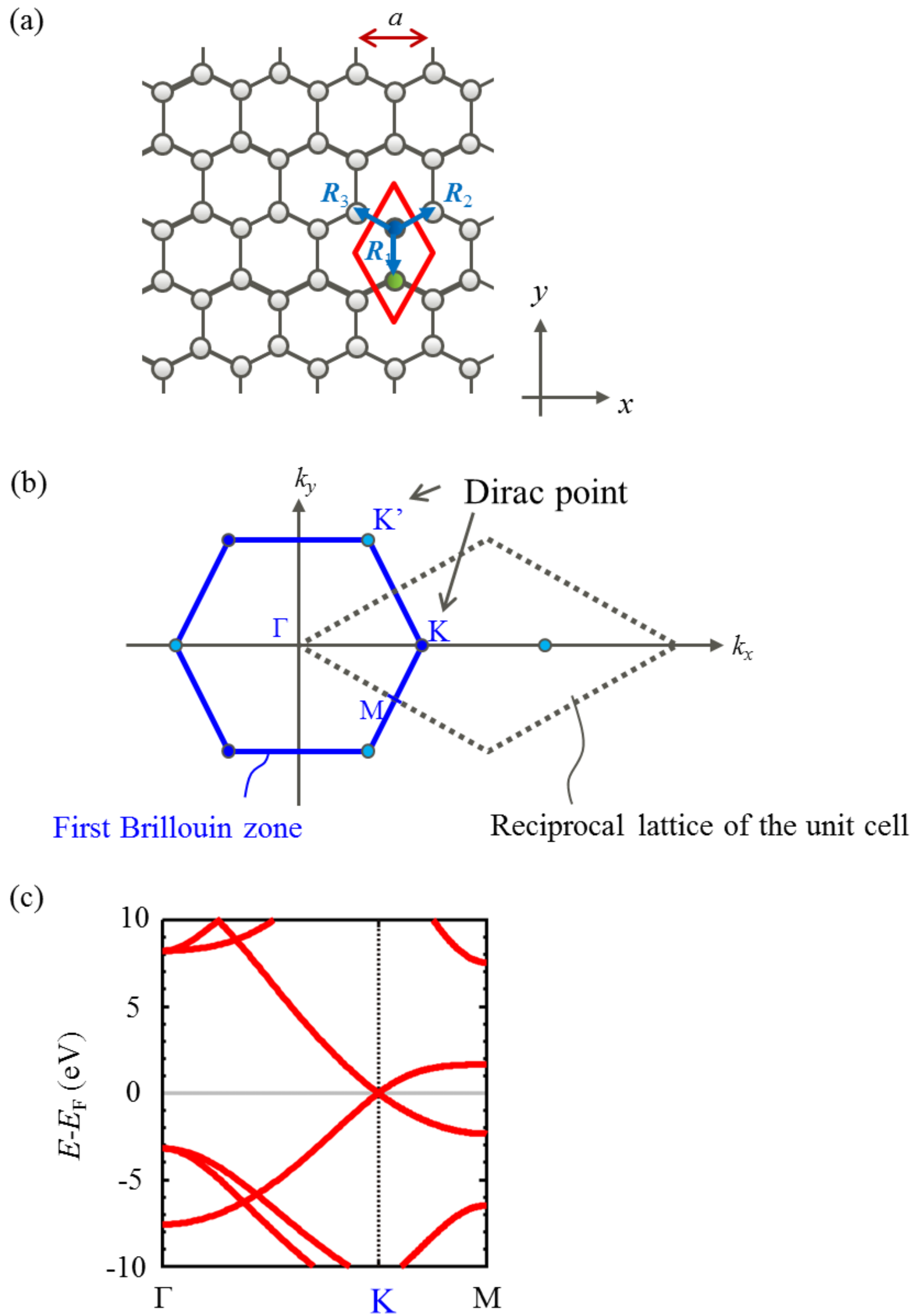

Fig. 1.2: (a) Crystallographic structure of graphene. The red rhombus is the primitive unit cell. The gray sphere represents a carbon atom. The green and blue spheres in the primitive unit cell indicate the sublattices of A and B, respectively. (b) Reciprocal lattice of the primitive unit cell and the first Brillouin zone. (c) Band structure of graphene using a first-principles calculation. The E_F is the Fermi energy.

1.2. Graphene nanoribbons

For semiconductor electronics applications of graphene, it is mandatory to control the energy band gap because graphene itself is a semiconductor with zero band gap. Various approaches have been proposed to open a band gap, such as a bilayer graphene under a vertical electric field [31, 32], an interaction with a substrate [33-35], a graphene nanomesh [36, 37], and graphene nanoribbons (GNRs) [38].

The GNRs are narrow stripes of graphene. Methods such as lithography [38], etching [39], and unzipping carbon nanotubes [40, 41], and bottom-up approach [42] are used for fabricating GNRs. The electronic structures of the GNRs depend on the edge structures [43-45]. The GNRs have two typical edges, which are called as an armchair [Fig. 1.3(a)] and a zigzag edges [Fig. 1.3(b)] due to their characteristic shapes. The GNRs with zigzag edges (ZGNRs) are metallic owing to peculiar edge localized states with nonbonding molecular orbitals at the Fermi level arising from the boundary condition imposed on graphene. In contrast, the GNRs with armchair edges (AGNRs) are semiconducting with the width of narrower than 10 nm owing to quantum confinement normal to the ribbon direction. The band gap energies of AGNRs depend on the width of ribbon which are classified into three families in terms of the number of C_2 dimer rows normal to the ribbon: $N = 3m$, $3m+1$, and $3m+2$, where m is an integer. For an integer m, AGNRs with the width of $N = 3m+1$ has the widest band gaps among three families, while those with the $N = 3m+2$ the narrowest band gap. For example, the band gap is 1.1 eV for $N = 6$ ($3m$ family of $m = 2$), 1.6 eV for $N = 7$ ($3m+1$ family of $m = 2$), and 0.2 eV for $N = 8$ ($3m+2$ family of $m = 2$), as shown in Fig. 1.4. Furthermore the band gaps are inversely proportional to N; for example, the band gap is 0.6 eV for $N = 19$. These values are obtained by first-principles calculations with a generalized gradient approximation (GGA), but a GW approximation, which includes the many-body effect, gives larger band gaps [46]. The strong dependences of electronic structures on geometries imply that atomically precise GNR fabrication will be necessary for electronic device applications.

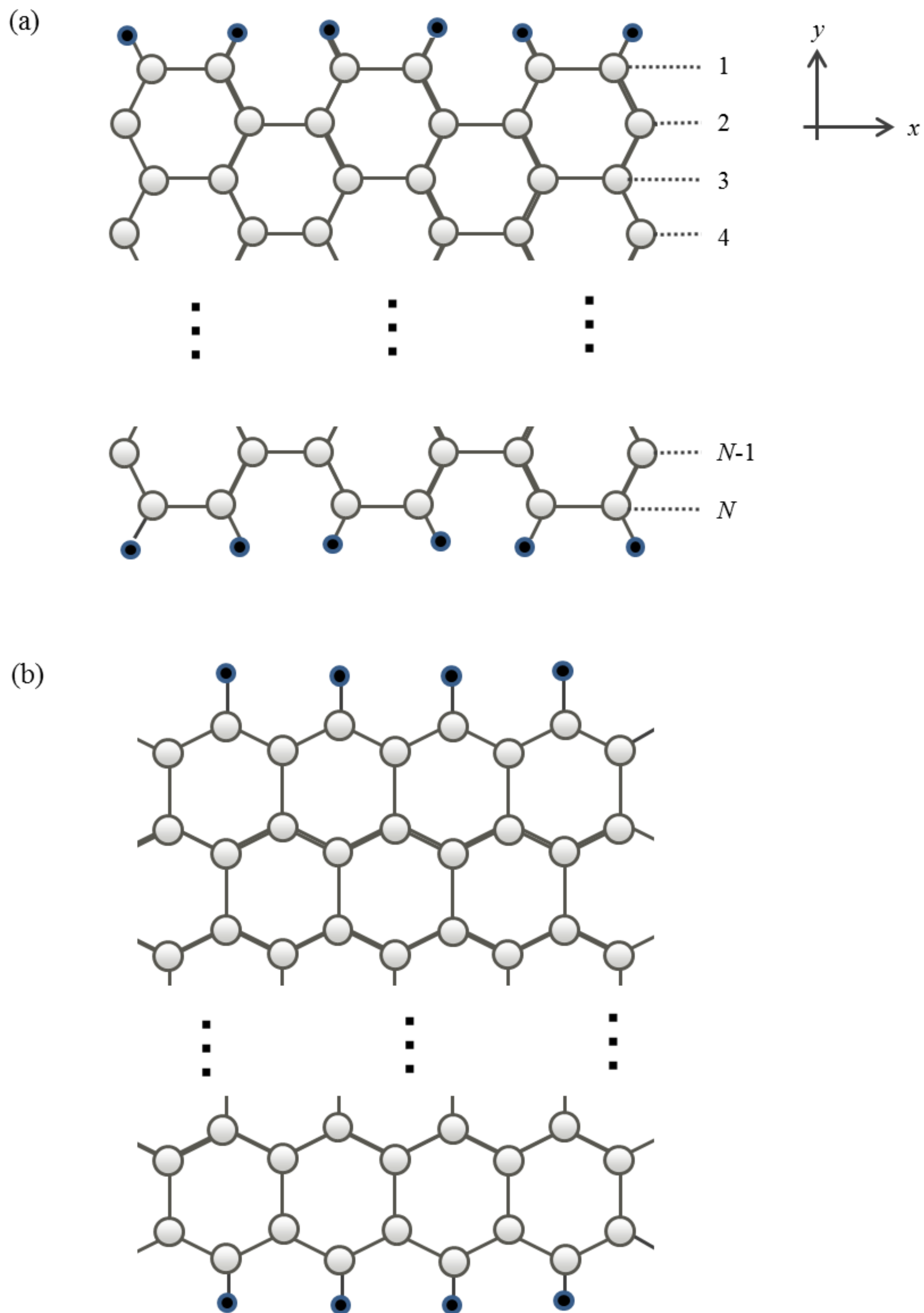

Fig. 1.3: Geometries of (a) an armchair graphene nanoribbons (AGNRs) and (b) a zigzag graphene nanoribbons (ZGNRs). The black sphere represents a hydrogen atom terminating the dangling bond of the edge carbon atoms. The ribbon width *N* is the number of carbon dimer rows.

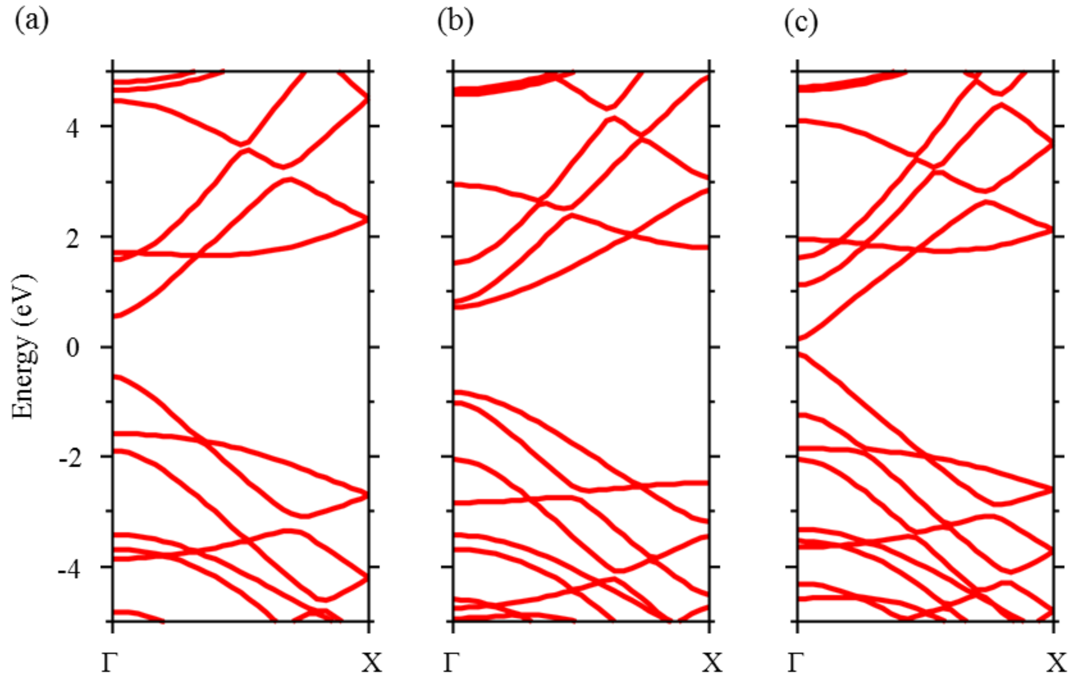

Fig. 1.4: Band structures of AGNRs with N = (a) 6, (b) 7, and (c) 8, which belong to the $3m$, $3m$+1, and $3m$+2 families, respectively, using the first-principles calculations. The Fermi energy is set to be 0 eV.

1.3. Problems for graphene-based electronic devices

One of serious problems for realizing graphene-based electronic devices [Fig. 1.5(a)] is the fragility of the electronic structure of graphene against foreign materials, such as metal electrodes and insulating substrates. The electronic properties of graphene are significantly modulated by physical contact with surrounding foreign materials, because the electron system of graphene is distributed normal to their atomic network that intrinsically forms interfaces with such foreign materials. At interfaces between graphene and metal surfaces, the high contact resistance is one of the critical issues for realizing graphene-based electronic devices: It has also been experimentally reported that the contact resistance depends on the metal species and the process conditions. In addition to the metals, insulating substrates also affect the electronic transport properties of graphene. The problems about two types of the hybrid systems will be discussed in this thesis.

1.4. Objective and framework of this thesis

In order to overcome the problems arising from interaction with the foreign materials, it is necessary to unravel the fundamental properties of the hybrid structures consisting of graphene and the foreign materials. In this thesis, we aim to provide the fundamental insight into the electronic and the transport properties of graphene in the hybrid structures using first-principles procedures.

The thesis is organized as following. In Chapter 2, we introduce the computational methods used in this study. All calculations are performed on the basis of the first-principles calculation methods. We employ the non-equilibrium Green's function methods for the electronic transport calculations. In Chapter 3, we investigate the fundamental properties of the graphene bridged between two metal electrodes as schematically illustrated in Fig. 1.5(b). We show the computational results of the model of up to 12 nm width graphene nanoribbons and discuss the transport properties focusing on the ribbon width. In Chapter 4, the fundamental properties of the graphene nanoribbons on SiO_2/Si as shown in Fig. 1.5(c) are examined. We discuss the variation of the transmission probability in terms of the channel length and the SiO_2/Si surface morphologies. In Chapter 5, we summarize the thesis.

(a)

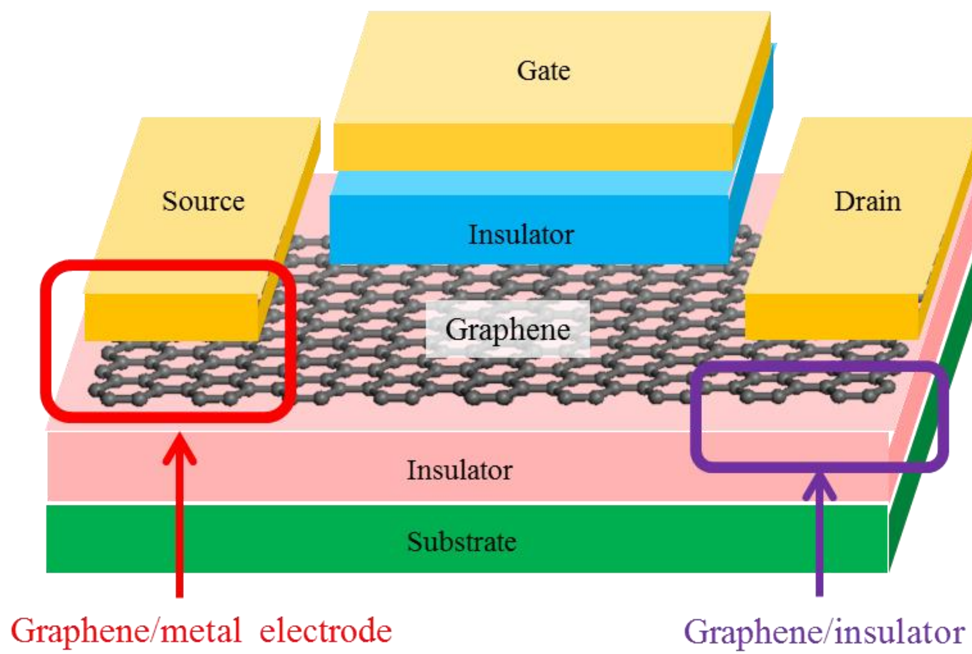

(b)

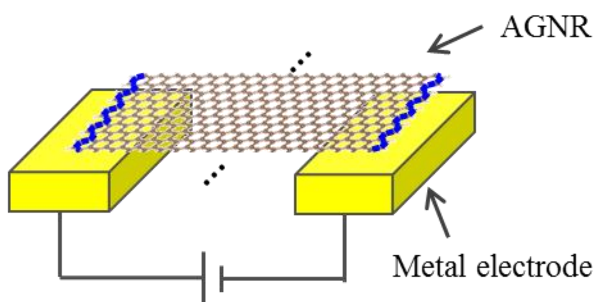

(c)

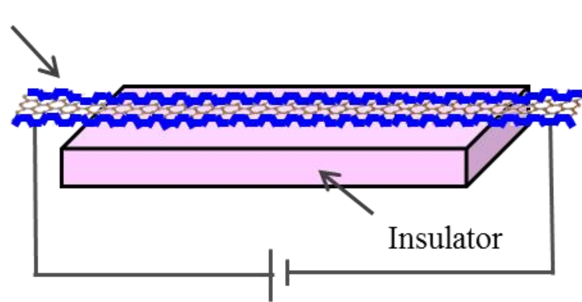

Fig. 1.5: (a) A schematic view of a graphene field effect transistor (FET). Structural models of (b) the graphene/metal electrodes and (c) the graphene/insulator employed in this thesis. The blue lines indicate the armchair edges of the AGNRs.

Chapter 2. Computational methods

In this chapter, we present computational methods used in this thesis. We describe the basis of the density functional theory (DFT) in Sec. 2.1. All calculations have been performed on the basis of the DFT. The DFT is one of the most computationally efficient first-principles methods to calculate atomic structures and electronic states of materials. We also explain the basis of the electronic structure calculations and the electronic transport calculations based on the non-equilibrium Green's function (NEGF) method using the DFT formalism in Sec. 2.2 and 2.3, respectively.

2.1. Density functional theory

The Schrödinger equation of a many-electron system is quite complicated due to the antisymmetric nature of the wave function under the exchange of two electrons and the electron-electron interaction. We need a one electron potential to obtain the electronic states of the materials. For atoms and molecules, the Hartree-Fock (HF) method is widely used. The method assumes that the exact many-body wave function of the system can be approximated by a single Slater determinant. However, the calculation of the exchange potential makes it difficult to apply the HF method to the solids. Another method to gain a one electron potential is the DFT, where the ground state of the many-electron system can be determined by using the spatially dependent electron density. The computational cost of the DFT is quite lower than that of the HF method. Thus the DFT has become a very popular and successful quantum mechanical approach to solve the many-body problems in condensed matter physics.

2.1.1. Born-Oppenheimer approximation

The many-body Hamiltonian of a system composed of M-nuclei and N-electrons is divided into five main terms:

$$H = T_n + T_e + V_{nn} + V_{ee} + V_{ne}. \tag{2.1}$$

The first and second terms in Eq. (2.1) are operators for the kinetic energies of the nuclei and the electrons,

respectively. The third term represents the Coulomb interaction energy between the nuclei. The fourth term represents the Coulomb interaction energy between the electrons. The fifth term represents the Coulomb interaction energy between the nuclei and the electrons. The eigenenergy ε and eigenfunction Φ of the total system described by the Hamiltonian in Eq. (2.1) are given by the solution of the following Schrödinger equation:

$$H\Phi(\mathbf{r}_1,\dots,\mathbf{r}_N;\mathbf{R}_1,\dots,\mathbf{R}_M) = \varepsilon\Phi(\mathbf{r}_1,\dots,\mathbf{r}_N;\mathbf{R}_1,\dots,\mathbf{R}_M), \tag{2.2}$$

where the many-body wave function $\Phi(\mathbf{r}_1,\dots,\mathbf{r}_N;\mathbf{R}_1,\dots,\mathbf{R}_M)$ depends on the nuclear coordinates $\mathbf{R}_n$ and the electron position $\mathbf{r}_i$. Since nuclei are much heavier than electrons, we can assume the position of the nuclei is static during the motion of the electrons. This approximation is known as the Born-Oppenheimer approximation [47].

The separated electronic Hamiltonian H_{el}, which describe the motion of *N*-electrons in the external potential $v(\mathbf{r}_i)$ derived from the fixed nuclei, is represented by

$$H_{el} = T_e + V_{ee} + V_{ne}\ , \tag{2.3}$$

$$T_e = -\sum_{i=1}^{N} \frac{\hbar^2}{2m} \nabla_i^2, \tag{2.4}$$

$$V_{ee} = \frac{1}{2} \sum_{i \neq j = 1}^{N} \frac{e^2}{4\pi\varepsilon|\mathbf{r}_i - \mathbf{r}_j|}, \tag{2.5}$$

$$V_{ne} = \sum_{i=1}^{N} v(\mathbf{r}_i). \tag{2.6}$$

Replacing the notation of H_{el} with H for simplicity, the Schrödinger equation of the *N*-electrons system is written by

$$H\psi(\mathbf{r}_1,\cdots,\mathbf{r}_\mathrm{N}) = E\psi(\mathbf{r}_1,\cdots,\mathbf{r}_N). \tag{2.7}$$

The DFT is explicated as the solving problem of the ground state of Eq. (2.7).

2.1.2. Hohenberg-Kohn theorems

The DFT is based on the two theorems proven by Hohenberg and Kohn in 1964 [48]. The first theorem

ensures that the charge density $n(\mathbf{r})$ is a unique functional of the external potential $v(\mathbf{r})$. The wave function ψ of the ground state is also uniquely determined by the $n(\mathbf{r})$. The second theorem is a variational principle on expectation value of the Hamiltonian, which is the global minimum value of the universal functional of $E[n(\mathbf{r})]$. It follows that the energy E of the ground state is written by

$$\begin{aligned} E[n(\mathbf{r})] &= \int \psi^* H \psi d\mathbf{r} \\ &= \int \psi^* (T_e + V_{ee}) \psi d\mathbf{r} + \int \psi^* V_{ne} \psi d\mathbf{r} \\ &= F[n(\mathbf{r})] + \int v(\mathbf{r}) n(\mathbf{r}) d\mathbf{r} \geq E[n_0(\mathbf{r})], \end{aligned} \tag{2.8}$$

where $F[n(\mathbf{r})]$ is represented as an universal functional of $n(\mathbf{r})$ independent of $v(\mathbf{r})$ and n_0 is the charge density of the ground state. Thus the DFT is strict theory in terms of the ground state. If we know the functional form of $F[n(\mathbf{r})]$, the energy of the ground state can be obtained by the charge density $n_0(\mathbf{r})$.

2.1.3. Kohn-Sham equations

To utilize the Hohenberg-Kohn (HK) theorems for practical calculations on interacting electrons, Kohn and Sham mapped the problem of the system of interacting electrons onto a fictitious system of non-interacting electrons [49]:

$$F[n(\mathbf{r})] = T_s[n(\mathbf{r})] + \frac{e^2}{2} \int \frac{n(\mathbf{r}) n(\mathbf{r}')}{|\mathbf{r} - \mathbf{r}'|} d\mathbf{r} d\mathbf{r}' + E_{xc}[n(\mathbf{r})], \tag{2.9}$$

where the first term T_s is the kinetic energy of the system of the non-interacting electrons with the charge density $n(\mathbf{r})$, the second term is the energy of the electrostatic interaction (Hartree term), and the third term is defined as the exchange-correlation energy in which all many-body effects on interacting electrons are taken into account.

The Kohn-Sham (KS) total-energy functional of a system of interaction N electrons is thus expressed as,

$$E[n(\mathbf{r})] = T_s[n(\mathbf{r})] + \frac{e^2}{2} \int \frac{n(\mathbf{r}) n(\mathbf{r}')}{|\mathbf{r} - \mathbf{r}'|} d\mathbf{r} d\mathbf{r}' + E_{xc}[n(\mathbf{r})] + \int v(\mathbf{r}) n(\mathbf{r}) d\mathbf{r}, \tag{2.10}$$

Based on the HK theorem, the ground state is determined by applying the variation principle with respect to $n(\mathbf{r})$.

$$\delta\left[E[n(\mathbf{r})]-\epsilon\left(\int d\mathbf{r}\, n(\mathbf{r})-N\right)\right]=0, \tag{2.11}$$

$$\frac{\delta E[n(\mathbf{r})]}{\delta n(\mathbf{r})}=\epsilon, \tag{2.12}$$

where ϵ is a Lagrange multiplier to specify the number of electrons. If we rewrite Eq. (2.12) using Eq. (2.10),

$$\frac{\delta T_s[n(\mathbf{r})]}{\delta n(\mathbf{r})}+v_{eff}(\mathbf{r})=\epsilon, \tag{2.13}$$

where $v_{eff}(\mathbf{r})$ is defined as:

$$v_{eff}(\mathbf{r})=v(\mathbf{r})+\int\frac{n(\mathbf{r}')}{|\mathbf{r}-\mathbf{r}'|}d\mathbf{r}'+v_{xc}(\mathbf{r}). \tag{2.14}$$

The $v_{xc}(\mathbf{r})$ is the exchange-correlation potential given by the functional deviation of the exchange-correlation energy $E_{xc}[n(\mathbf{r})]$ with respect to the charge density $n(\mathbf{r})$:

$$v_{xc}(\mathbf{r})=\frac{\delta E_{xc}[n(\mathbf{r})]}{\delta n(\mathbf{r})}. \tag{2.15}$$

The Eq. (2.13) is an equation of non-interacting electrons moving in the effective potential $v_{eff}(\mathbf{r})$, because $T_s[n(\mathbf{r})]$ corresponds to the kinetic energy of non-interacting electrons of the density $n(\mathbf{r})$. To express the electron density $n(\mathbf{r})$, Kohn and Sham adopted single-electron orbitals $\psi(\mathbf{r})$ as follows:

$$n(\mathbf{r})=\sum_{i=1}^{N}|\psi_i(\mathbf{r})|^2. \tag{2.16}$$

Using the $\psi(\mathbf{r})$, the $T_s[n(\mathbf{r})]$ can be replaced by following equation:

$$T_s[n(\mathbf{r})]=\sum_{i=1}^{N}\left\langle\psi_i(\mathbf{r})\middle|-\frac{\hbar^2}{2m}\nabla^2\middle|\psi_i(\mathbf{r})\right\rangle. \tag{2.17}$$

By substituting Eq. (2.17) in to Eq. (2.13),

$$\left[-\frac{\hbar^2}{2m}\nabla^2+v_{eff}(\mathbf{r})\right]\psi_i=\epsilon_i\psi_i, \tag{2.18}$$

where ϵ_i is the eigenenergy of the electron, The Eq. (2.18) with Eqs. (2.14)-(2.16) is the KS equations. They should be self-consistently resolved because the wave function of the solution depends on the charge density defined by the summation of the squared wave function for occupied states. The problem of solving the ground state of the *N*-electrons system is interpreted as the simple one-particle problem under the effective

potential $v_{eff}(\mathbf{r})$. The effective potential $v_{eff}(\mathbf{r})$ is composed of the external potential $v(\mathbf{r})$ derived from the atomic nuclei, the electrostatic interaction potential, and the exchange-correlation potential $v_{xc}(\mathbf{r})$, as shown in Eq. (2.14). The electron correlation effect is included in the KS equation.

2.1.4. Local density approximation

To solve the KS equation practically, we require the explicit expression for $E_{xc}[n(\mathbf{r})]$ and $v_{xc}(\mathbf{r})$. In the local density approximation (LDA), the exchange-correlation energy $E_{xc}[n(\mathbf{r})]$ depends only on the local value of the charge density $n(\mathbf{r})$ under the assumption of the homogeneous electron gas. Then the $E_{xc}[n(\mathbf{r})]$ is written by

$$E_{xc}[n(\mathbf{r})] \approx \int \epsilon_{xc}[n(\mathbf{r})]\, n(\mathbf{r}) d\mathbf{r}, \tag{2.19}$$

where $\epsilon_{xc}[n(\mathbf{r})]$ is the exchange-correlation energy of one particle in the uniform electron gas with the charge density of $n(\mathbf{r})$. Thus the exchange-correlation potential v_{xc} is given by

$$v_{xc}(\mathbf{r}) = \frac{\delta E_{xc}}{\delta n(\mathbf{r})} = \epsilon_{xc}[n(\mathbf{r})] + n(\mathbf{r})\frac{\partial \epsilon_{xc}[n]}{\partial n}. \tag{2.20}$$

The exchange-correlation energy can be divided into the exchange and the correlation terms as follows:

$$\epsilon_{xc} = \epsilon_x + \epsilon_c \tag{2.21}$$

The analytical representation of the exchange energy ϵ_x is derived from the exchange potential term in the HF approximation as follows:

$$\epsilon_x = -\frac{3e^2}{2}\left(\frac{3}{8\pi}n(\mathbf{r})\right)^{\frac{1}{3}}. \tag{2.22}$$

The exchange potential corresponding to this ϵ_x is given by

$$\begin{aligned} v_x(\mathbf{r}) &= \left[\frac{d(n\epsilon_x[n])}{dn}\right]_{n=n(\mathbf{r})} \\ &= -2\mathrm{e}^2\left[\frac{3}{8\pi}n(\mathbf{r})\right]^{\frac{1}{3}}. \end{aligned} \tag{2.23}$$

The exchange potential derived from the LDA includes the self-interaction between the identical orbitals, because it uses the term of the exchange interaction potential. The electrostatic and the exchange interaction in the identical orbitals should annihilate each other to be zero with respect to the orthonormalized orbitals.

The fact that the condition is not fulfilled in the LDA is considered to be one of the origins of the underestimation in the energy band gap.

The correlation energy density ϵ_c cannot be represented by the analytical form, in contrast to the exchange energy density ϵ_x. It is described by the parameterization for the correlation energy of the uniform electron gas as a function of the charge density. For examples, Ceperly and Alder numerically parameterized the correlation energy to be used in DFT calculations from quantum Monte Carlo calculations [50].

For the system with inhomogeneous electron densities, the generalized gradient approximation (GGA) is often employed instead of the LDA [51]. The GGA is the method to improve the LDA by introducing the gradient of the density. The exchange-correlation energy in the GGA depends on not only the electron density but also derivatives of the density, and it is given by

$$E_{xc}^{GGA}[n(\mathbf{r})] \approx \int f[n(\mathbf{r}), \nabla n(\mathbf{r})]\, d\mathbf{r}, \tag{2.24}$$

where f is a function of the electron density and its derivative. The binding energies become better than the LDA owing to the including the gradient of the electron density.

2.1.5. Hellmann-Feynman force

When each ψ_i is an eigenstate of the Hamiltonian in the KS equation, the partial derivative of the KS energy functional with respect to the position of an ion gives the real physical force on the ion. The force $\boldsymbol{F}_I$ on an ion I is minus the derivative of the total energy $E[n(\mathbf{r})]$ of a system with respect to the position of the ion $\mathbf{R}_I$ as follows:

$$\begin{aligned} \boldsymbol{F}_I &= -\frac{dE[\{\psi_i\}, \{\mathbf{R}_I\}]}{d\mathbf{R}_I} \\ &= -\frac{\partial E}{\partial \mathbf{R}_I} - \sum_i \int d^3r \left\{ \frac{\delta E}{\delta \psi_i(\mathbf{r})} \frac{d\psi_i(\mathbf{r})}{d\mathbf{R}_I} + \frac{\delta E}{\delta \psi_i^*(\mathbf{r})} \frac{d\psi_i^*(\mathbf{r})}{d\mathbf{R}_I} \right\}. \end{aligned} \tag{2.25}$$

where the first term on the right side is the force derived from the position dependency of the KS Hamiltonian, which is referred to as the Hellmann-Feynman force. If the H is the KS Hamiltonian,

$$\frac{\delta E}{\delta \psi_i^*(\mathbf{r})} = H\psi_i(\mathbf{r}). \tag{2.26}$$

Hence Eq. (2.25) is rewritten by

$$\boldsymbol{F}_I = -\frac{\partial E}{\partial \mathbf{R}_I} - \sum_i \left\{ \left\langle \psi_i \middle| H \middle| \frac{d\psi_i}{d\mathbf{R}_I} \right\rangle + \left\langle \frac{d\psi_i}{d\mathbf{R}_I} \middle| H \middle| \psi_i \right\rangle \right\}. \tag{2.27}$$

If each ψ_i is an eigenenergy of the Hamiltonian H,

$$\left\langle \psi_i \middle| H \middle| \frac{d\psi_i}{d\mathbf{R}_I} \right\rangle + \left\langle \frac{d\psi_i}{d\mathbf{R}_I} \middle| H \middle| \psi_i \right\rangle = \varepsilon_i \frac{d}{d\mathbf{R}_I} \langle \psi_i | \psi_i \rangle = 0, \tag{2.28}$$

resulting in only the Hellmann-Feynman force:

$$\boldsymbol{F}_I = -\frac{\partial E}{\partial \mathbf{R}_I}. \tag{2.29}$$

However, if we introduce some basis sets to represent the eigenstates, i.e.,

$$\psi_i(\mathbf{r}) = \sum_\mu c_{i\mu} \chi_\mu(\mathbf{r}), \tag{2.30}$$

where χ_μ denote the basis set, the eigen energy ε_i is determined by the eigenvalue equation:

$$\sum_{\mu'} H_{\mu\mu'} c_{i\mu'} = \varepsilon_i \sum_\mu c_{i\mu'} S_{\mu\mu'}, \tag{2.31}$$

where the Hamiltonian $H_{\mu\mu}^{'}$ and the overlap matrix $S_{\mu\mu'}$ are defined as

$$H_{\mu\mu'} = \left\langle \chi_\mu \middle| H \middle| \chi_{\mu'} \right\rangle, \tag{2.32}$$

$$S_{\mu\mu'} = \left\langle \chi_\mu \middle| \chi_{\mu'} \right\rangle. \tag{2.33}$$

Since the ψ_i is normalized,

$$\langle \psi_i | \psi_i \rangle = \sum_{\mu\mu'} c_{i\mu'} c_{i\mu}^* S_{\mu\mu'} = 1. \tag{2.34}$$

Using Eqs. (2.30)-(2.34), Eq. (2.27) is expressed as

$$\boldsymbol{F}_I = -\frac{\partial E}{\partial \mathbf{R}_I} - \sum_i \left\{ \sum_{\mu'\mu} c_{i\mu'}^* c_{i\mu} \left(\left\langle \frac{d\chi_{\mu'}}{d\mathbf{R}_I} \middle| H - \varepsilon_i \middle| \chi_\mu \right\rangle + \left\langle \chi_{\mu'} \middle| H - \varepsilon_i \middle| \frac{d\chi_\mu}{d\mathbf{R}_I} \right\rangle \right) \right\}. \tag{2.35}$$

The second term of this equation contains the derivative of the basis set with respect to the position of the ion. The contribution of this term to the force on the ion is called as the Pulay force [52].

2.2. Electronic structure calculations

As shown in the previous section, the DFT provides theoretical frameworks for obtaining the ground state total energy, the ground state electron density, and the optimized atomic structure. The electronic structure method based on a linear combination of numerical atomic local basis orbitals [53-58] and pseudo potentials [59, 60] is a possible way of extending the applicability of the DFT to large-scale systems, since the generalized eigenvalue problem with the resultant sparse matrices can be solved with the use of the low computational cost.

2.2.1. Linear combination of atomic orbitals

In this thesis, the wave functions ψ_μ in the KS equation are expanded in terms of linear combination of pseudo-atomic orbitals (LCPAO) $\phi_{i\alpha}$ centered on the site τ_i by

$$\psi_{\sigma\mu}^{(\boldsymbol{k})}(\mathbf{r}) = \frac{1}{\sqrt{N}}\sum_{n}^{N} e^{i\mathbf{R}_n\cdot\boldsymbol{k}} \sum_{i\alpha} c_{\sigma\mu,i\alpha}^{(\boldsymbol{k})}\,\phi_{i\alpha}(\mathbf{r}-\tau_i-\mathbf{R}_n), \tag{2.36}$$

where c is an expansion coefficient, $\mathbf{R}_n$ is a lattice vector, $\boldsymbol{k}$ is a Bloch wave vector, i is a site index, σ is a spin index (up or down), μ is an eigenstate index, and α is an orbital index. Considering the variation in the total energy of the system expressed by the KS wave function $\psi_{\sigma\mu}^{(\boldsymbol{k})}$ with respect to the coefficients c, we obtain the following KS matrix equation:

$$H_\sigma^{(\boldsymbol{k})} c_{\sigma\mu}^{(\boldsymbol{k})} = \varepsilon_{\sigma\mu}^{(\boldsymbol{k})} S^{(\boldsymbol{k})} c_{\sigma\mu}^{(\boldsymbol{k})}, \tag{2.37}$$

where $c_{\sigma\mu}^{(\boldsymbol{k})}$ is a column vector consisting of the coefficients $\{c_{\sigma\mu,i\alpha}^{(\boldsymbol{k})}\}$. The Hamiltonian $H_\sigma^{(\boldsymbol{k})}$ and overlap matrices $S^{(\boldsymbol{k})}$ are given by

$$H_{\sigma,i\alpha j\beta}^{(\boldsymbol{k})} = \sum_n e^{i\boldsymbol{k}\cdot\mathbf{R}_n} h_{\sigma,i\alpha j\beta,\mathbf{R}_n}, \tag{2.38}$$

$$S_{i\alpha j\beta}^{(\boldsymbol{k})} = \sum_n e^{i\boldsymbol{k}\cdot\mathbf{R}_n} s_{i\alpha j\beta,\mathbf{R}_n}, \tag{2.39}$$

where $h_{\sigma,i\alpha j\beta,\mathbf{R}_n}$ and $s_{i\alpha j\beta,\mathbf{R}_n}$ are the Hamiltonian and overlap matrix elements between two basis functions $\phi_{i\alpha}(\mathbf{r}-\tau_i)$ and $\phi_{i\beta}(\mathbf{r}-\tau_i-\mathbf{R}_n)$, respectively. The overlap matrix arises from the nonorthogonality of the pseudo atomic orbital (PAO) basis functions.

2.2.2. Pseudopotential methods

Most physical and chemical properties of atoms, molecules, and solid strongly depend on valence electrons. The core electrons are strongly bound to the nuclei and do not play a significant role in the chemical properties of atoms. In the pseudopotential method, core electrons around the atomic nucleus are replaced by potential functions with respect to valence electrons. By using pseudopotentials, we can calculate only the valence electron states without the calculation of the core electrons, whose computational cost is a vast amount. The pseudo potentials are generated for atoms of each element and they are used in combination.

In this thesis, we use the norm-conserving pseudopotentials [61]. The pseudopotentials, which have a same norm with the true valence wave functions, are constructed by forcing the pseudo wave functions to coincide with the true valence wave functions outside a given radius, designated the core radius. The charge densities obtained outside the core region must be also identical to the true charge density. Thus, the integral of the squared amplitudes of the real and pseudo wave functions over the core region must be identical. This condition is referred as “norm-conservation”.

The atomic properties of the element must be preserved, including phase shifts on scattering across the core. These phase shifts will be different for each angular momentum state. In general, the pseudopotential must be non-local with projectors for each angular momentum components l, m, as represented using the form:

$$V = V_{loc} + \sum_{l,m} (V_l - V_{loc}) P_{l,m}, \tag{2.40}$$

where $P_{l,m}$ are the projectors of the electronic wave functions on to the eigenfunctions of each angular momentum state, V_{loc} is the local part chosen arbitrarily.

The pseudopotentials are constructed using an ab-initio procedure. The true wave functions are calculated for a free atom by comparing with a given reference electron configuration, using an all-electron DFT approach. The resulting valence wave functions are then modified to remove the rapid oscillations in the core region under the norm-conservation constraint. The Schrödinger equation is then inverted to find the

pseudopotential which will reproduce the pseudo wave functions. This procedure produces a pseudopotential which may be transferred between widely varying systems.

2.3. Non-equilibrium Green's function method

In this thesis, we use a non-equilibrium Green's function (NEGF) method for the first-principles electronic transport calculations. We summarized advantages of the NEGF method: (i) the source and drain contacts are treated based on the same theoretical framework as for the scattering region in terms of the coherent transport; (ii) the electronic structure of the scattering region under a finite source-drain bias voltage is self-consistently determined by combining with first-principles electronic structure calculation methods such as the HF and the DFT method; (iii) many-body effects in the transport properties, e.g., electron-phonon and electron-electron interactions, are included thorough self-energies; (iv) its applicability to large-scale systems can be anticipated basis functions in real space, resulting in computation for sparse matrices. Due to these advantages, the NEGF method has been successfully applied to calculations for the electronic transport properties of various systems.

We present configurations of the system for the NEGF method and calculation procedures in Sec. 2.3.1. We explain the NEGF method on the coherent transport according to the Ref. [62] for equilibrium and non-equilibrium states in Sec. 2.2.2 and 2.2.3, respectively.

2.3.1. Configurations and calculation procedures

We firstly set up a configuration of the system for the NEGF method in Fig. 2.1. The electronic transport is assumed to occur along the a axis under a two-dimensional periodic boundary condition imposed on the bc plane. The one-dimensional infinite cell consists of the central region denoted by C_0 and the cells denoted by L_i and R_i, where $i = 0, 1, 2, \ldots, \infty$. All the cells L_i (R_i) are arranged semi-infinitely and contain the same number of atoms with the same structural configuration. We consider a central region C consisting of C_0, L_0, and R_0 to allow the relaxation of electronic structure around the interfaces between the leads (L_0 and R_0) and the scattering region (C_0). Lead regions of L and R consist of L_i ($i = 1, 2, \ldots, \infty$) and R_i ($i = 1, 2, \ldots, \infty$), respectively. Two conditions are also imposed: (i) The localized basis orbitals in the C_0 overlap only with those in the L_0 and R_0. (ii) The localized basis orbitals in the L_i (R_i) overlap only with basis orbitals in the nearest neighboring cells $L_{i\text{-}1}$ ($R_{i\text{-}1}$) and L_{i+1} (R_{i+1}). Overlaps between the next nearest neighboring cells are

not allowed. The size of the unit cells for L_i and R_i is adjusted with consideration for the specific cutoff radii of the localized basis orbitals to satisfy these two conditions.

We preliminarily evaluate electronic states of the left and right leads using conventional band calculations under the three-dimensional periodic boundary condition. The fine k-sampling along the a axis is required compared with the conventional band calculation to ensure consistency with the semi-infinity along the a axis in the calculation of the surface Green's function. Then we perform self-consistent NEGF calculations, where the effect of the leads is taken into account as the self-energies. The unit cell of the bc plane in the leads is also assumed in the C region. Finally, the transmission and the current are evaluated by the Landauer formula [63, 64].

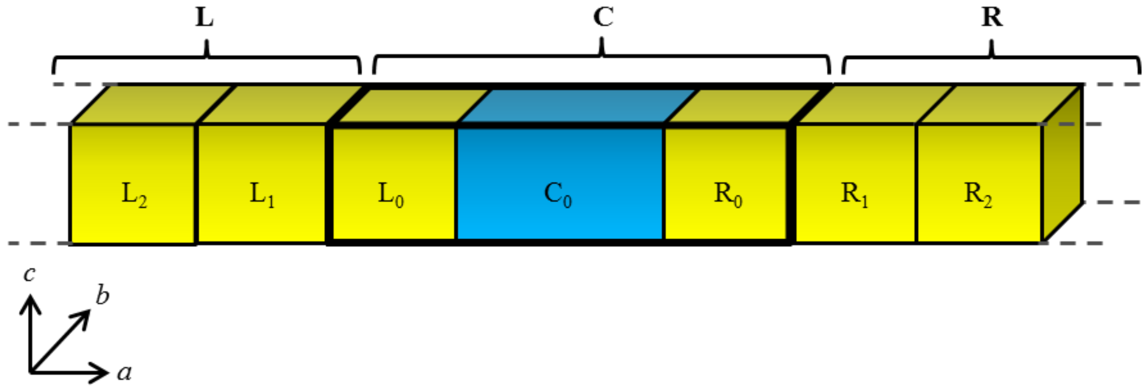

Fig. 2.1: The geometric structure of the one-dimensional system for the NEGF method. It is compacted from three-dimensional system by considering the periodicity along the *b* and *c* axis. The infinite left and right leads of *L* and *R* are along the *a* axis. The central region *C* consists of C_0, L_0, and $R_{0.}$ The lead regions of *L* and *R* consist of L_i (i = 1, 2, …, ∞) and R_i (i = 1, 2, …, ∞), respectively.

2.3.2. Equilibrium state

In the equilibrium state with a homogeneous chemical potential in the system, the electronic structure of the system may be determined by the DFT as described in Sec. 2.1 and 2.2. The KS wave function in the system is expressed by Eq. (2.36), which is reprinted here,

$$\psi_{\sigma\mu}^{(\boldsymbol{k})}(\mathbf{r}) = \frac{1}{\sqrt{N}}\sum_{n}^{N} e^{i\mathbf{R}_n\cdot\boldsymbol{k}} \sum_{i\alpha} c_{\sigma\mu,i\alpha}^{(\boldsymbol{k})}\, \phi_{i\alpha}(\mathbf{r}-\tau_i-\mathbf{R}_n). \tag{2.36}$$

Due to the periodicity along the b and c directions, the lattice vector $\mathbf{R}_n$ and the Bloch wave vector $\boldsymbol{k}$ are given by $\mathbf{R}_n = l_b\boldsymbol{b} + l_c\boldsymbol{c}$, where $\boldsymbol{b}$ and $\boldsymbol{c}$ are the lattice vectors, and $\boldsymbol{k} = k_b\tilde{\boldsymbol{b}} + k_c\tilde{\boldsymbol{c}}$, where $\tilde{\boldsymbol{b}}$ and $\tilde{\boldsymbol{c}}$ are the reciprocal lattice vectors, respectively. The summation over i and α is considered for all the basis orbitals in the one-dimensional infinite cell, which indicates no periodicity along the a axis. Under the two conditions in Sec. 2.3.1, the Hamiltonian matrix and the overlap matrix given by Eq. (2.38) and (2.39), respectively, are written by a block tridiagonal form as follows:

$$H_{\sigma}^{(\boldsymbol{k})} = \begin{pmatrix} \ddots & \ddots & & & 0 \\ \ddots & H_{\sigma,L_1}^{(\boldsymbol{k})} & H_{\sigma,L_1C}^{(\boldsymbol{k})} & & \\ & H_{\sigma,CL_1}^{(\boldsymbol{k})} & H_{\sigma,C}^{(\boldsymbol{k})} & H_{\sigma,CR_1}^{(\boldsymbol{k})} & \\ & & H_{\sigma,R_1C}^{(\boldsymbol{k})} & H_{\sigma,R_1}^{(\boldsymbol{k})} & \ddots \\ 0 & & & \ddots & \ddots \end{pmatrix}, \tag{2.41}$$

$$S^{(\boldsymbol{k})} = \begin{pmatrix} \ddots & \ddots & & & 0 \\ \ddots & S_{L_1}^{(\boldsymbol{k})} & S_{L_1C}^{(\boldsymbol{k})} & & \\ & S_{CL_1}^{(\boldsymbol{k})} & S_{C}^{(\boldsymbol{k})} & S_{CR_1}^{(\boldsymbol{k})} & \\ & & S_{R_1C}^{(\boldsymbol{k})} & S_{R_1}^{(\boldsymbol{k})} & \ddots \\ 0 & & & \ddots & \ddots \end{pmatrix}, \tag{2.42}$$

where $H_{\sigma,C}^{(\boldsymbol{k})}$ ($S_{C}^{(\boldsymbol{k})}$), $H_{\sigma,L_1}^{(\boldsymbol{k})}$ ($S_{L_1}^{(\boldsymbol{k})}$), and $H_{\sigma,R_1}^{(\boldsymbol{k})}$ ($S_{R_1}^{(\boldsymbol{k})}$) are Hamiltonian (overlap) matrices of the channel (C), left lead (L_1) and right lead (R_1). The index of σ represents the spin degree of freedom. Hereafter, the indices σ and $\boldsymbol{k}$ are omitted for simplicity. The Green's function is defined as $G(Z)(ZS-H)=I$, where Z is the complex energy. By using the block tridiagonal form of the Hamiltonian and the overlap matrices, the Green function of the C region G_C can be written by (p. 227, Ref. [65])

$$G_C(Z) = [ZS_C - H_C - \Sigma_L(Z) - \Sigma_R(Z)]^{-1}, \tag{2.43}$$

with self-energies Σ_L and Σ_R defined by

$$\Sigma_L(Z) = \left(ZS_{CL_1} - H_{CL_1}\right)G_L(Z)\left(ZS_{L_1C} - H_{L_1C}\right), \tag{2.44}$$

$$\Sigma_R(Z) = \left(ZS_{CR_1} - H_{CR_1}\right)G_R(Z)\left(ZS_{R_1C} - H_{R_1C}\right), \tag{2.45}$$

where $G_L(Z)$ and $G_R(Z)$ is surface Green function of the *L* and *R* region, respectively. The effects of the semi-infinite *L* and *R* are included thorough the corresponding self-energies $\Sigma_L(Z)$ and $\Sigma_R(Z)$, whose real and imaginary parts give the shift and the broadening of the eigenenergy in the *C* region, respectively. The surface Green function is defined by $G_L(Z) \equiv (ZS_L - H_L)^{-1}$ and $G_R(Z) \equiv (ZS_R - H_R)^{-1}$. The constraint that localized basis orbitals in the L_0 (R_0) within the *C* region overlap only with basis orbitals in the nearest neighboring cells L_1 (R_1) enables us to obtain the simple expressions of the self-energies in Eqs. (2.44) and (2.45). In order to practically calculate the G_C given by Eq. (2.43), we introduce an approximation that the L_i (i = 1, 2, …, ∞) regions are all equivalent to each other with respect to the spatial charge distribution, the KS Hamiltonian, and the relevant density matrix. They are calculated in advance by adopting the system of which unit cell is L_1 and by using the conventional band structure calculation. The same approximation also applies for the R_i (i = 1, 2, …, ∞) regions. The assumption is asymptotically correct as the unit vector becomes larger, if the size of the unit vector along the *a* axis for the L_0 and R_0 regions within the *C* region is large enough. The approximation enables us to evaluate the surface Green function by the iterative method [66].

When the Hamiltonian and overlap matrices associated with Eq. (2.43) are $\boldsymbol{k}$ dependent, the density matrix $\rho^{(\mathrm{eq})}_{\mathbf{R}_n}$, where one of the associated basis orbitals is in the central cell and the other is in the cell denoted by $\mathbf{R}_n$, is given by making use of both the retarded and advanced Green functions $G_C^{(\boldsymbol{k})}(E + i0^+)$ and $G_C^{(\boldsymbol{k})}(E - i0^+)$ as

$$\rho^{(\mathrm{eq})}_{\mathbf{R}_n} = \frac{1}{V_C}\int_{BZ} dk^3 \left(\rho_+^{(\boldsymbol{k})} - \rho_-^{(\boldsymbol{k})}\right) e^{-i\boldsymbol{k}\cdot\mathbf{R}_n}, \tag{2.46}$$

with

$$\rho_\pm^{(\boldsymbol{k})} = \frac{i}{2\pi}\int_{-\infty}^{\infty} dE\, G_C^{(\boldsymbol{k})}(E \pm i0^+) f(E - \mu), \tag{2.47}$$

where V_C is the volume of the unit cell, $\int_{BZ}$ represents the integration over the first Brillouin zone, 0^+ is a positive infinitesimal, and μ is a chemical potential. In case of the ***k***-independent problem, Eq. (2.46) can be simplified into

$$\rho^{(\mathrm{eq})} = \mathrm{Im}\left[-\frac{1}{\pi}\int_{-\infty}^{\infty} dE G_C(E + i0^+) f(E-\mu)\right]. \tag{2.48}$$

The Fermi-Dirac function $f(E-\mu)$ is defined as:

$$f(x) = \left[1 + \exp\left(\frac{E-\mu}{k_B T}\right)\right]^{-1}, \tag{2.49}$$

where k_B is a Boltzmann constant of 1.38×10^{-23} $[\mathrm{m^2 kg\, s^{-2} K^{-1}}]$ and T is an electronic temperature. The equilibrium density matrix is computed using the contour integration method with the Fermi-Dirac function f expressed by a continued fraction representation [66].

The charge density in the C region is calculated by

$$n(\mathbf{r}) = n^{(\mathrm{CC})}(\mathbf{r}) + 2n^{(\mathrm{sC})}(\mathbf{r}) + n^{(\mathrm{ss})}(\mathbf{r}), \tag{2.50}$$

where the suffix s is L or R. The charge densities $n^{(\mathrm{CC})}(\mathbf{r})$, $n^{(\mathrm{sC})}(\mathbf{r})$, and $n^{(\mathrm{ss})}(\mathbf{r})$ are contributed from the basis functions located in the central, the lead and central, and the lead regions, respectively. Among three charge contributions, the charge densities $n^{(\mathrm{sC})}(\mathbf{r})$ and $n^{(\mathrm{ss})}(\mathbf{r})$ are calculated by the conventional band calculations for the leads and they are independent on the SCF iteration. The charge density in the C region is calculated by the equilibrium density matrix $\rho^{(\mathrm{eq})}$ given by

$$n^{(\mathrm{CC})}(\mathbf{r}) = \sum_{i,j} \phi_i(\mathbf{r})\phi_j^*(\mathbf{r})\rho^{(\mathrm{eq})}, \tag{2.51}$$

where i and j are indices for the site, and ϕ is the basis function. The total charge density is obtained by the summation of the $n(\mathbf{r})$ over the spin degree of freedom.

The Hartree potential in the C region is calculated under the boundary condition that the Hartree potential at the boundary between C and L_1 (R_1) regions is the same as that of the lead. The Hartree potential in the lead regions is calculated using the conventional band calculation before the SCF calculation using the Green function. The Hartree potential for the C region under the boundary condition is efficiently evaluated by a combination of the two-dimensional Fast Fourier Transform (FFT) and a finite difference method. The majority part of the Hartree potential is given by the neutral atom potential, which depends only on the

atomic structure and atomic species. The effect of the relaxation of charge distribution on the Hartree potential is taken into account by the remaining minority part of the Hartree potential δV_{H}, which is defined as the Coulomb potential for the $\delta n(\mathbf{r})$, given by the Poisson equation:

$$\nabla^2 \delta V_{\mathrm{H}}(\mathbf{r}) = -4\pi\delta n(\mathbf{r}), \tag{2.52}$$

where $\delta n(\mathbf{r})$ is defined by the difference between the total charge density $n(\mathbf{r})$ given by Eq. (2.50) and the total atomic electron density $n^{(a)}(\mathbf{r})$ as follows:

$$\delta n(\mathbf{r}) = n(\mathbf{r}) - n^{(a)}(\mathbf{r}), \tag{2.53}$$

where $n^{(a)}(\mathbf{r})$ is calculated by superposition of each atomic electron density $n_i^{(a)}(\mathbf{r})$ at atomic site i. The obtained Hartree potential V_{H} is used as the second term in the right side of Eq. (2.14) and we can calculate the Hamiltonian and overlap matrices.

2.3.3. Non-equilibrium state

The density matrix in the nonequilibrium state of the C region is evaluated by

$$\rho^{(\mathrm{neq})} = \rho^{(\mathrm{eq})} + \Delta\rho \,, \tag{2.54}$$

where $\Delta\rho$ is defined by

$$\Delta\rho = \frac{1}{2\pi}\int_{-\infty}^{\infty} dE\, G_C(E+i\epsilon)\Gamma_{s_1}(E)G_C(E-i\epsilon)\Delta f(E) \,, \tag{2.55}$$

with

$$\Gamma_{s_1}(E) = i\left[\Sigma_{s_1}(E+i\epsilon) - \Sigma_{s_1}(E-i\epsilon)\right], \tag{2.56}$$

and

$$\Delta f(E) = f\left(E-\mu_{s_1}\right) - f\left(E-\mu_{s_2}\right), \tag{2.57}$$

where $s_1 = R$ and $s_2 = L$ if $\mu_L < \mu_R$ and $s_1 = L$ and $s_2 = R$ if $\mu_L \geq \mu_R$. The Fermi-Dirac function f in Eq. (2.57) is defined by Eq. (2.49). The formula is based on two assumptions: (i) the occupation of the wave functions incoming from the L or R region still obeys the Fermi-Dirac function with the L or R chemical potential even in the C region; (ii) the states in the C region is in equilibrium in the energy range below the lower chemical potential (μ_L or μ_R). The imaginary part ϵ is used for smearing the integrand in Eq. (2.55) and its convergence was discussed in Fig. 3 [62]. It is necessary for a relatively large ϵ to avoid the numerical instabilities in the SCF iteration, but the large ϵ suffers the results such as the Mulliken population. The ϵ = 0.01 eV is the best choice to compromise between the accuracy and efficiency for the discussed case in Ref. [62]. The careful choice of the ϵ is necessary especially for a system having spiky DOS in the integration range. The source-drain bias voltage V_b is defined by

$$V_b = (\mu_L - \mu_R)/e. \tag{2.58}$$

We ignore the distortion of the wave functions by the applied electric field, which is called the Stark effect. It is easily incorporated by adding a constant electric potential V_b to the Hartree potential in the R region. The Hamiltonian matrices and the boundary conditions are replaced by adding the constant potential. The gate voltage $V_g(x)$ can be treated by adding an electric potential defined by the similar form of the image charges as follows:

$$V_g(x) = V_g^{(0)} \exp\left[-\left(\frac{x - x_c}{d}\right)^8\right], \tag{2.59}$$

where $V_g^{(0)}$ is a constant value corresponding to the applied gate voltage, x_c is the position of the center of the C_0 region, and *d* is the length of the unit vector along the *a* axis for the C_0 region.

After the SCF calculation converges in terms of the potential and the charge density, the spin- and $\boldsymbol{k}$-resolved transmission $T_\sigma^{(\boldsymbol{k})}(E)$ is defined by

$$T_\sigma^{(\boldsymbol{k})}(E) = \mathrm{Tr}\left[\Gamma_{\sigma,L_1}^{(\boldsymbol{k})}(E) G_{\sigma,C}^{(\boldsymbol{k})}(E + i\epsilon) \Gamma_{\sigma,R_1}^{(\boldsymbol{k})}(E) G_{\sigma,C}^{(\boldsymbol{k})}(E - i\epsilon)\right]. \tag{2.60}$$

The spin-dependent transmission $T_\sigma(E)$ is evaluated as the numerical integration of the $T_\sigma^{(\boldsymbol{k})}(E)$ over the first Brilloiuin zone:

$$T_\sigma(E) = \frac{1}{\mathrm{V_C}} \int_{BZ} dk^3 T_\sigma^{(k)}(E). \tag{2.61}$$

The current *I* under a bias voltage $V_b = (\mu_L - \mu_R)/e$ is evaluated by

$$I = \sum_\sigma \frac{e}{h} \int_{-\infty}^{\infty} T_\sigma(E) \Delta f(E) dE. \tag{2.62}$$

This integration is performed in the energy window from μ_L to μ_R at the zero temperature ($T = 0$), because $\Delta f(E) = 1$ at $\mu_L < E < \mu_R$ and $\Delta f(E) = 0$ at else E. At the finite temperature ($T > 0$), the energy window is smeared according to the Fermi-Dirac function. Thus we can consider the effect of the electronic temperature for the current.

Chapter 3. Graphene/metal electrode hybrid structures

In this chapter, we investigate the electronic transport properties of the hybrid structures of graphene/metal electrodes. We firstly present a problem of high contact resistance between graphene and metal electrodes, and introduce the previous studies on the graphene/metal interfaces in Sec. 3.1. We then demonstrate the computational details and employed models in Sec. 3.2 and 3.3, respectively. In Sec. 3.4, we show results and develop discussions for the electronic transport properties of the hybrid structures of graphene/metal electrodes. Finally, we present conclusion of this chapter in Sec. 3.5.

3.1. Introduction

3.1.1. Contact resistance

High contact resistance between graphene and metal electrodes is one of serious problems for realizing graphene-based electronic devices. The small density of states (DOS) of graphene around the Fermi level E_F limits the contact resistance. The charge transfer between graphene and metal electrodes results in large E_F shift of graphene due to the small DOS of graphene. The E_F shifts by 0.47 eV upon the charge transfer of 0.01 electrons per carbon atom [68]. The charge transfer was experimentally reported as the shift of the Dirac point during the deposition of the metal nanoparticles on the graphene channel [69]. The anti-symmetric conductivity dependence on the back-gate voltage also supports the charge transfer [70-72]. The charge transfer region ascribed to the small DOS results in additional resistance produced by *p-n* junctions [73].

We summarize two typical methods of experimental measurements of the contact resistance in Fig. 3.1. Figure 3.1(a) shows the four-probe method. The source-drain voltage V_{sd} includes the voltage drop from not only the channel but also the contacts. The contact resistance R_c is evaluated by

$$R_c = \frac{1}{2}(R_{tot} - R_{ch} \times L/l\,), \tag{3.1}$$

where R_{tot} is the total resistance measured between the source and the drain electrodes, and R_{ch} is the channel resistance measured between the third and the fourth electrodes. Figure 3.1(b) shows the transfer

length method. The resistances between the nearest-neighbor electrodes are plotted as a function of each channel length. In the limit of a zero distance, the residual resistance corresponds with $2R_c$ if all the contacts are equivalent. The residual resistance can be found from the graph by extrapolating to the zero distance.

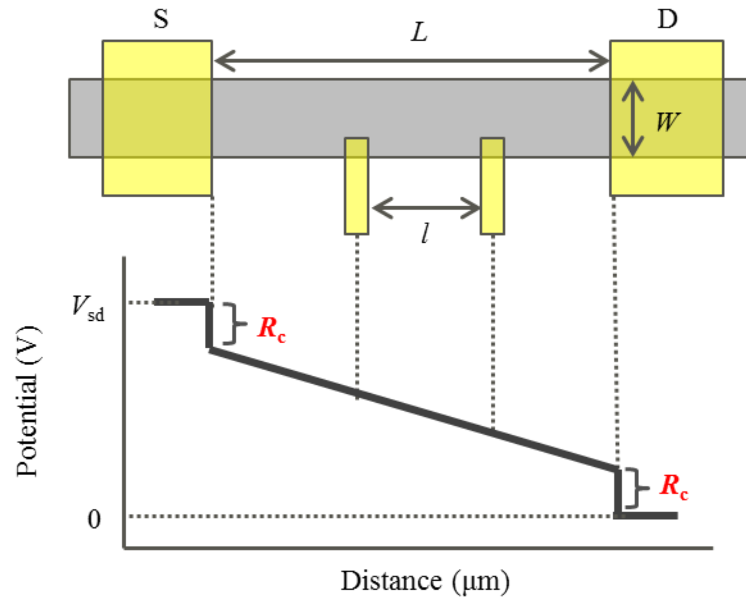

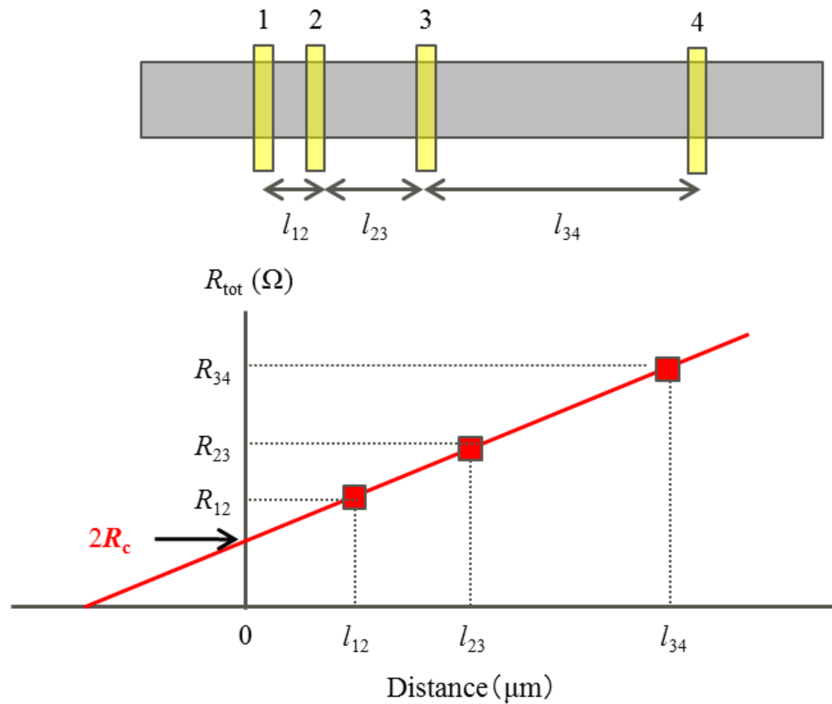

Fig. 3.1: Schematic views of two methods for the measurement of the contact resistance R_c. (a) Four-probe method. (b) Transfer length method. The gray and yellow rectangles represent the channel and the electrodes.

3.1.2. Experimental studies

It has been experimentally reported that the contact resistance depends on the metal species [74-83]. Large variations have also been found in the contact resistance even within the same species. The contact resistivities measured by the four-probe method are 10^2-10^3 Ωμm for Ni electrodes, while they are 10^3-10^5 Ωμm for Ti/Au and Cr/Au electrodes [74]. The Ti/Au electrode consists of the bottom layer of Ti with 10 nm thickness and the upper layer of Au with 20 nm thickness. The Ti is employed because of the strong binding to the insulating substrate and considered to be also attached to the graphene channel. The Au layer blocks the oxidation of the Ti layer. However, a lot of fundamental properties is still unknown such as the work function and the detailed electronic states in the interface between the alloys and graphene. Nagashio *et al.* also reported the contact resistivity of 50 Ωμm for the Au electrode using the resist-free metal deposition technique [77]. For the resist-free metal/graphene contacts, the DOS of graphene is maintained for the Au electrode, while it is largely modulated for the Ni electrode. The low contact resistivity for the Au electrode is ascribed to the increasing of DOS of graphene by the back-gate modulation.

The electron-beam lithography is often utilized to form electrical contacts onto graphene. For examples [74], the contact metals were thermally evaporated on the resist-patterned graphene in a chamber with a background pressure of 10^{-5} Pa. To remove the resist residuals, the devices were annealed in a H_2-Ar mixture at 300 ℃ for 1 hour. The electrical measurements were performed in a vacuum with a source/drain bias voltage of 10 mV and a gate voltage from -20 V to 40 V.

3.1.3. Theoretical studies

Many theoretical studies reported geometries and electronic structures of interfaces between graphene and metal surfaces [84-100]. The stable structures of the graphene on various metal surfaces were examined using the first-principles calculations [84]. Metal species are classified into two groups according to the amount of the interaction with graphene. Al, Cu, Ag, Pt, and Au (Group I) weakly interact with graphene: the equilibrium spacing d between the graphene and the metal surfaces are 0.32-0.34 nm and the characteristic band structures of original graphene retain in the hybrid structures. On the other hand, Ti, Co, Ni and Pd (Group II) strongly interact with graphene: d are 0.20-0.23 nm and the band structures of the hybrid structures are strongly modified from the original structures, resulting in the absence of the linear bands.

Transport properties have also been studied actively. Previous works are classified into three by the employed models in Fig. 3.2: (a) with left and right leads containing graphene and metals [101-103], (b) with one-side leads containing graphene and metals, and other-side containing only graphene [104-109], and (c) with left and right leads containing only metals, where there are graphene edges (graphene nanoribbon) [110, 111]. In this thesis, we apply the model (c) to investigate the interface effect to the electronic transport in the realistic two-probe structure. For the model (c), it is found that the contact resistance of the Ni-graphene system is one order of magnitude lower than that of Cu-graphene using first-principles electronic transport calculations [110]. In Cu-graphene contact, the transmission spectra correspond with the band structures of the isolated graphene and only the symmetric states with respect to the Cu-s state contribute to transport. In Ni-graphene contact, however, the band structures are strongly modified from that of an isolated graphene due to the hybridization between the graphene π-orbitals and the Ni d-orbitals. It has been investigated the effect of contact area on the transport through the interface [111]. For the Cu electrode, the current increases at a low bias voltage as the contact area increases due to the charge transfer between the graphene and the Cu surface. For the Ni electrode, however, the current monotonically increases as the contact area increases due to the strong π-d hybridization.

Although much effort has been devoted to reveal the fundamentals of the hybrid structures, the comprehensive understanding has not yet been addressed. Therefore, in this chapter, we aim to give

theoretical insight into the fundamental properties of the hybrid structures for advancing the interface science related with the two-dimensional thin films. We investigate the electronic transport properties of the graphene channels bridging two electrodes using the first-principles calculations. We examine armchair graphene nanoribbons (AGNRs) with over 10 nm width. Au (Group I) and Ti (Group II) are employed as the metal electrodes.

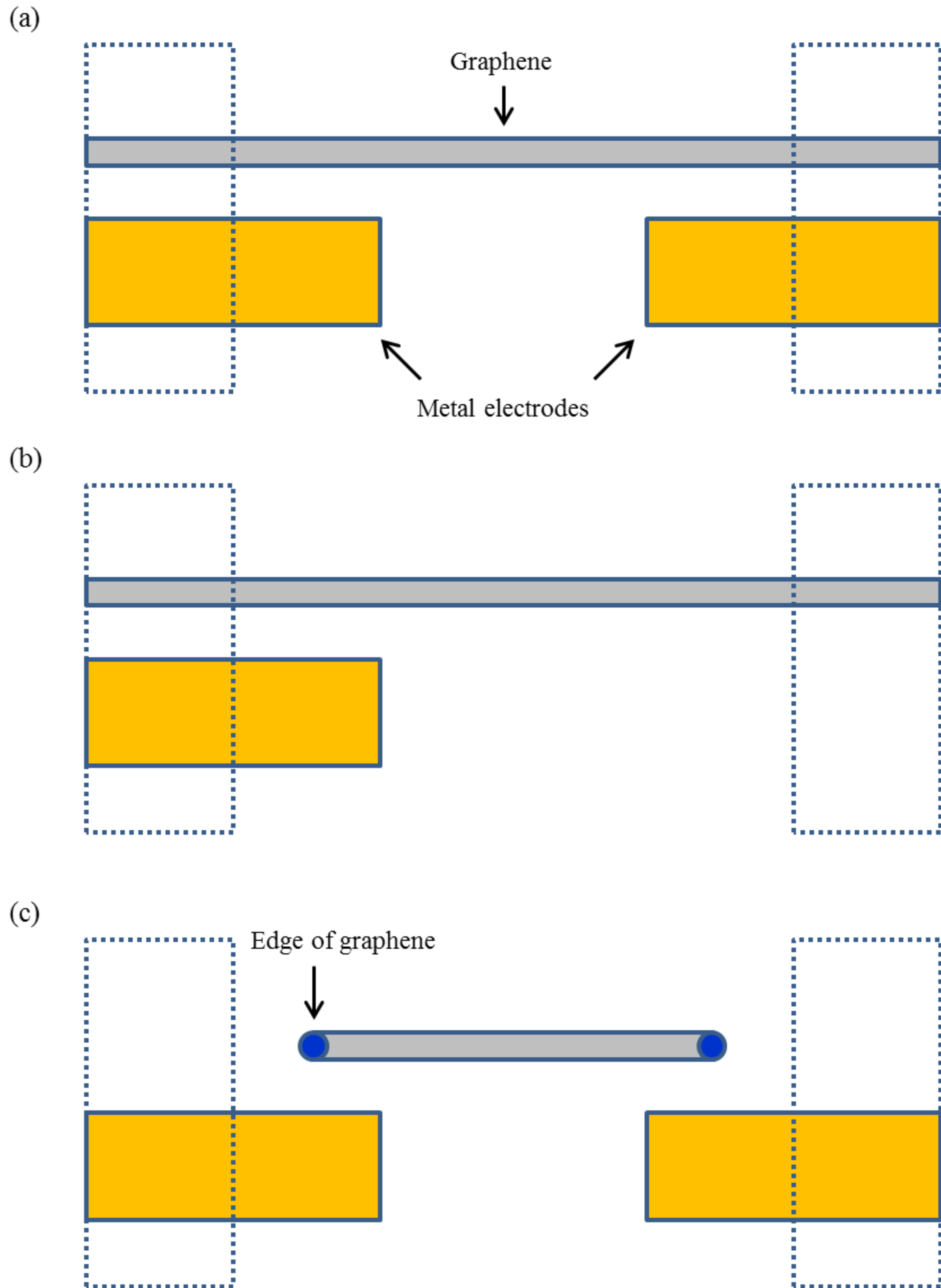

Fig. 3.2: Three models employed in previous works for the transport calculations. (a) Left and right leads containing graphene and metals, (b) one-side leads containing graphene and metals, and other-side containing only graphene, and (c) left and right leads containing only metals, where there are graphene edges (graphene nanoribbon). The dotted rectangles represent the leads, which correspond with L_0 and R_0 in Sec. 2.3.

3.2. Computational details

For all calculations, we use the DFT code OpenxMX [53], which allows us to perform large-scale calculations on massively parallel computers [112, 113]. We use the GGA with Perdew-Burke-Ernzerhod functional form for describing the exchange-correlation energy among interacting electrons [51]. The electron-ion interaction is described by norm-conserving pseudopotentials [61] with partial core correction [114]. PAOs centered on atomic sites are used as the basis function set for expanding molecular orbitals [53].

For geometry optimizations and energy band structure calculations, we use the PAOs specified by C6.0-*s*2*p*2*d*1, H5.0-*s*2*p*1, Au7.0-*s*2*p*2*d*2*f*1, and Ti7.0-*s*3*p*3*d*2. For examples, C6.0-*s*2*p*2*d*1 indicates the PAO of the carbon atom with the cutoff radii of 6.0 Bohr and with two *s*, two *p*, and one *d* components. Geometric structures of interfaces of graphene and metal surfaces are optimized under a repeated slab model with 13 Å vacuum spacing to exclude the effects arising from periodic images. The convergence criterion for forces acting on atoms is 0.1 eV/nm.

For transport calculations, we employ the NEGF method under the finite bias voltage between two electrodes [62]. We use a smaller set of PAOs, i.e. C-*s*1*p*2, H-*s*1*p*1, Au-*s*1*p*2*d*1, and Ti-*s*1*p*2*d*1, to reduce the computational cost. Note that the reduced set of PAOs can maintain the quantitative and qualitative accuracy of the transport calculations. Figure 3.3 shows the comparison of the energy band structures of graphene on Au(111) surface modeled by the slab with four layers using the reduced set of PAOs (green lines) and the non-reduced set of PAOs (red lines). The energy shift of the Dirac point ΔE_D in graphene at the *K* point is 0.34 eV for the reduced set and 0.37 eV for the non-reduced set. The cutoff radii are the same as those used in the band calculations. We use 151 *k*-points along the perpendicular to the transport direction. The electronic temperature is 300 K.

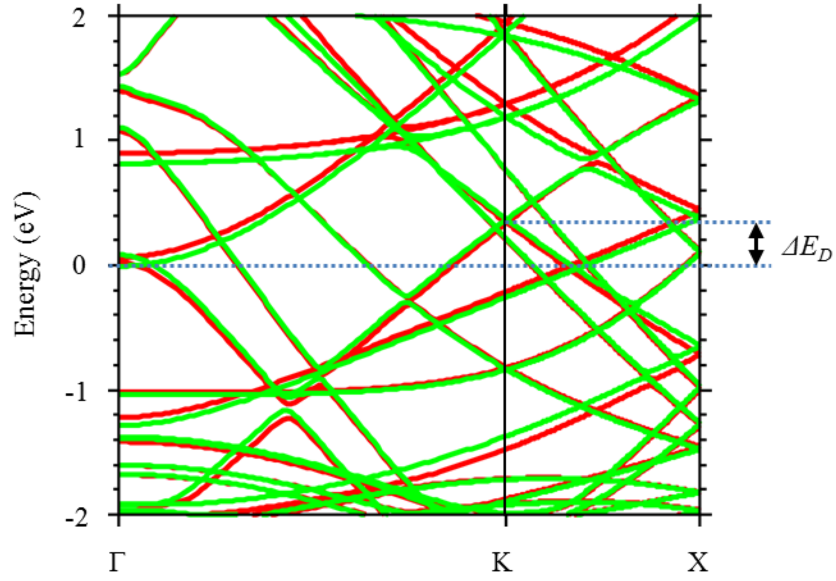

Fig. 3.3: Energy band structures of graphene on Au(111) surface slab with four layers using the set of PAOs specified by C6.0-*s*2*p*2*d*1, H5.0-*s*2*p*1, and Au7.0-*s*2*p*2*d*2*f*1 (green lines) and C-*s*1*p*2, H-*s*1*p*1, and Au-*s*1*p*2*d*1 (red lines). The zero energy is set to the Fermi energy.

3.3. Models

3.3.1. Equilibrium lattice parameters

Before the calculation for the interfacial structures, we examine equilibrium lattice parameters of Au in fcc crystal, Ti in hcp crystal, and graphene (Table. 3.1). Our GGA results are found to be enough to describe the lattice parameters within 3 % errors from the experimental values.

Table 3.1: Lattice parameters (in Å) of Au, Ti, and graphene. The "Other LCAO" and "Plane wave" are results within GGA.

	Our calc. (GGA)	Our calc. (LDA)	Other LCAO	Plane wave	Exp.
Au	4.17	4.06	4.18[a]	4.15[b]	4.08[c]
Ti: *a*	2.93	2.86	2.99[f]	2.93[e]	2.95[c]
c	4.65	4.53	4.75[f]	4.65[e]	4.68[c]
Graphene	2.47	2.45	2.49[g]	2.47[d]	2.46[h]

[a]Reference [115].

[b]Reference [116].

[c]Reference [117].

[d]Reference [78].

[e]Reference [118].

[f]Reference [119].

[g]Reference [1209].

[h]Reference [121].

3.3.2. Interfacial structures of graphene/metal surface

We optimize graphene adsorbed on Au(111) and Ti(0001) surfaces as shown in Fig. 3.4. The interface between metals and graphene is simulated by the repeated slab model consisting of four atomic layers of the metals and a single graphene sheet. A commensurability condition is imposed between lateral periodicities of graphene and that of the metal surfaces. Accordingly, the rectangle unit cell contains the 2x2√3 lateral periodicity of graphene and the √3x3 lateral periodicity of Au(111) surface and Ti(0001) surface. Since there are lattice mismatches between graphene and metal surfaces, the lateral lattice parameter of the Au(111) and the Ti(0001) surface is compressed by 3.23 % and 2.65 % from the equilibrium lattice parameter, respectively. The lattice constant a of graphene is 2.47 Å. The artificial lattice compression causes a slight change in the work function from 5.30 to 5.18 eV for the Au(111) surface. Compared the energy band structure of the compressed Au (111) [Fig. 3.5(b)] with that of equilibrium Au(111) [Fig. 3.5(a)], we have found that the energy of the unoccupied state extended throughout the surface [Fig. 3.5(c)] drops from 0.45 eV to just above the Fermi energy because of the lattice compression. Under the optimum structure of both metal surfaces, one carbon atom is situated above the topmost metal atom and the other is on a bridge site [84].

The equilibrium spacing d between graphene and the topmost metal atom is 0.37 nm for the Au(111) surface and 0.20-0.22 nm for the Ti(0001) surface. The binding energy is evaluated by

$$E_b = E(\mathrm{G/M}) - \{E(\mathrm{G}) + E(\mathrm{M})\}, \qquad (3.2)$$

where E(G/M), E(G), and E(M) are the total energies of the graphene on the metal, the isolated graphene, and the isolated metal, respectively. Calculated energies E_b are 0.016 eV/carbon atom on the Au(111) surface and 0.312 eV/carbon atom on the Ti(0001) surface. These results of d and E_b indicate that the graphene is weakly and strongly bound to the Au(111) and Ti(0001) surfaces, respectively.

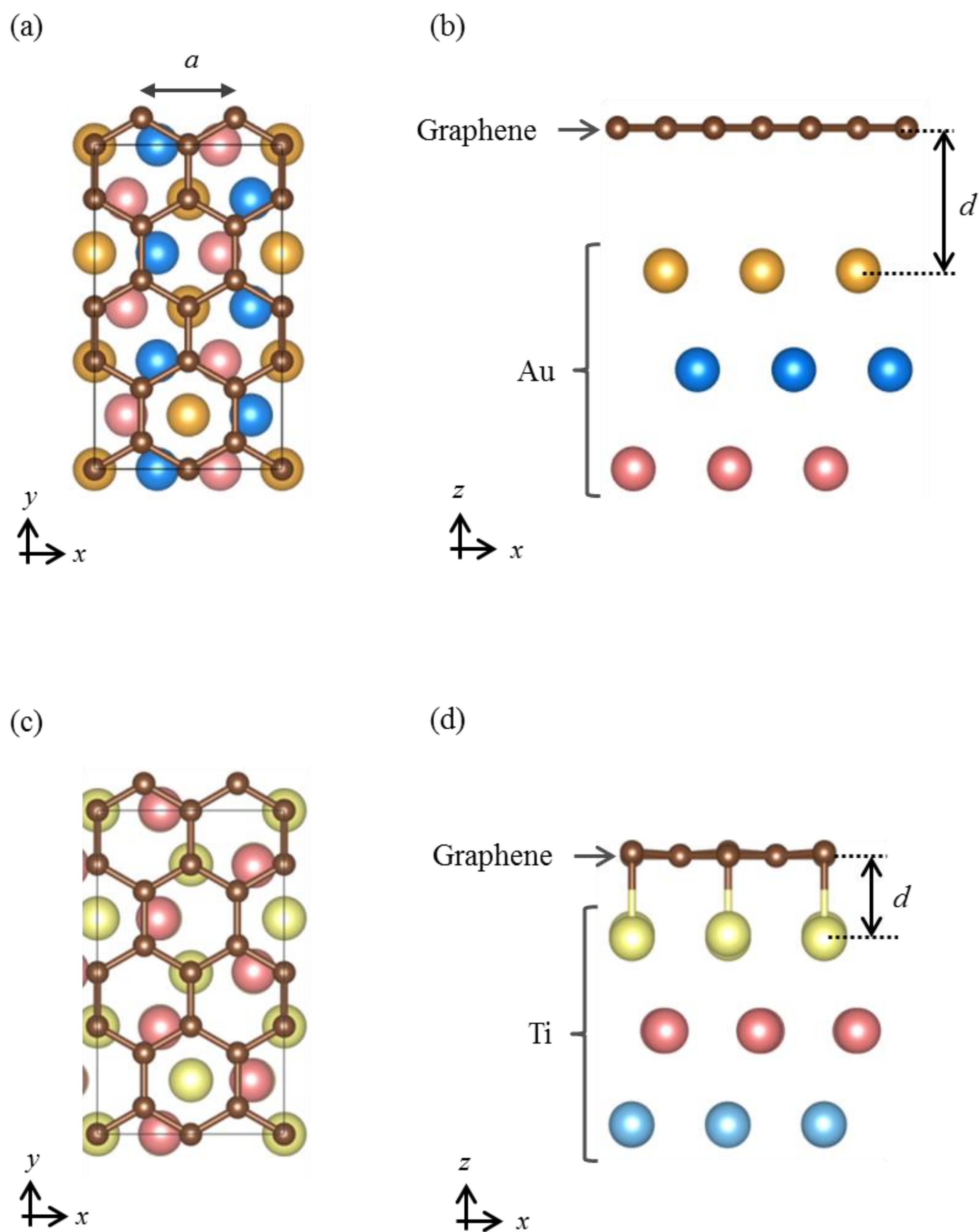

Fig. 3.4: (a) Top and (b) side views of the stable geometry of graphene/Au-fcc(111) interface. (c) Top and (d) side views of the stable geometry of graphene/Ti-hcp(0001) interface.

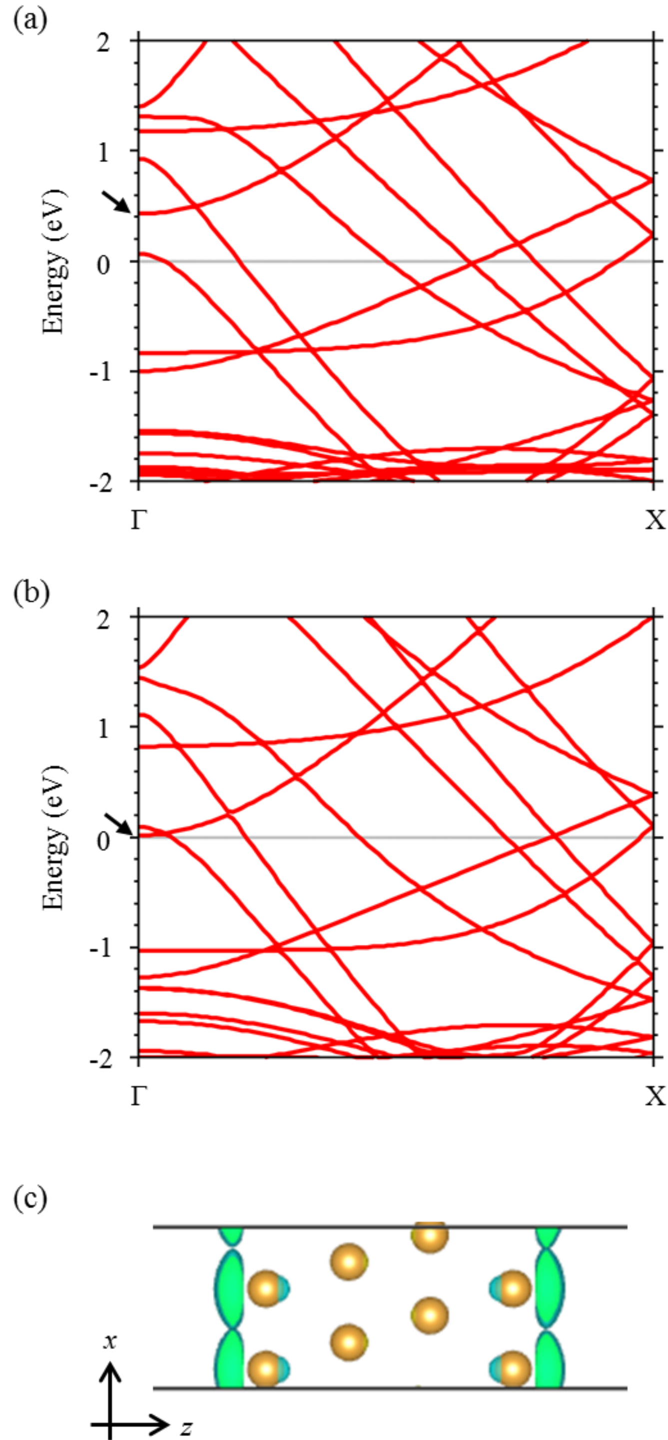

Fig. 3.5: Energy band structures of Au(111) surface simulated by the slab model with four-layers under (a) the equilibrium lattice constant of Au and (b) the compressed lattice constant to match the graphene lattice. (c) A wave function of the band pointed by arrows in (a) and (b) at the Γ-point. The yellow spheres represent Au atoms.

3.3.3. Electronic properties of graphene/metal hybrid structures

Figure 3.6(b) shows the band structure of the graphene on Au(111). Even by forming the complex, the characteristic band structure of the isolated graphene [Fig. 3.6(a)] is kept on the Au(111) due to the weak interaction. The Dirac point of graphene shifts upward by ΔE_{D} = 0.37 eV. Thus holes are injected into graphene by the Au(111) surface. This *p*-type doping is mainly ascribed to the higher work function of the Au(111) surface (φ_{M} = 5.18 eV) compared with that of graphene (φ_{G} = 4.06 eV). The charge transfer between metal and graphene forms an interface dipole layer and a potential step derived from the dipole. To visualize the charge redistribution, we examine the difference of the electron densities Δn by the formation of the interface:

$$\Delta n = n_{\mathrm{M/G}} - (n_{\mathrm{M}} + n_{\mathrm{G}}), \tag{3.3}$$

where $n_{\mathrm{M/G}}$, n_{M}, and n_{G} denote the electron densities of the graphene/metal hybrid structure, the clean metal surface, and the isolated graphene, respectively. Here the structures of the clean metal surface and the isolated graphene are assumed to be the same structures as the graphene/metal hybrid structure. Figures 3.7(a) and 3.7(b) show isosurfaces of Δn and plane-averaged Δn, respectively. We have found that the charge transfer mainly occurs in the interlayer region between the graphene and the topmost Au(111) layer. The charge accumulation just below the bottom layer of Au(111) is considered to be ascribed to the artificial electric field arising from the periodic boundary condition, as discussed details in Sec. 3.3.5.

Figure 3.6(c) shows the band structure of the graphene on Ti(0001). Contrary to the Au(111) surface, the linear dispersion bands around the Fermi energy disappear owing to the strong *π-d* interaction. Electrons are injected into graphene by the Ti(0001) surface because of the small work function of the Ti.

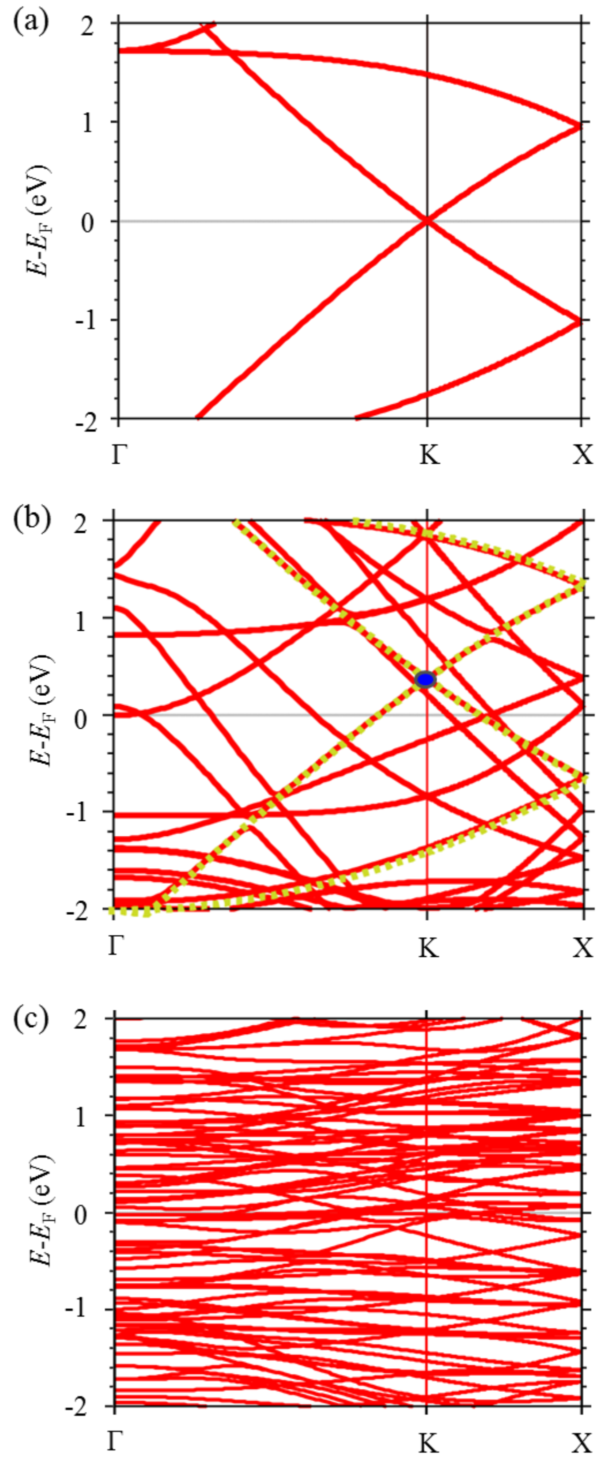

Fig. 3.6: Energy band structures of (a) the isolated graphene, (b) the graphene on Au(111) surface, and (c) the graphene on Ti(0001) surface. The dotted yellow lines in (b) represent the band structure of the isolated graphene with the upward energy shift by 0.37 eV.

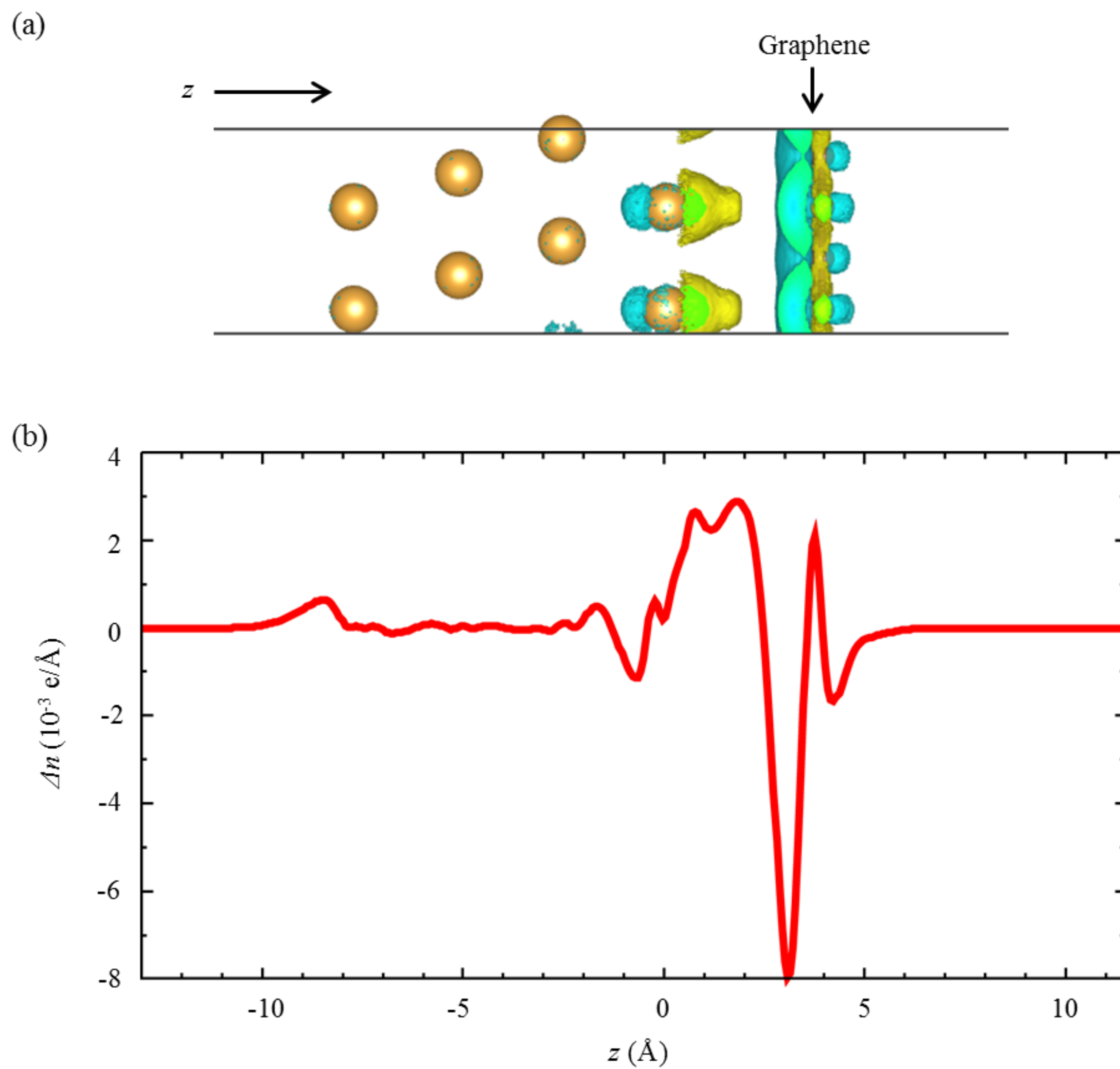

Fig. 3.7: (a) Isosurfaces and (b) plane-averaged electron density of Δn per unit cell for the graphene/Au(111) interface. The yellow and aqua isosurfaces in (a) denote the charge accumulation and depletion, respectively.

3.3.4. Discussion about the effect of different equilibrium interfacial spacing

The calculated d and E_b in GGA and LDA for the Au(111) and the Ti(0001) are summarized in Tables 3.2 and 3.3, respectively. The ΔE_D for the graphene on Au(111) is also shown in Table 3.2. The LDA gives smaller ΔE_D than the GGA due to the smaller d. As discussed in Ref. [84], the ΔE_D can be written as a function of the d as following (d_0 is a constant):

$$\Delta E_D(d) = \pm\frac{\sqrt{1+2\alpha D_0(d-d_0)|W_M-W_G-\Delta_c(d)|}-1}{\alpha D_0(d-d_0)}, \quad (3.4)$$

where the sign of ΔE_D is determined by the sign of $(W_M - W_G - \Delta_c)$. The W_M and W_G are work functions of the clean metal surface and the graphene, respectively. The Δ_c describes the short-range interaction, which is originated from the hybridization between the metal and the graphene states and vanishes exponentially with increasing d. For an energy range from -1 eV to 1 eV with respect to the Dirac points, the graphene DOS is described well by a linear function:

$$D(E) = D_0|E|, \quad (3.5)$$

with D_0 = 0.09/(eV^2 unit cell). By using a plane capacitor model, we can describe the charge transfer contribution to the potential step as

$$\Delta_{\mathrm{tr}}(d) = \alpha N(d) z_d, \quad (3.6)$$

where $\alpha = e^2/\epsilon_0 A = 34.93$ eV/Å with A = 5.18 Å^2 as the area of the unit cell, $N(d)$ is the number of electron per unit cell transferred from graphene to the metal, and z_d is the effective distance between the sheets of transferred charge on graphene and the metal. Under a thick contamination layer such as water and a metal oxide with the effective dielectric constant κ, the parameter α is replaced by α/κ.

The spacing between graphene and Au electrode sensitively affects the current density which is associated with the overlap of the wave functions between them. In the present calculation, the spacing between graphene and Au electrode is slightly overestimated because of the choice of GGA functional which could not reproduce the dispersive force. The van der Waals (vdW) forces play an important role in weakly bonded systems. Indeed, several previous DFT calculations with the vdW corrections showed the narrower optimum spacing d of 0.32-0.36 nm, whose variation is ascribed to the difference of the functionals [92, 93, 116]. The narrower d shifts the energy of the Dirac point downward. For examples, the ΔE_D = -0.05 eV is obtained at d

= 0.32 nm [116], while our GGA calculation results in the ΔE_D = 0.37 eV at d = 0.37 nm. The difference of ΔE_D in considering the effect of the vdW forces is mainly ascribed to the difference of d.

Table 3.2: Calculated equilibrium spacing d and binding energy E_b between graphene and Au(111) surface, and the Dirac point shift ΔE_D by forming the complex. The d is defined as the distance in z direction between the carbon atoms of the graphene and the relaxed positions of the topmost Au layer. The E_b is evaluated as the energy per carbon atom to remove the graphene from the Au surface.

	Our calc. (GGA)	Our calc. (LDA)	Plane wave (LDA)	Plane wave (vdW correction)	Exp.
d (nm)	0.37	0.33	0.33[a]	0.357[b]	0.5[e]
			0.34[b]	0.377, 0.369, 0.321, 0.329[c]	
			0.337, 0.335[d]	0.321, 0.322, 0.320[d]	
E_b (meV)	16	52	30[a]	38[b]	-
			31[b]	47, 49, 80, 59[c]	
			~30[d]	~110[d]	
ΔE_D (eV)	0.37	0.06	0.19[a]	0.21[b]	-
			0.26, 0.25[d]	0.08, 0.00, -0.16, 0.07[d]	

[a]Reference [84].

[b]Reference [92].

[c]Reference [94]. (including various functionals of vdW corrections)

[d]Reference [122]. (including various lattice parameters)

[e]Reference [123].

Table 3.3: Calculated equilibrium spacing d and binding energy E_b between graphene and Ti(0001) surface. The d is defined as the distance in z direction between the carbon atoms of the graphene and the relaxed positions of the topmost Ti layer. The E_b is evaluated as the energy per carbon atom to remove the graphene from the Ti surface.

	Our calc. (GGA)	Our calc. (LDA)	Plane wave (LDA)
d (nm)	0.20-0.22	0.19-0.21	0.21 [a]
E_b (meV)	312	527	327 [a]

[a]Reference [84].

3.3.5. Discussion about the effect of an artificial electric field

In our model of graphene on the Au(111) slab, the electrostatic potentials on the two sides of the slab are different at the cell boundary. In this model, thus, an artificial uniform electric field is introduced in the supercell in order to cancel the potential jump at the boundary under the periodic boundary conditions on the electrostatic potential.

Figure 3.8(a) shows our model of the unit cell of graphene on the Au(111) surface. The potential gradient of 0.06 V/Å is found in the vacuum region indicated by an arrow in Fig. 3.8(b). This potential gradient corresponds with the existence of the artificial electric field in the vacuum region due to the periodic boundary condition. To check the effects of this artificial field on physics, we consider a new model of adding a reversal slab of graphene/Au(111) in the vacuum region as shown in Fig. 3.8(d). Figure 3.8(e) shows that the electric field is canceled each other and the flat potential is observed in the vacuum region of this new model. Almost the same band structures are found in our model with the artificial electric field [Fig. 3.8(c)] and the new model without it [Fig. 3.8(f)]. The shift of the Dirac point ΔE_{D} is 0.37 eV for the former model and 0.36 eV for the latter model. We can conclude that the artificial electric field hardly affects the electronic structure in this case.

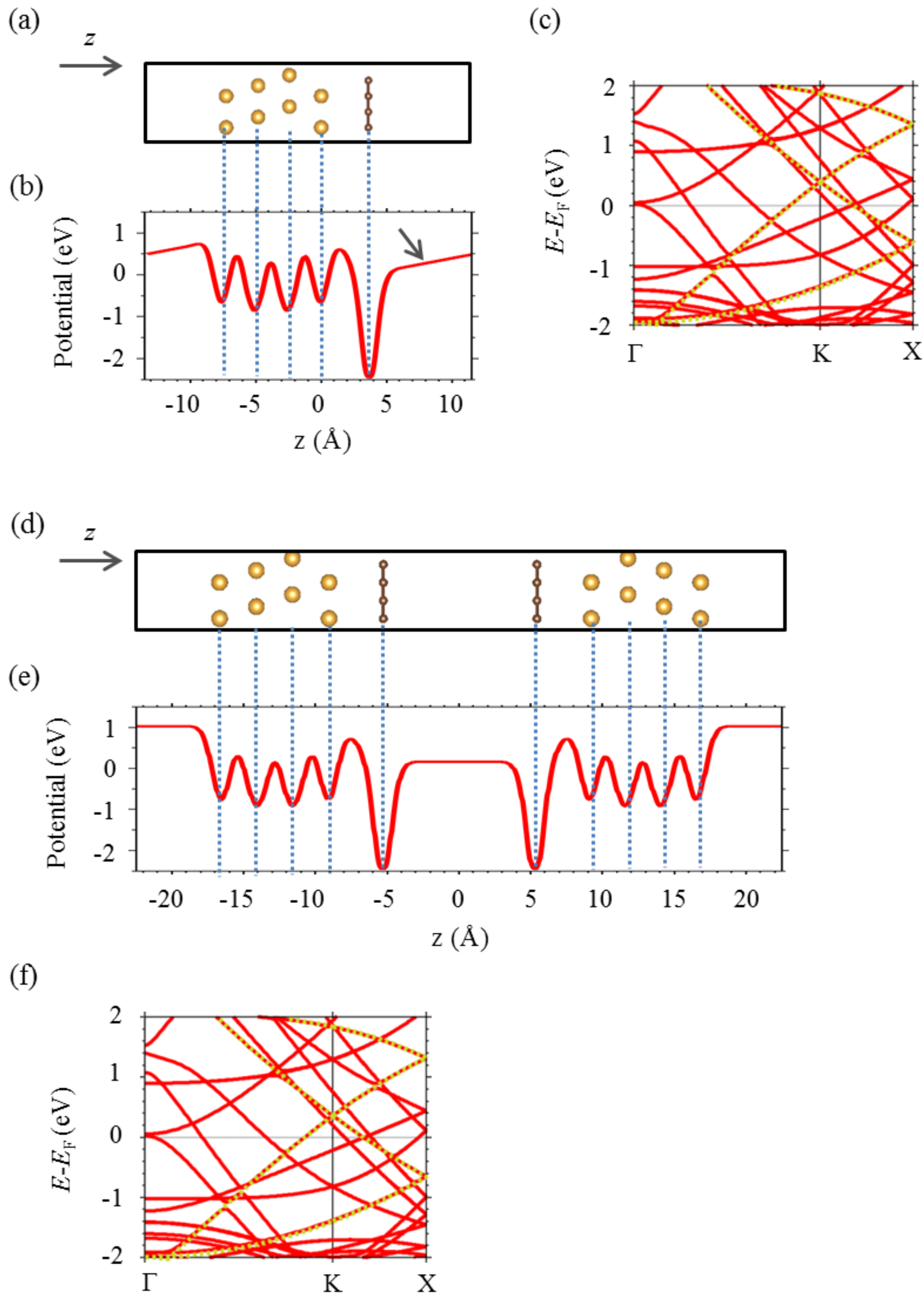

Fig. 3.8: (a) An unit cell of graphene on Au(111). (b) Potential along the z direction averaged in the xy-plane. It includes the Hartree and ionic potentials. (c) Band structure of the graphene on Au(111). (d)-(f) Same with (a)-(c) for the symmetric configuration of the graphene on Au(111), respectively.

3.3.6. Structural model for transport calculations

Figure 3.9 shows a structural model for simulating transport properties of the hybrid structure that consists of Au electrodes and an AGNR. The AGNRs with a width *W* ranging from 2.7 nm to 12.1 nm are bridged between two Au electrodes with the contact length L_{con} = 0.86 nm to elucidate the *W* dependence of the transport properties of AGNRs. All edge carbon atoms along the *y* direction are terminated by hydrogen atoms and the armchair edges are appeared in the contact region. Along the *y* direction, we impose the periodic boundary condition. *N* is defined as the number of C_2 dimer rows along the ribbon direction (*x* direction). Both sides of the unit cell in the *x* direction are connected to semi-infinite leads, which are denoted as the dashed rectangles in Fig. 3.9(b). The relaxed geometry of 4-layers slab of the clean Au(111) surface is employed as the geometry of Au(111) surface both in the leads and the scattering region. The interlayer spacing between the AGNR and the Au electrodes is set to 0.37 nm, corresponding to the equilibrium spacing between graphene and Au(111) surfaces. For the AGNR/Ti hybrid structures, similar models are used as shown in Fig. 3.10. The interlayer spacing is set to their equilibrium spacing of 0.20-0.22 nm.

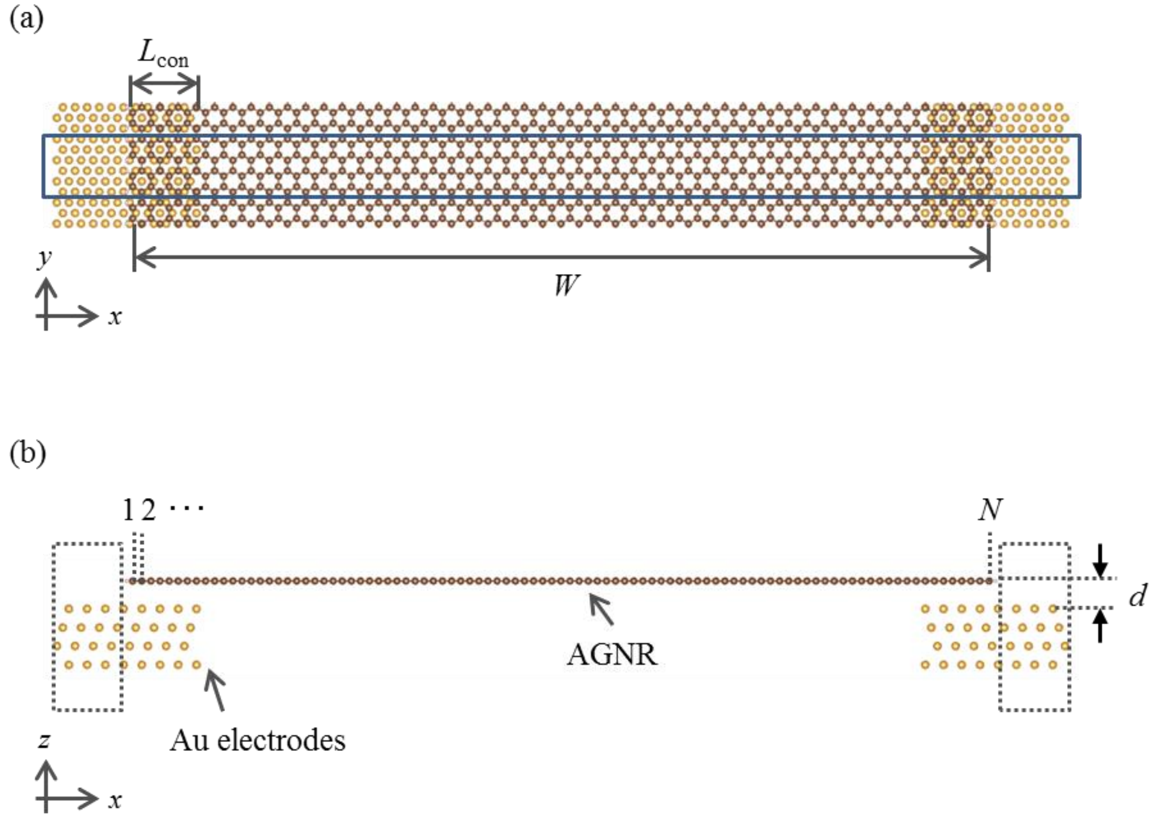

Fig. 3.9: (a) Top and (b) side views of the AGNR/Au hybrid structure. The AGNR with the number of C_2 dimer rows $N = 95$ ($W = 9.88$ nm) is bridged between two Au electrodes with the contact length $L_{con} = 0.86$ nm. The blue solid rectangle in (a) indicates the unit cell of the model. The dashed rectangles in (b) indicate the unit cells of leads. The interlayer spacing d is set to 0.37 nm. Although both sides in the transport direction (x) are connected to semi-infinite leads in actual calculations, only atoms of the center region are given. The khaki, white, and orange spheres represent the carbon, hydrogen, and gold atoms, respectively.

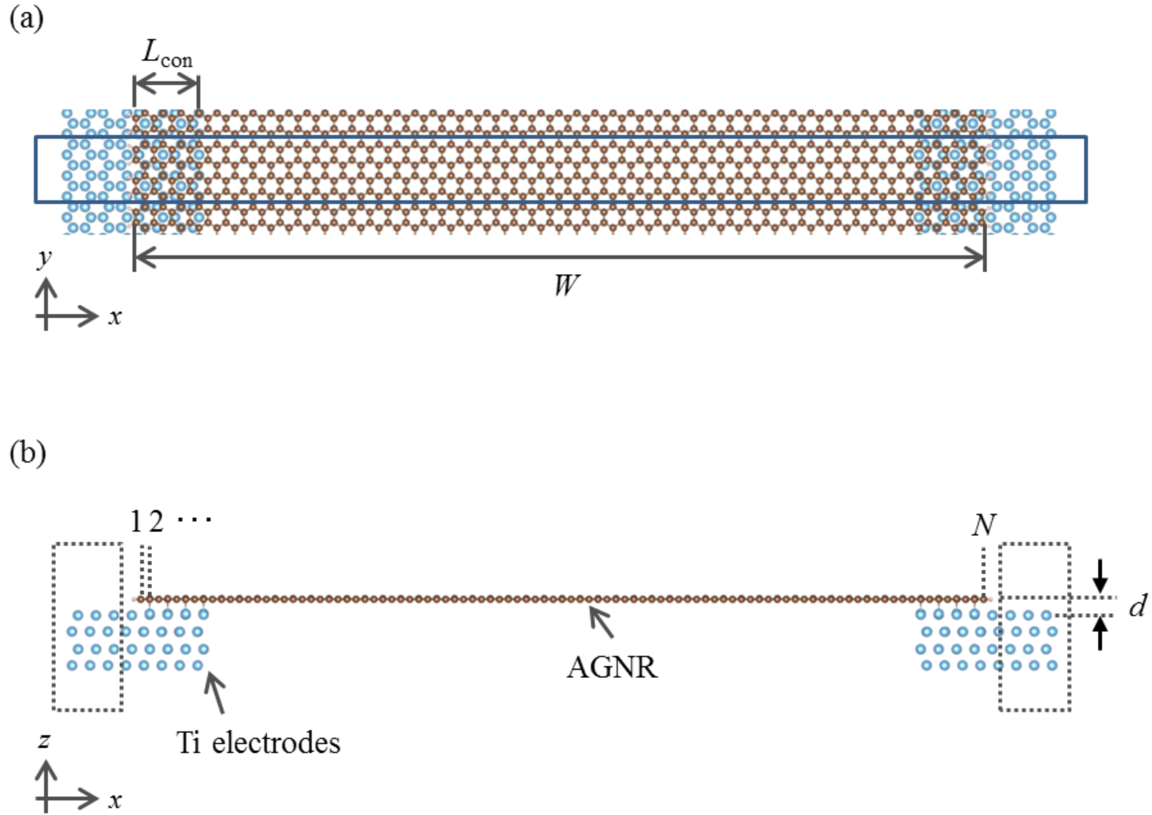

Fig. 3.10: (a) Top and (b) side views of the AGNR/Ti hybrid structure. The AGNR with the number of C_2 dimer rows N = 95 (W = 9.88 nm) is bridged between two Ti electrodes with the contact length L_{con} = 0.86 nm. The blue solid rectangle in (a) indicates the unit cell of the model. The dashed rectangles in (b) indicate the unit cells of leads. The interlayer spacing d is set to 0.20-0.22 nm. Although both sides in the transport direction (x) are connected to semi-infinite leads in actual calculations, only atoms of the center region are given. The khaki, white, and aqua spheres represent the carbon, hydrogen, and titanium atoms, respectively.

3.4. Results and discussions

3.4.1. Current densities for the hybrid structure of graphene/Au electrodes

We calculate a current density I under the bias voltage $V_b = (\mu_L\text{-}\mu_R)/e = 0.1$ V, where μ_L (μ_R) is the chemical potential of the left (right) electrode, without a gate voltage. The channel length of 10 nm and the operating voltage of 0.75 V are expected for the Si-CMOS technology trend in 2020 according to ITRS2013 [124]. The IBM reported that the carbon nanotubes FET with the 9 nm channel can be operated in 0.5 V [125]. In this thesis, we employ the bias voltage of 0.1 V for more low energy consumption devices envisioned in the graphene FET in the future.

Figure 3.11 shows the calculated current density I as a function of the ribbon width W for the AGNR/Au hybrid structure. The current density sensitively depends on the width of AGNR. The current density basically decreases with increasing the ribbon width. Furthermore, the current density rapidly oscillates with the number of C_2 dimer rows N along the ribbon direction in the narrow ribbons: the current density of AGNR with dimer rows $N = 3m+2$ is lower than those with $N = 3m$ and $3m+1$. More interestingly, the current densities still depend on the N family in the wide ribbons (W ~ 12nm): they are 24.1 A/m for $N = 99$ ($W =$ 12.10 nm), 23.0 A/m for $N = 97$ ($W = 11.85$ nm) and 30.3 A/m for $N = 95$ ($W = 11.60$ nm). The facts indicate that the transport properties of ANGR with Au electrodes sensitively depend on the tiny difference in their atomic structures. Therefore, the current density variation and contact resistance variation are expected to be essential in AGNR-FET with Au electrodes.

As mentioned in Sec. 3.3.4, by taking account the dispersive force into this calculation, the spacing between graphene and Au(111) surface will become narrower. The current is expected to increase. However, due to the weak interaction nature of the dispersive force, the quantitative nature of the current thorough the electrode and graphene is expected to retain even in calculations containing the dispersive force.

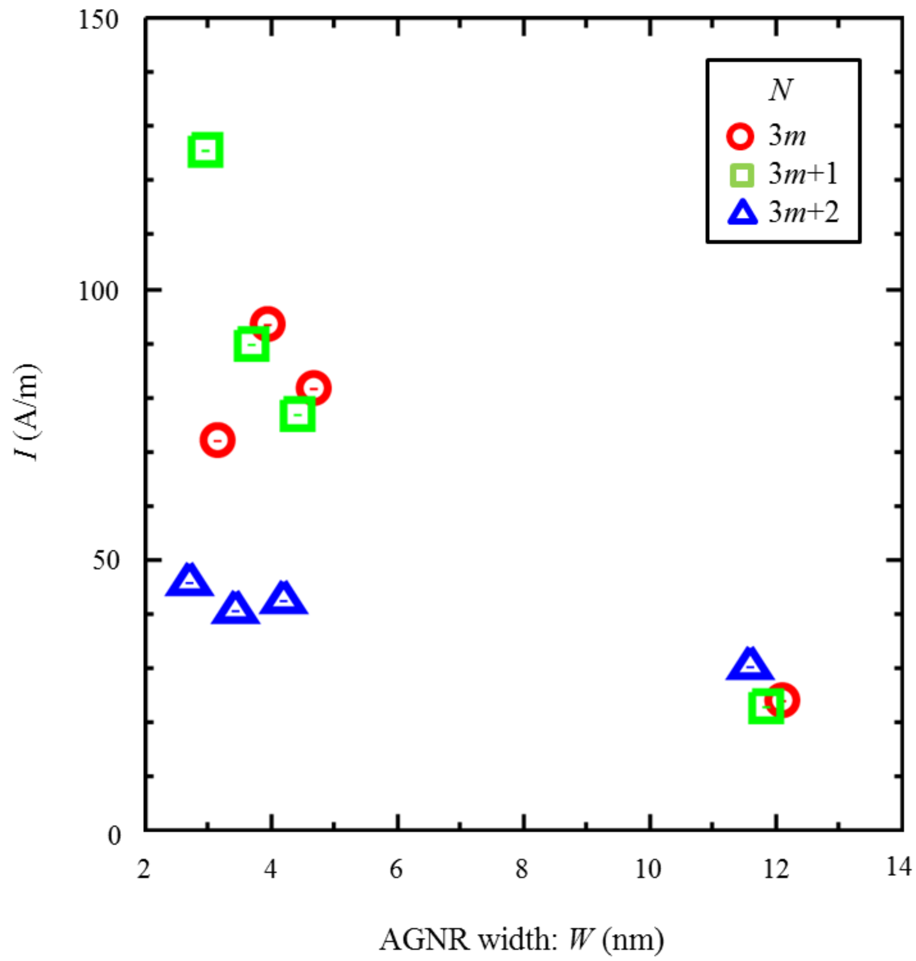

Fig. 3.11: Current density I as a function of the AGNR width W for the models of the AGNR bridged between two Au electrodes at a bias voltage V_b = 0.1 V.

3.4.2. Origin of N-family dependence

To unravel the N-family dependence observed in current densities, we analyze transmission spectra $T(k_y, E)$ as functions of both wave number along the ribbon k_y and energy E of AGNR with $W \sim 4.5$ nm (Fig. 3.12). The spin-dependent transmission coefficient $T_\sigma(E)$ is defined as

$$T_\sigma(E) = \frac{1}{N_{k_y}} \sum_{k_y} T_\sigma\left(k_y, E\right), \tag{3.7}$$

where σ is the index of the spin (up or down) and N_{ky} (= 151) is the number of k-points along the y direction. Using the $T_\sigma(E)$, the current density I is evaluated by

$$I = \frac{1}{L_y} \sum_\sigma \frac{e}{h} \int_{-\infty}^{\infty} T_\sigma(E)[f(E - \mu_\mathrm{L}) - f(E - \mu_\mathrm{R})] dE, \tag{3.8}$$

where L_y is the length of the unit cell of the model along the y direction. The $T_\sigma(k_y, E)$ around the energy integration range from 0 to 0.1 eV smeared with the electronic temperature in the Fermi-Dirac function gives the current density. We found the large $T_\sigma(k_y, E)$ within the integration range for AGNRs with $N = 39$ and 37, while the transmission is small within the range for the AGNR with $N = 35$. Indeed, the AGNRs with $N = 39$ and 37 exhibit high transport properties while the AGNR with $N = 35$ is less conductive than the other two ribbons. Further analyses on the transmission spectra for the AGNRs with the other ribbon width corroborate the fact that the N-family dependence in the current densities originates from the transmission spectra in the integral region determined by the ribbon width or the number of dimer rows N. The transmission spectra reflect the characteristic feature of the band structures of the isolated AGNRs as shown in right panels of Fig. 3.12. The energies are shifted upward by about 0.3 eV simulating the p-doping from the Au electrodes for the comparison with the transmission spectra. The transmission occurs at the particular k_y and E at which electronic energy band emerges in graphene because of the weak interaction between Au and graphene.

In addition to the band structure, the symmetry of π state of graphene also plays an important role in determining the transmission spectra. The isolated AGNR with $N = 39$ is a semiconductor with a band gap of about 0.2 eV as shown in Fig. 3.12(a). The highest occupied molecular orbital (HOMO) and the second highest occupied molecular orbital (HOMO-1) of the isolated AGNR at the Γ-point are located at the energies of 0.2 eV and 0 eV, respectively. By comparing the transmission spectra and the band structure, we

find that the HOMO give the small $T_\sigma(\Gamma, E)$ while the HOMO-1 leads to the large $T_\sigma(\Gamma, E)$. To clarity the difference of the two states, we show the wave functions of them in Fig. 3.13(a). The HOMO shows the anti-symmetric nature of their wave function with respect to the *xz* plane, while the HOMO-1 shows symmetric nature. On the other hand, surface electron states around the Fermi level of Au comprise *s* orbital of Au atoms possessing the symmetric nature with respect to the surfaces. Only the symmetric π state of the HOMO-1 hybridizes with the *s* state of the Au surface as shown in Fig. 3.13(b). We find that the π states with symmetric nature mainly contribute to the transmittance through the contact between Au and graphene. The symmetric π states of AGNRs appear alternately, resulting in the discrete and sparse transmission peaks. To examine the wave functions in the hybrid structures, we consider the clustered model of the AGNR bridged between two Au electrodes in Fig. 3.13(b). The model has finite size of the Au electrodes in the *x*-direction. The conventional band calculation is performed under the three-dimensional periodic boundary conditions with enough vacuum spacing. Although the electronic structure of the interface is different from that in the NEGF calculation due to the effect of the metal edges, the band structure and the wave function in the model are useful to understand the results of the transmission.

We also find that the values of $T_\sigma(k_y, E)$ are fluctuated along the k_y even in the same π state in Fig. 3.12. For examples, the $T_\sigma(k_y, E)$ derived from the HOMO of the AGNR with $N = 39$ [Fig. 3.12(a)] shows a value of about 0.3 at the α-point ($k_y = 0.05$), while it is almost zero at the Γ-point. The fluctuation of $T_\sigma(k_y, E)$ is ascribed to symmetry change of the π state along the k_y. The HOMO of the isolated AGNR at the α-point is still anti-symmetric [Fig. 3.13(a)], while the symmetric and well-hybridized wave function appears in the model with Au electrodes [Fig. 3.13(b)]. The symmetric *s* state of the Au surface can hybridizes with the symmetric component of the π state at any k_y. Although the HOMO-1 of the isolate AGNR at the α-point is not symmetric, the symmetric character is found in the model with Au electrodes as well as the HOMO. Thus the symmetric π state at the Γ-point may become immiscible with the Au electrodes depending on the k_y.

Another fact obtained in Figs. 3.12 and 3.13 is that the band crossing may leads to the suppression of the $T_\sigma(k_y, E)$. The band repulsion is occurred at the crossing point of the bands of graphene and Au according to

the symmetry requirement. For examples, the repulsive band crossing shown as the blue circle in Fig. 3.13(b) results in the small transmission at the (k_y, E) indicated by the blue arrow in Fig. 3.12(a).

The same analysis is applicable to the other AGNR with different ribbon widths or the N family: the state possessing the symmetric nature with respect to the surfaces leads to the large transmission irrespective to the ribbon width or the number of dimer rows N. Figure 3.14 shows the transmission spectra of the hybrid structures and the band structure of the isolated AGNRs with N = 99, 97, and 95, where the ribbon width W are about 12 nm. Even in the ribbon with the width of 12 nm, the band structures and the symmetry of the π state of graphene determine the transport properties.

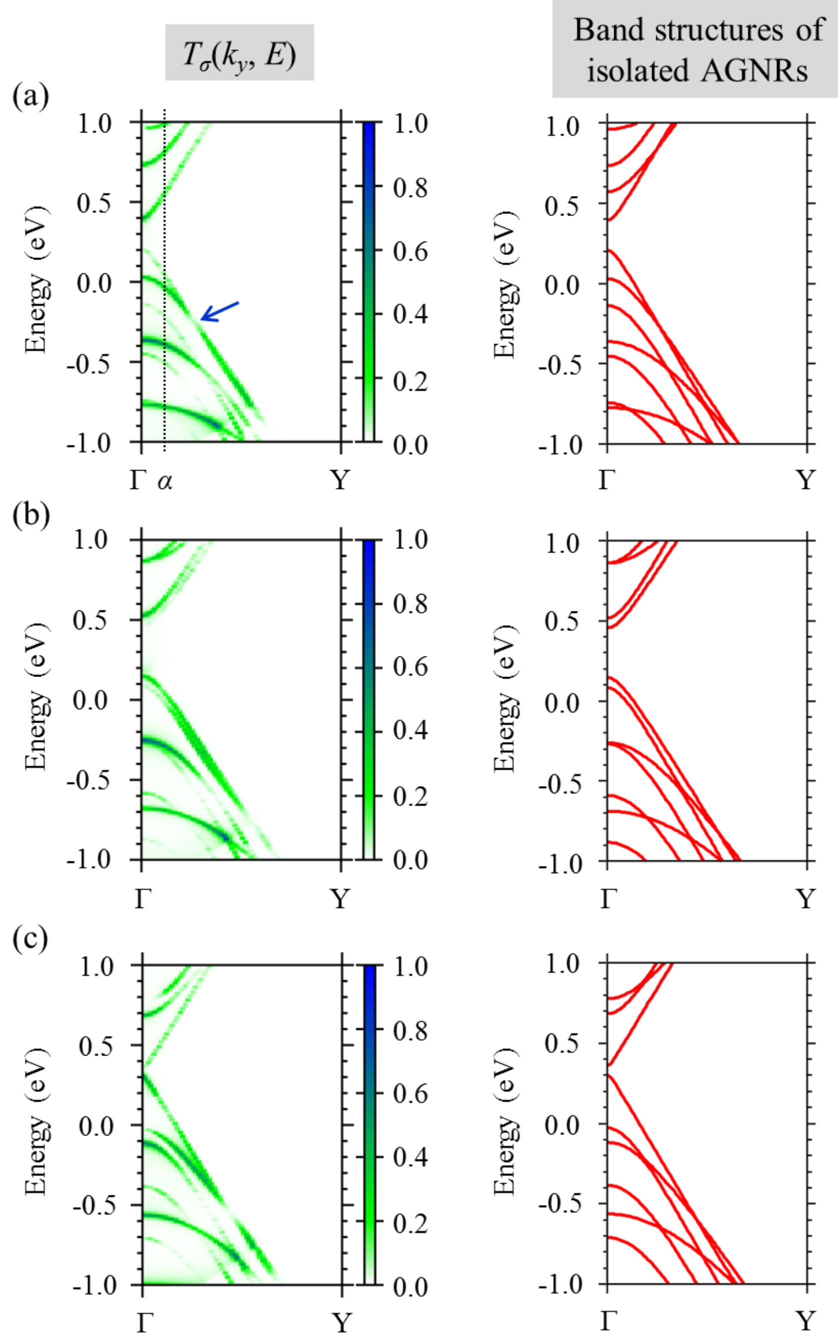

Fig. 3.12: Transmission spectra $T_\sigma(k_y, E)$ and band structures of the isolated AGNRs for the models with N = (a) 39, (b) 37, and (c) 35, which belong to the $3m$, $3m$+1, and $3m$+2 families, respectively. The energies in the band structures of the isolated AGNRs are shifted upward by about 0.3 eV for comparison with $T_\sigma(k_y, E)$. Only the up-spin of the transmission is shown due to no spin-polarization. The chemical potentials of the left-side lead μ_L are set to 0 eV in $T_\sigma(k_y, E)$. The right color bar shows the value of $T_\sigma(k_y, E)$. The α-point is located at $k_y = 0.05$ (*cf.* Γ: $k_y = 0.0$, Y: $k_y = 0.5$).

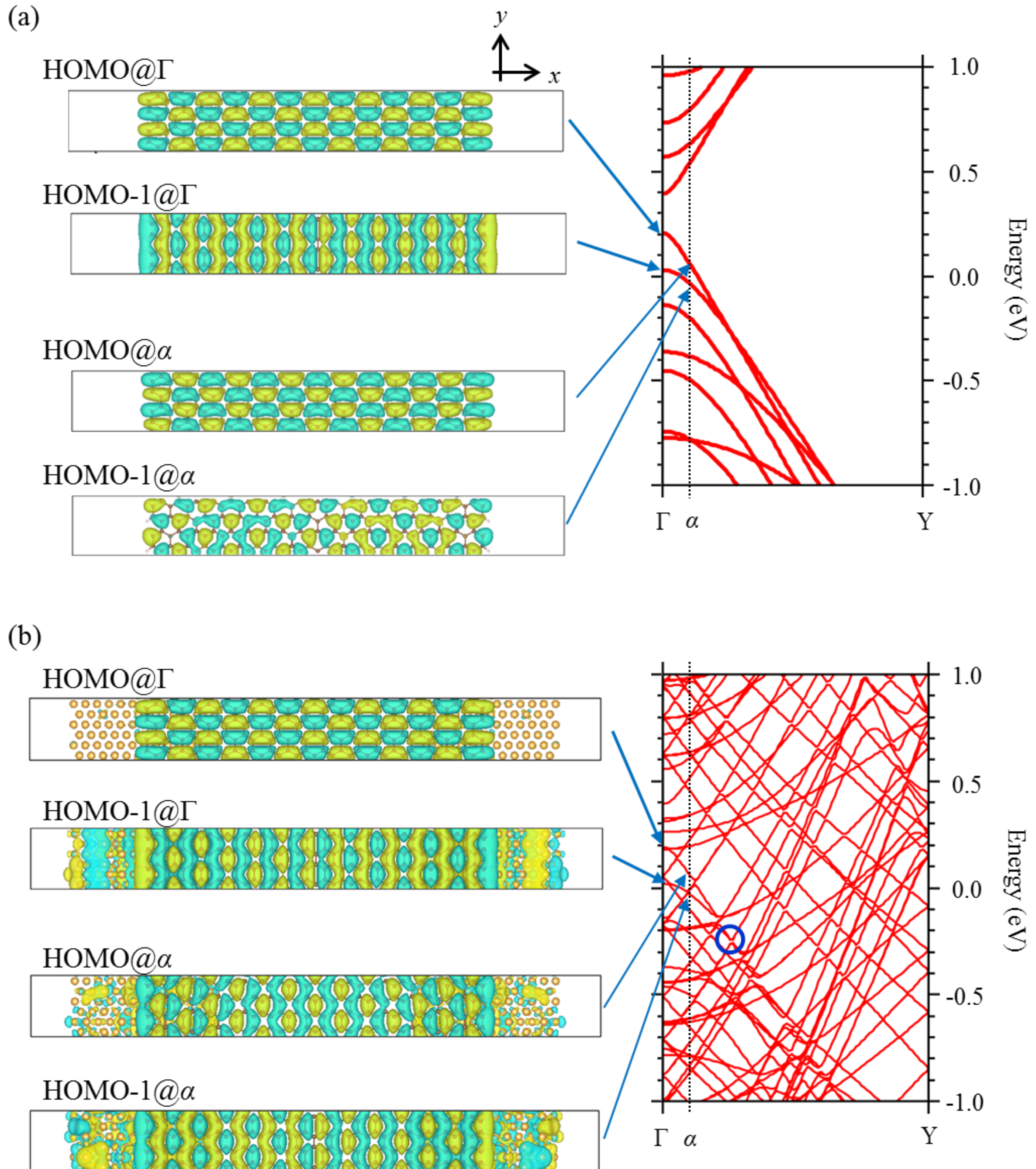

Fig. 3.13: Wave functions and band structures for (a) the isolated AGNR with $N = 39$ and (b) the clustered model of AGNR with $N = 39$ bridged between two Au electrodes. The solid rectangles in the left panel represent the unit cell. The α-point is located at $k_y = 0.05$ (*cf.* Γ: $k_y = 0.0$, Y: $k_y = 0.5$). The real-parts of the wave functions are shown for the α-point. The band structure in (a) is same as in Fig. 3.12(b).

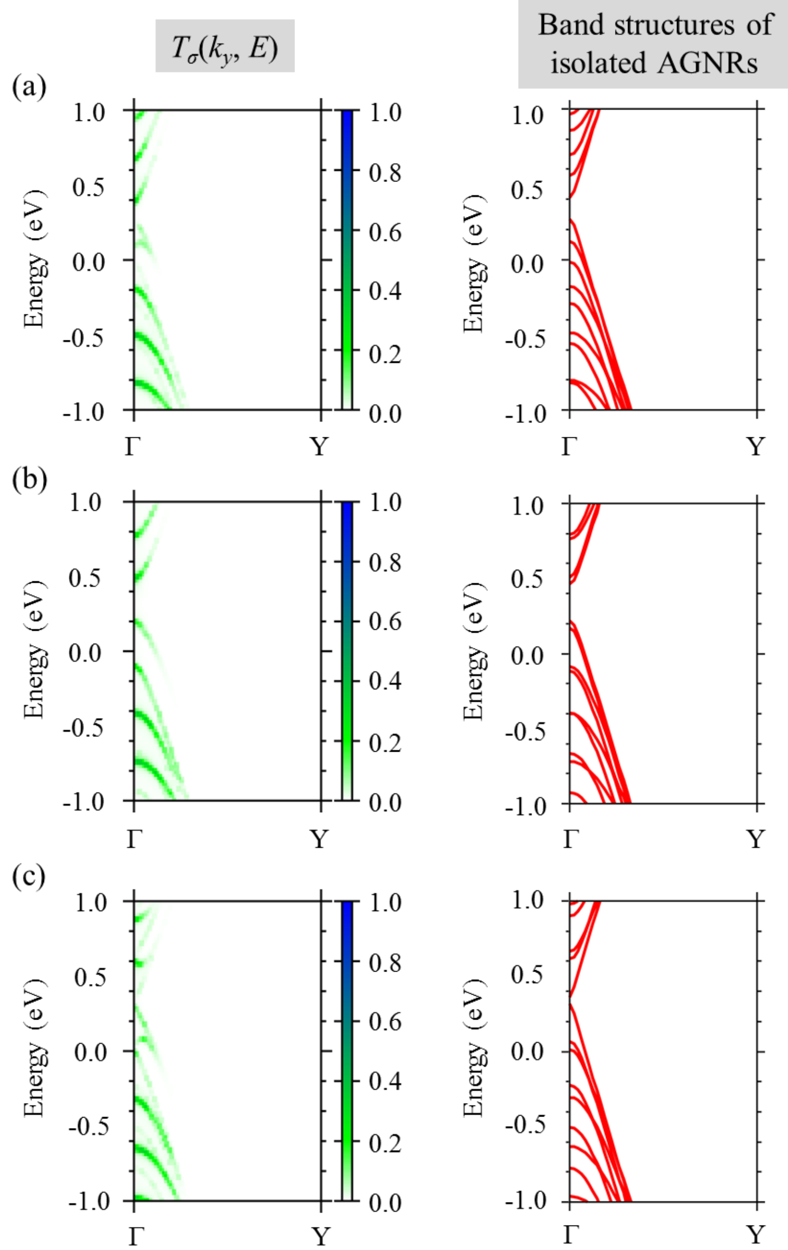

Fig. 3.14: Transmission spectra $T_\sigma(k_y, E)$ and band structures of the isolated AGNRs for the models with N = (a) 99, (b) 97, and (c) 95, which belong to the $3m$, $3m$+1, and $3m$+2 families, respectively. The energies in the band structures of the isolated AGNRs are shifted upward by about 0.17 eV for comparison with $T_\sigma(k_y, E)$. Only the up-spin of the transmission is shown due to no spin-polarization. The chemical potentials of the left-side lead μ_L are set to 0 eV in $T_\sigma(k_y, E)$. The right color bar shows the value of $T_\sigma(k_y, E)$.

3.4.3. Origin of W dependence

It is worth investigating how the current depends on the ribbon width in each N family. In all N family cases, the current density asymptotically decreases as the ribbon widens. In the case of the AGNR with the width of $N = 3m$, the current density oscillates within the family. Figure 3.15 shows the transmission spectra of the AGNR with $N = 27$ ($W = 3.15$ nm), $N = 39$ ($W = 4.68$ nm), and $N = 99$ ($W = 12.10$ nm). The large $T_{\sigma}(k_{y}, E)$ originating from the HOMO-1 state is not located in the bias range for $N = 27$, while the $T_{\sigma}(k_{y}, E)$ is observed in the range for $N = 39$, resulting in a higher current density in $N = 39$ than in $N = 27$. The $T_{\sigma}(k_{y}, E)$ in $N = 99$ is the smallest among $N = 27$, 39, and 99 within the integration range from 0 to 0.1 eV, although the band structures correspond with the transmission spectra. This smallest $T_{\sigma}(k_{y}, E)$ leads to the lowest current density in $N = 99$ among the $N = 3m$ family. As described above, the variation of current density was observed even in the 12 nm ribbons. The energy interval of the π states associating with the transmittance is 0.15 eV for the model with $N = 99$ as shown in Fig. 3.15(c). The larger energy interval than the integration range of 0.1 eV is likely to cause the variation of current density. Wider AGNRs will suppress the variation because the energy interval inversely decreases with increasing the ribbon width.

The suppression of the transmission spectra in the wider ribbon is ascribed to the decrease of the wave function distribution of the state hybridizing with electrodes in the bridge region. Figure 3.16 shows the wave functions of the HOMO-1 states for $N = 99$ and 39 in the clustered model which is described in previous section. The distribution seems to be uniform in the ribbon with both N at the Γ-point as shown in Figs. 3.16(a) and 3.16(c). At $k_{y} = 0.07$, however, the distribution decrease at the middle of the ribbon compared with the contact region for $N = 99$, while the uniform distribution throughout the ribbon is still found for $N = 39$. When the k_{y} is changed, the π states of the ribbon in the contact region can modulate themselves in keeping the same symmetry with the electrodes by using the electronic state of the electrodes. On the other hand, the π states of the ribbon in the bridge region cannot use the states of the electrodes and they create the new states by using only the ribbon states, resulting in the less hybridization if the π states of the ribbon have different symmetries from the electrodes. As increasing the bridge region, the distribution of the wave functions becomes non-uniform along the ribbon [Fig. 3.16(b)].

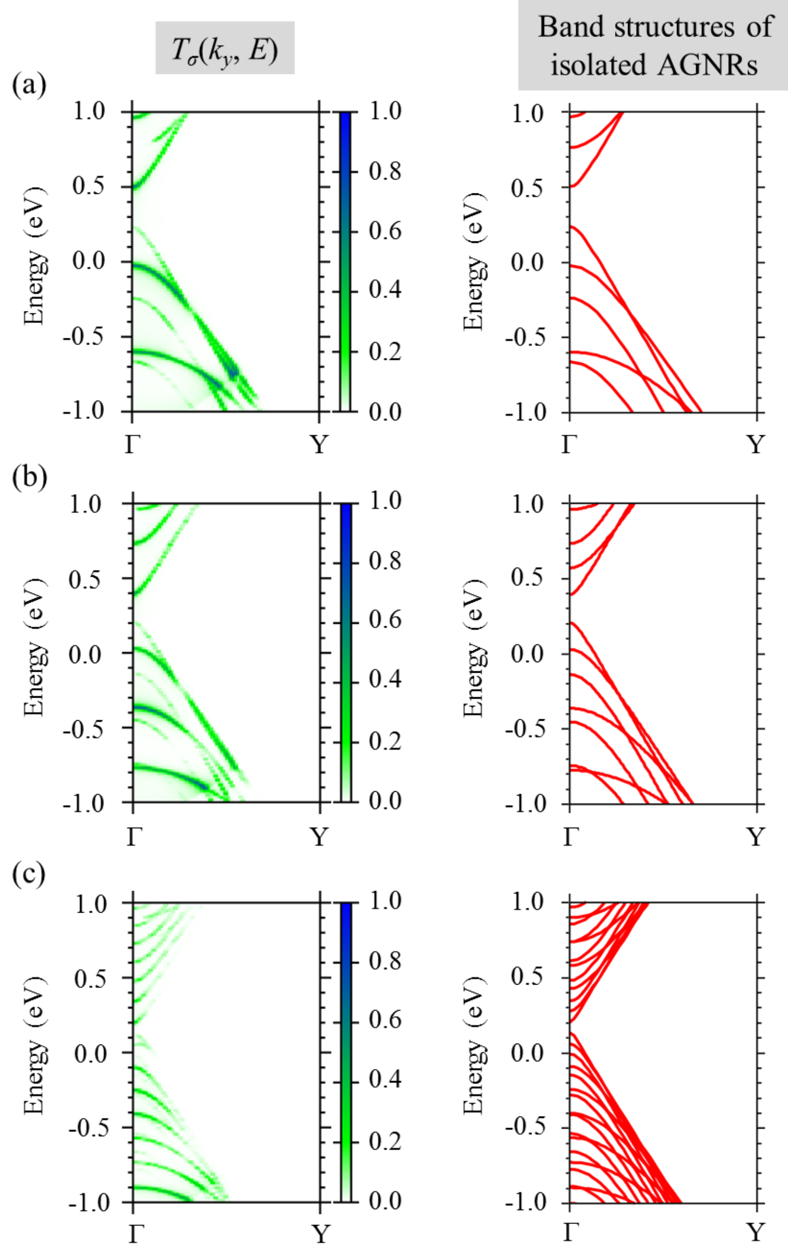

Fig. 3.15: Transmission spectra $T_\sigma(k_y, E)$ and band structures of the isolated AGNRs for the models with N = (a) 27, (b) 39, and (c) 99, which belong to the 3*m* family with W = 3.15, 4.68, and 12.10 nm, respectively. The energies in the band structures of the isolated AGNRs are shifted upward by arbitrary energies for comparison with $T_\sigma(k_y, E)$.

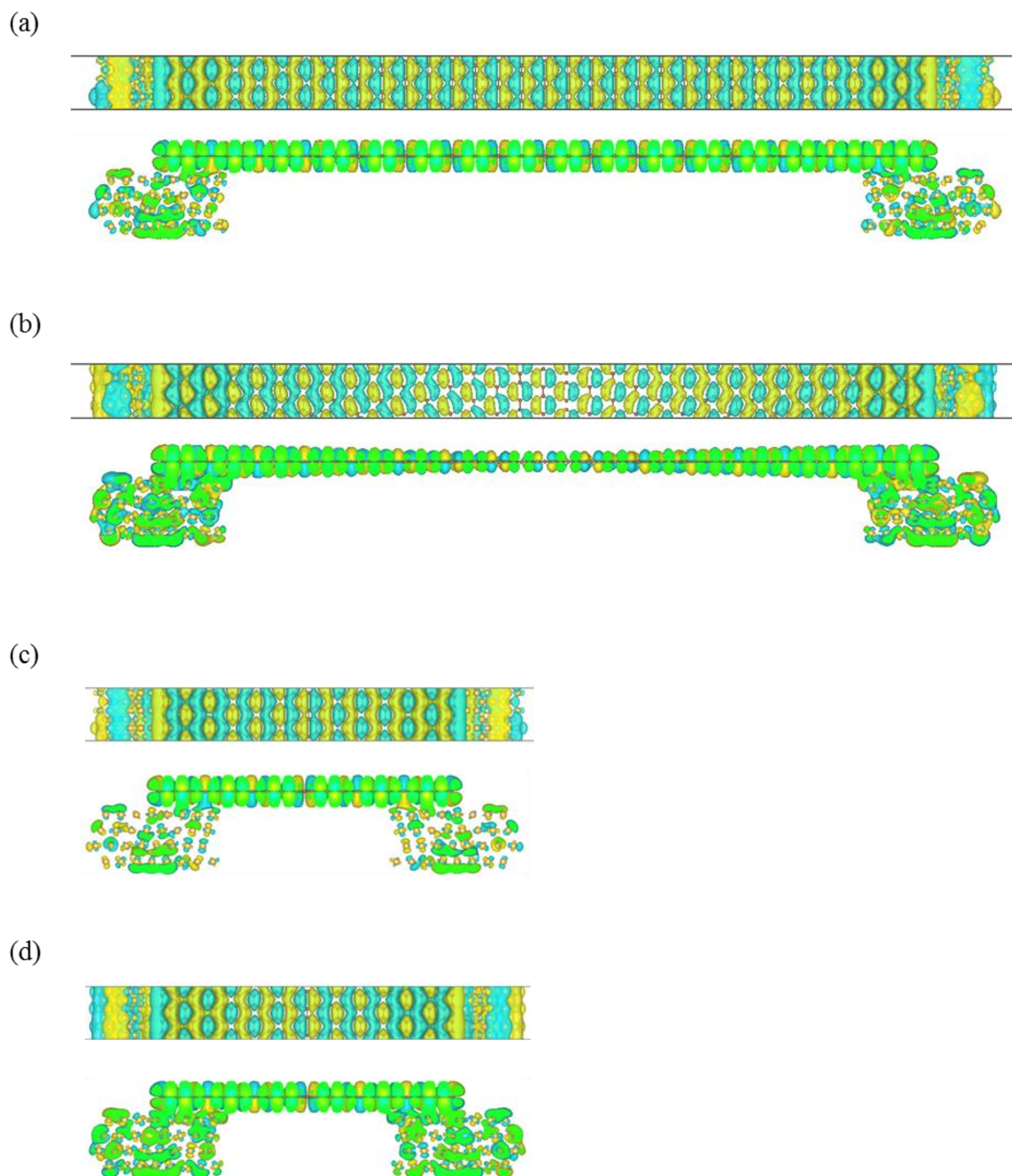

Fig. 3.16: Wave functions of the HOMO-1 state for the clustered model with N = (a)(b) 99 and (c)(d) 39. The k_y is 0.0 (Γ) for (a) and (c), and 0.07 for (b) and (d).

3.4.4. Hybrid structure of graphene/Ti electrodes

Figure 3.17 shows current densities for the Ti electrodes. For comparison, those for the Au electrodes are also shown. We found that the current densities for the Ti electrodes are about 10 times as large as those for the Au electrodes in all W (i.e. N) studied here.

As shown in Fig. 3.18, the transmission occurs at a wide range of the energy eigenvalues E and the wave number along ribbon k_y around those of the AGNR (Fig. 3.14) arising from the strong π-d coupling that substantially enhances the electron transfer through the Ti-graphene contact. For the Au electrode, on the other hands, the transmission peaks reflect the band structures and they alternately arise from the symmetry of the π state of the AGNRs as discussed in Sec. 3.4.2. The broad transmission spectra are observed at each k_y for the Ti electrode, while the transmission peaks are discrete and smaller for the Au electrode, as shown in Fig. 3.19. We find that the contact resistance between graphene and metal electrodes decisively depends on the amount of the hybridization between them, which is determined by the energy location of metal d states with respect to the Fermi level.

Figure 3.20 shows the difference of the projected density of states (PDOS) of graphene between near the contact area and the middle of the ribbon. The strongly hybridized electronic states are found in atoms labelled as A and B, which are in the ribbon near the contact area. However, the character of the isolated AGNR is recovered in an atom labelled as D, which is at the middle of the ribbon. The energy shift of the Dirac point is about -0.2 eV, indicating n-doping from the Ti electrodes. The PDOS of an atom labelled as C shows similar character to that of the atom D. For the narrower ribbons, the transmission spectra will be completely out of the character of the band structure of the isolated AGNRs by reflecting the completely mixed electronic states. In this wider ribbon (N = 95), the electronic state of the isolate AGNRs is observed in the middle of the ribbon, resulting in the transmission spectra at E and k_y around the band structure of the isolated the AGNR.

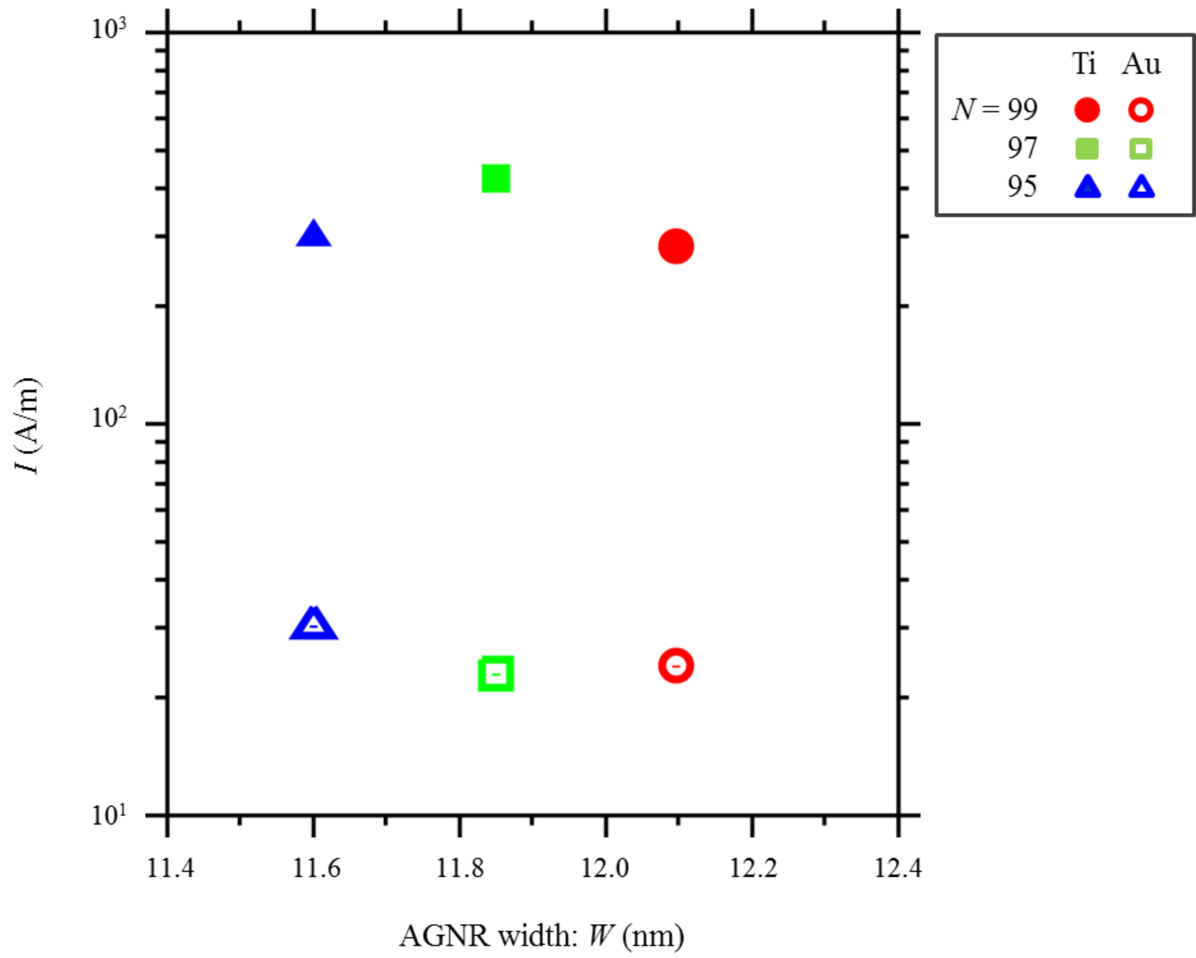

Fig. 3.17: Current density I in a log scale as a function of the AGNR width W for the models of the AGNR bridged between Ti and Au electrodes at a bias voltage $V_b = 0.1$ V.

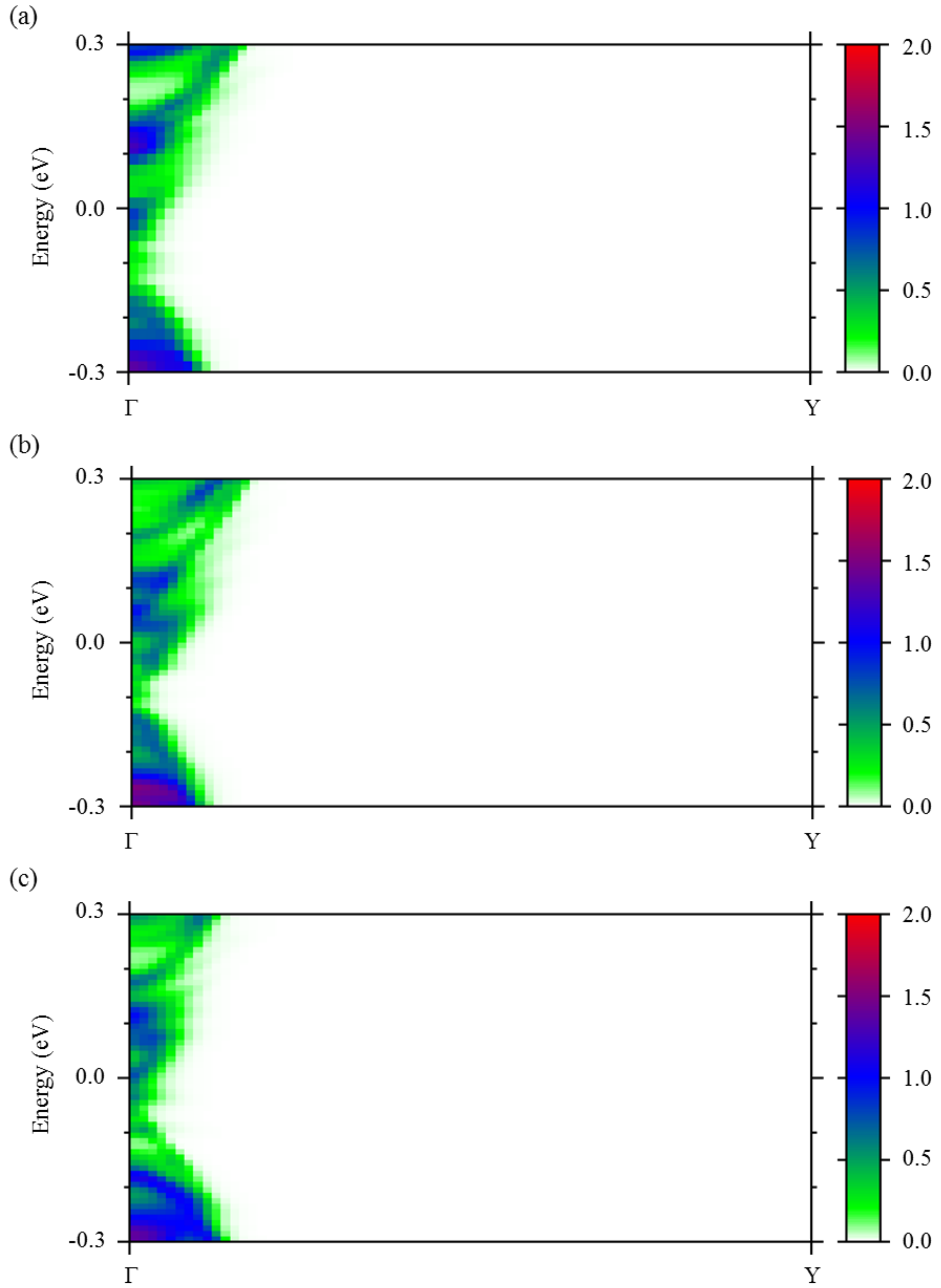

Fig. 3.18: Transmission spectra $T_\sigma(k_y, E)$ for the models with N = (a) 99, (b) 97, and (c) 95 for Ti electrodes.

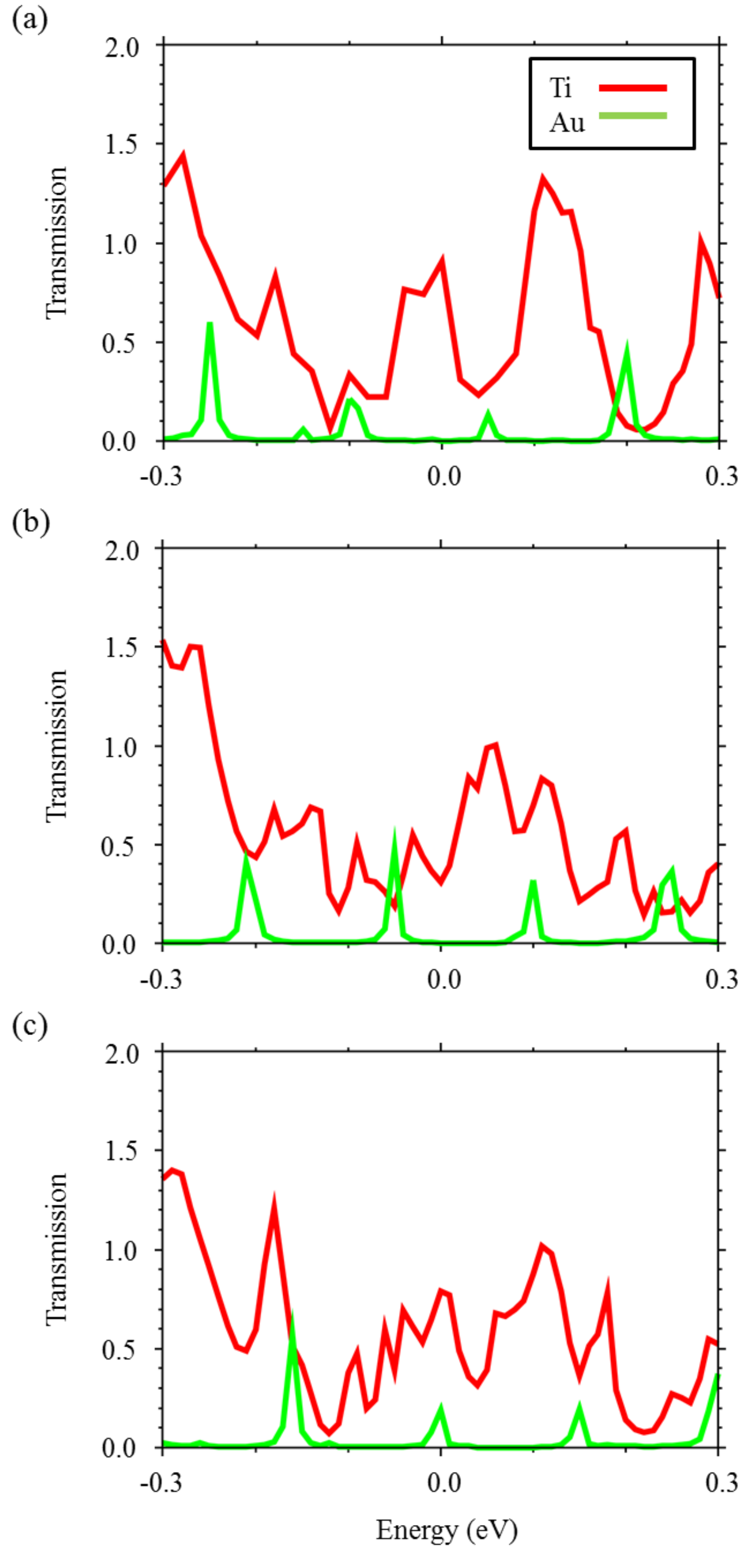

Fig. 3.19: Transmission spectra $T_{\sigma}(\Gamma, E)$ for the models with N = (a) 99, (b) 97, and (c) 95 for Ti and Au electrodes.

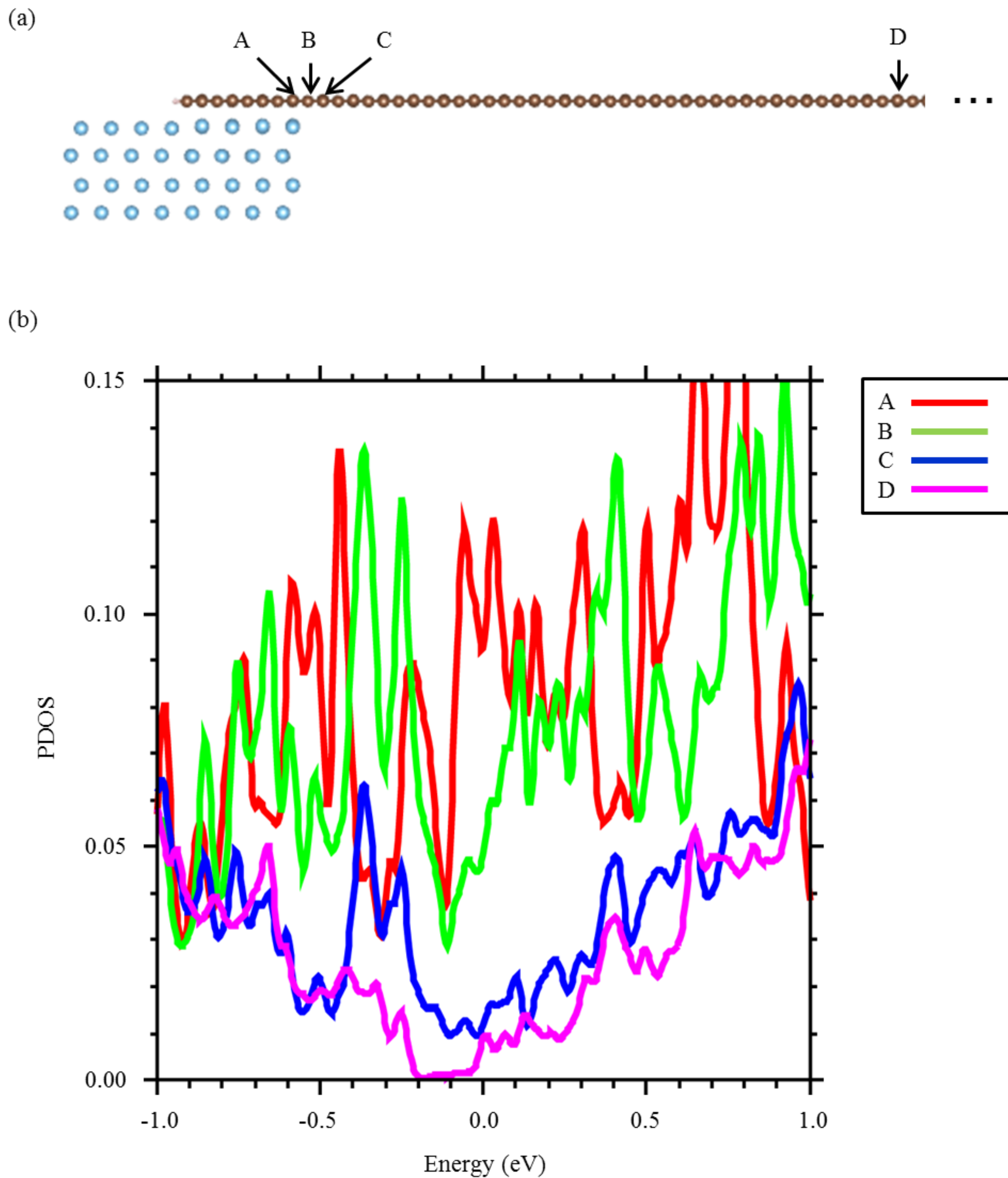

Fig. 3.20: (a) Left-hand half of the clustered model of the hybrid structure of graphene and Ti electrodes with $N = 95$. The carbon atom labelled as D is just the middle of the ribbon. (b) Projected density of states (PDOS) of the carbon atoms labelled as A, B, C, and D in (a).

3.4.5. Discussions

In this thesis, we assume that GNRs are adsorbed on clean crystalline metal surfaces. The metal electrodes deposited by the electron-beam lithography are considered to be poly crystals. The high substrate temperature gives large grains of the metal crystals. The annealing may also develop the grain size. The local geometries in experimental seem to be similar to our models. However, a lot of impurities such as water, oxygen, and nitrogen are generally present at the interface [126]. The organic materials from the resist residuals may be one of the impurities [77]. Such surface contaminations modulate work functions of the clean metal surface, resulting in the variation of the ΔE_D in the weak interaction system such as the graphene/Au hybrid structure. The equilibrium spacing d will also be enlarged by the contaminations, also resulting in the variation of the ΔE_D as discussed in Sec. 3.3.3. The current densities may become quite different, when the shift is larger than the integration range of 0.1 V.

The current densities in the graphene-Ti contacts with many adsorbates will be drastically decreased compared with our results, because the chemical interaction between graphene and metal could be weakened as increasing the concentration of adsorbates on the metal surface [77]. Due to the absence of the strong π-d coupling, the transmission will occur at the particular k_y and E at which the electronic energy band emerges in the isolated AGNRs as in the case of the graphene/Au hybrid structures.

Finally, we discuss the contact area effect on the transport properties. As reported in the previous works [74, 106], the current density is expected to depend on the contact area: In the case of Cu electrode [111], transmission spectra shift downward in energy with respect to the Fermi level due to the enhancement of electron transfer from the metal surface to the graphene with increasing the contact area. By the analogy with the Cu electrode, thus, the electron transfer from the graphene to the metal surface is expected to be increased with increasing the contact area. Furthermore, the transmission spectra shift upward with respect to the Fermi level. In the case of Ni electrode [111], the transmission increases with increasing the contact area due to the enhancement of the interfacial hybridization. By the analogy with the Ni electrode, the Ti electrode will exhibit a contact-dependent conductance which monotonically increases with increasing the contact area.

3.5. Conclusions

We have studied the electronic transport properties through AGNRs with a width of up to 12 nm bridged between two Au and Ti electrodes using first-principles calculations. For the Au electrodes, we have found that the current densities sensitively depend on the ribbon width, even though the width reaches 12 nm. The symmetry of π state of the graphene ribbons as well as the band structure is important for determining the transport properties. These results suggest that the width of graphene material should be precisely controlled for designing the graphene-based FET devices with Au electrodes. For the Ti electrodes, on the other hand, the current densities are determined by only the modified electronic band structure of the graphene. Thus the contact resistance between graphene and metal electrodes decisively depends on the metal species. These results should be applicable to give a theoretical insight for transport properties of physisorbed and chemisorbed graphene on other metals.

Chapter 4. Graphene/insulator hybrid structures

In this chapter, we investigate the electronic transport properties of the hybrid structures of graphene/insulators. We firstly present problems arising from the fragility of electronic properties of graphene on insulating substrates, and introduce the previous studies on the graphene/insulator interfaces in Sec. 4.1. We then demonstrate the computational details and employed models in Sec. 4.2 and 4.3, respectively. In Sec. 4.4, we show results and develop discussions for the electronic transport properties of the hybrid structures of graphene/insulators. Finally, we present conclusion of this chapter in Sec. 4.5.

4.1. Introduction

Graphene is normally supported on insulating substrates such as SiO_2 in electronic devices in order to ensure process robustness and electrical reliability. The carrier mobility of suspended graphene can be up to 200,000 $cm^2V^{-1}s^{-1}$ [127, 128], while that of graphene on a SiO_2 substrate is limited to 10,000 $cm^2V^{-1}s^{-1}$ [1]. The on/off current ratio of freestanding GNRs is also degraded on SiO_2. For example, freestanding GNRs exhibit a ratio of 10^4 [129], while GNRs on SiO_2 have a ratio of 10^1 at a ribbon width W = 20 nm and a source-drain bias V_{ds} = 0.5 V [130].

The surface treatment of SiO_2 also changes the electronic transport properties of graphene. The primary structures of silica surfaces are known to be silanol groups (Si–OH) and siloxane groups (Si–O–Si) [131]. The treatment of the SiO_2 surface with O_2 plasma after dipping in HF results in the silanol (OH-terminated) surface. The siloxane (O-terminated) surface is prepared by annealing the silanol surface in O_2 gas to desorb H_2O molecules. Silanol groups on the SiO_2 surface degrade the mobility and shift the Dirac point of graphene, while graphene on the siloxane SiO_2 surface shows the high mobility without the Dirac point shift [132].

From a theoretical perspective, several studies on the geometrical and electronic properties of graphene on SiO_2 have been reported using first-principles methods. They showed that graphene is strongly bound to O-terminated SiO_2 substrates with unsaturated O dangling bonds via the formation of covalent C–O bonds

[36, 133, 134]. However, on OH- and O-terminated SiO_2 surfaces without dangling bonds, graphene is weakly bound to the surface [135]. On both OH- and O-terminated SiO_2 surfaces, the energy band structure of freestanding graphene is almost preserved, but a small energy gap is formed at the Dirac point. Although no charge transfer between the graphene and either SiO_2 surface is observed, inhomogeneous valence charge redistribution occurs in the interfacial region for the OH-terminated surface [136]. The charge redistribution indicates that the silanol group could be one of the main scattering centers on the SiO_2 substrate and the carrier mobility in graphene can be suppressed by the presence of the OH groups on the SiO_2 surface.

4.2. Computational details

The computational details are almost the same as the last chapter. For geometrical optimizations, we use the PAOs specified by C-*s*2*p*2*d*1, H-*s*2*p*1, Si-*s*2*p*2*d*1, and O-*s*2*p*2*d*1. Real-space grid techniques are used with a grid cell length of l_g = 0.13 Bohr in numerical integrations, and the Poisson equation was solved using FFT. We use the O(*N*) scheme based on a Krylov subspace method implemented in OpenMX [137]. The radius of cluster truncation and the dimension of the Krylov subspace are set at 1.1 nm and 1500, respectively. Geometries are optimized under a three-dimensional periodic boundary condition, and the convergence criterion for forces on atoms is 0.1 eV/nm.

For transport calculations, we employ the NEGF method implemented in OpenMX. The PAO set is C-*s*1*p*2, H-*s*1, Si-*s*1*p*1, and O-*s*1*p*1. To examine the accuracy of the small basis set, we made a small unit cell model with graphene on SiO_2/Si [Fig. 4.1(b)]. The graphene is compressed by 11% along the *x*-direction and expanded by 4% along the *y*-direction to match with the lateral unit cell of SiO_2/Si. The energy band structure of the compressed graphene is shown in Fig. 4.1(c). The Dirac point in the compressed graphene is shifted to the Γ-Y direction from the Γ-point, where it is folded under the equilibrium lattice constant. Figures 4.1(d) and 4.1(e) show the energy band structures of graphene on SiO_2/Si obtained using the large and small orbital sets, respectively. The large basis set provides quantitatively the same results each other in the geometry and electronic properties through our benchmark calculations. The Dirac point of graphene for the small basis set appears just 0.09 eV above that of the large basis set. The difference of Fermi velocity of the bands around the Dirac point is within 6% between the large and small basis sets. A larger l_g = 0.30 Bohr is used in the real-space grid techniques. The accuracy of the large grid cell length (l_g = 0.30 Bohr) is examined using the short-channel model with L = 0.86 nm as shown in Fig. 4.2(a). The model is composed of two units of the AGNR channel with N = 7 and the strained AGNR leads with N = 8. We calculated the current densities for the model at bias voltages of 0.5 V and 1.0 V using the NEGF method. The errors in the current densities are shown in Fig. 4.2(b). The obtained current density for l_g = 0.30 Bohr is below 3% smaller than that for l_g = 0.13 Bohr, which is the value employed in the geometric optimization. We concluded that the small set of PAOs and the large grid cell length l_g = 0.30 Bohr are adequate to discuss the

transport properties of AGNRs on SiO_2/Si. These treatments significantly contribute to reduce the computational cost.

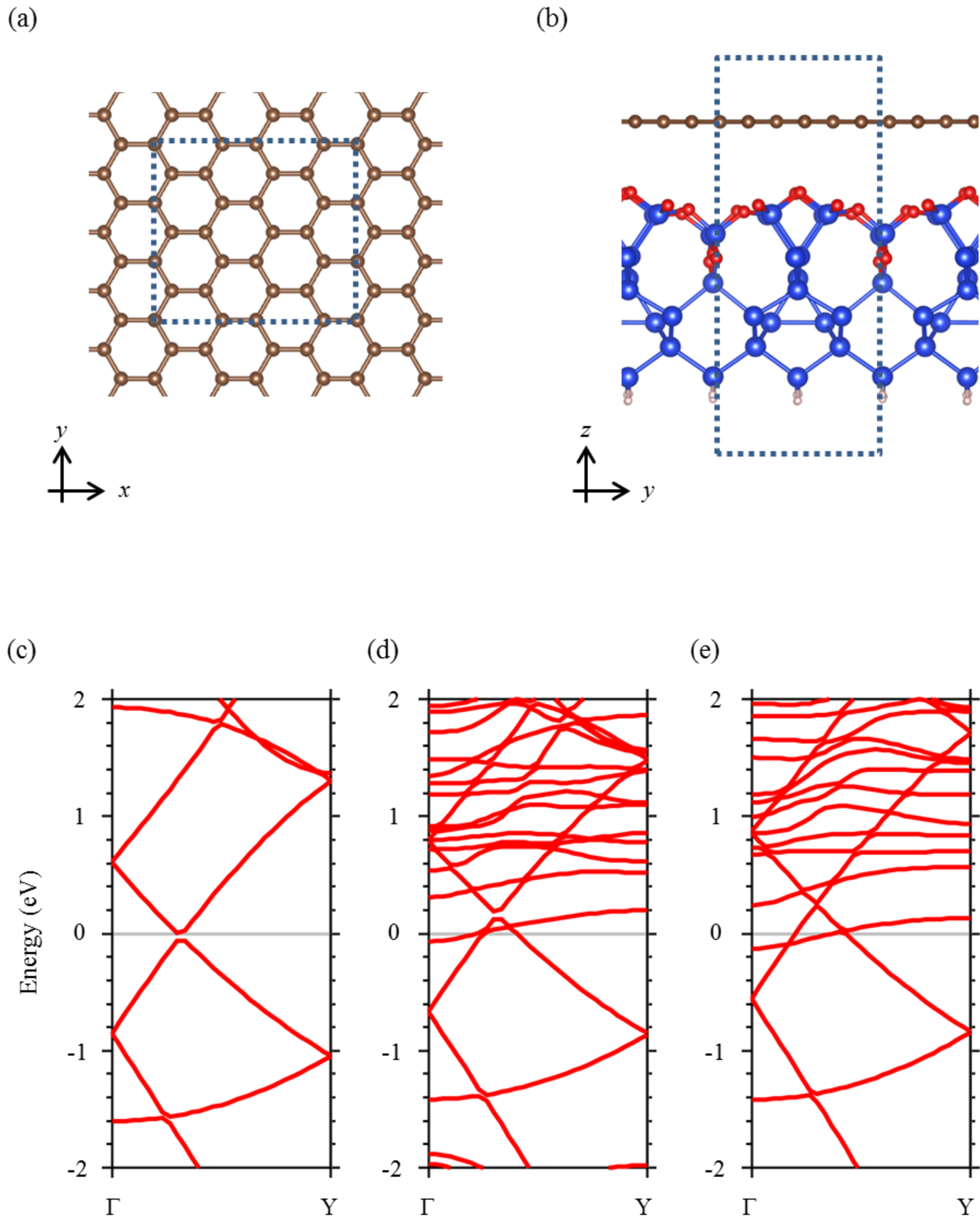

Fig. 4.1: A small unit cell model with (a) graphene and (b) graphene on SiO_2/Si in the equilibrium SiO_2/Si cell. The dotted rectangle indicates the unit cell. The lattice of graphene is compressed by 11% along the *x*-direction and expanded by 4% along the *y*-direction to match the lateral unit cell of SiO_2/Si. Energy band structures of (c) the compressed graphene using large basis sets, and graphene on SiO_2/Si using (d) large and (e) small basis sets. The Fermi level is set at zero energy.

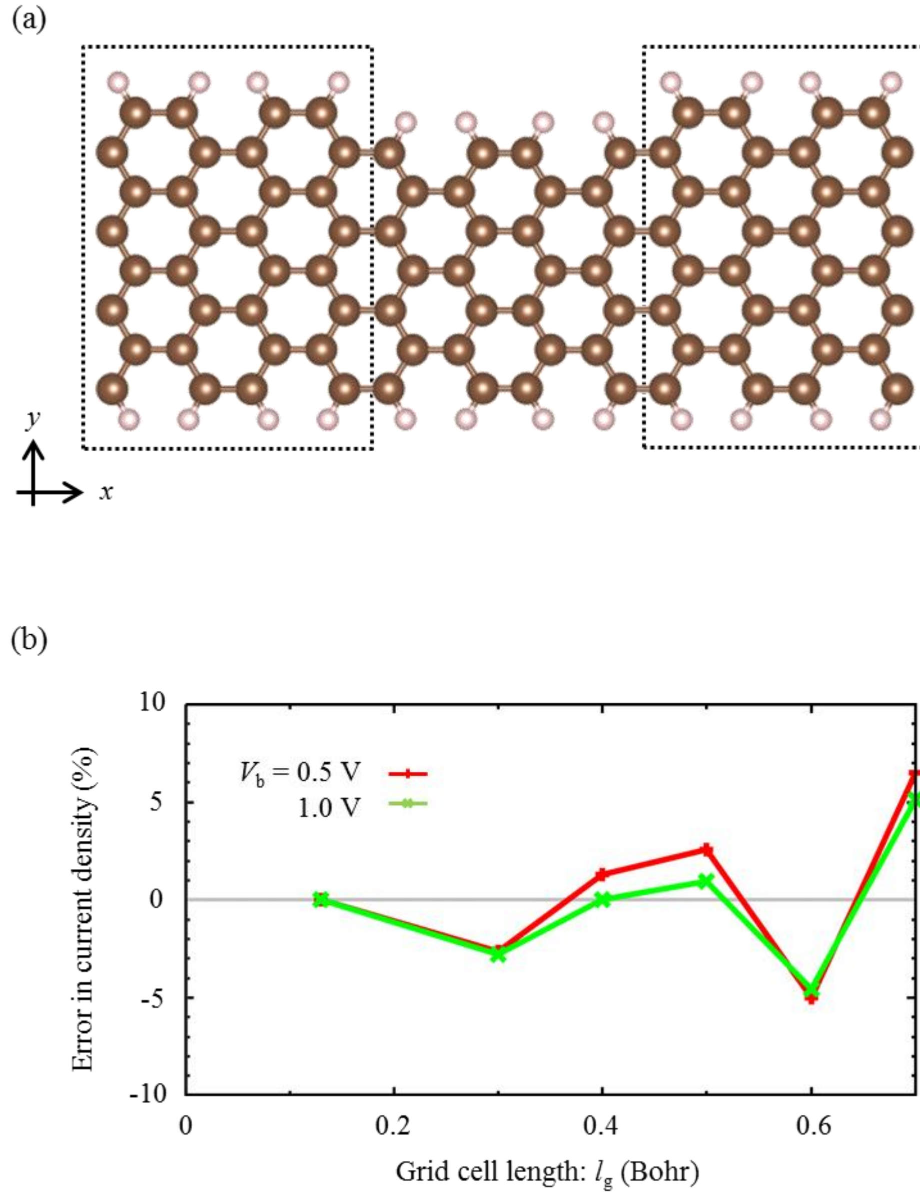

Fig. 4.2: (a) A short-channel model of AGNR with $L = 0.86$ nm to examine the relationship between the grid cell length l_g and the current density. The model is composed of two units of the AGNR channel with $N = 7$ and the strained AGNR leads with $N = 8$. (b) Errors in the current densities as a function of the grid cell length under bias voltages of $V_b = 0.5$ V and 1.0 V.

4.3. Models

In this thesis, we study the electronic transport properties of AGNRs on SiO_2/Si. The AGNRs with the number of C_2 dimer rows $N = 7$ are chosen. We examine the SiO_2/Si surfaces with OH and O terminations. We also investigate the transport properties of AGNRs on SiO_2/Si with two channel lengths of $L = 9.91$ and 15.1 nm.

4.3.1. AGNRs

Figure 4.3 shows freestanding AGNRs used for transport calculations. The channel of an AGNR with $N = 7$ is sandwiched between semi-infinite leads. The calculated energy band gap of the AGNRs with $N = 7$ is 1.6 eV, which is consistent with previous works [45, 138]. For simplicity, the leads were made of AGNRs with $N = 8$ whose lattice parameter is uniaxially elongated by 1.86 % along the ribbon in order to possess metallic electronic structure [138, 139]. All edge carbon atoms are terminated by hydrogen atoms. The channel length L is either 9.91 or 15.1 nm; these values were chosen based on their potential future application in graphene-based electronic devices. The geometric structure of the AGNR is optimized using the O(N) method except the atoms belonging into leads.

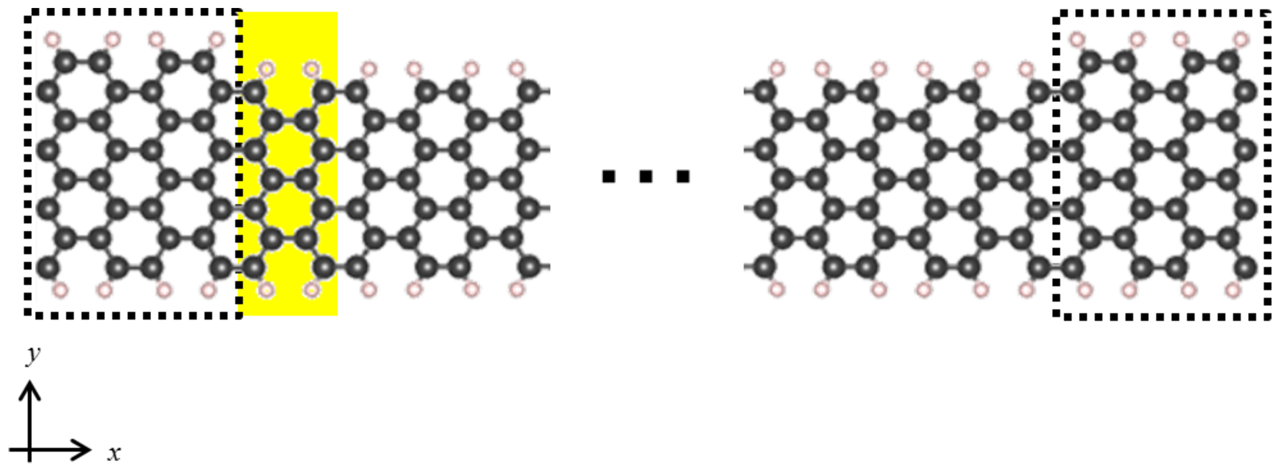

Fig. 4.3: A structural model of AGNRs for transport calculations. The yellow rectangle indicates a unit of AGNRs with $N = 7$. The length of the unit in the x-direction is 0.430 nm. The channels consist of 23 and 35 units for channel lengths (L) of 9.91 and 15.1 nm, respectively. The dotted regions represent the unit cell of the leads, which are made of AGNRs with $N = 8$ whose lattice parameter is uniaxially elongated by 1.86 % along the x-direction. The gray and white spheres represent carbon and hydrogen atoms, respectively.

4.3.2. SiO_2/Si

Figures 4.4(a) and 4.4(b) shows SiO_2/Si with OH-terminated (silanol) and O-terminated (siloxane) surfaces, respectively. The two models are chosen to correspond with the experiment of the electronic transport properties of graphene on SiO_2 [132]. Here, we explain the details of the O-terminated SiO_2/Si models shown in Fig. 4.4(b). The two layers of Si surface are oxidized. The SiO_2 thickness is 0.45 nm, which is also considered as an equivalent oxide thickness for future devices. The SiO_2 thickness from a few ten to a few hundred nm is commonly used in current experiments. The model in Fig. 4.5(a) shows a fully O-terminated surface structure without dangling bonds for a thin oxide film, as proposed in Ref. [140]. The model originally had 14 Si layers; however, we extracted six layers and terminated all edge Si atoms with hydrogen atoms, as shown in Fig. 4.5(b). We then optimized the geometry except the bottom two Si layers and confirmed that the model maintains the atomic structure with the errors in bond lengths within 1% and the bond angles equal to the original ones. The unit cell of the structure in the xz-plane is indicated by the dotted rectangle, which is also periodic along the y-direction. For transport calculations, the end of this structure is cut off on both sides in the x-direction and terminated by hydrogen atoms (Fig. 4.4). The models consist of 8.5 and 13.5 units of the original periodic SiO_2/Si structure for L = 9.91 and 15.1 nm, respectively. The entire geometry of the model is also optimized using the O(N) method except the bottom two Si layers.

The OH-terminated model of Fig. 4.4(a) is constructed by replacing each topmost oxygen atom in the O-terminated model of Fig. 4.4(b) with two OH groups. The silanol concentration of the model is 6.7 OH/nm^2, which almost corresponds to the highest concentration on the surface of amorphous silica [131] and the intermediate value between 9.6 OH/nm^2 in Ref. [135] and 4.8 OH/nm^2 in Ref. [136]. Only the atomic positions of the OH groups are relaxed. We identified the model in Fig. 4.4(a) as a metastable structure and confirmed that intense geometrical optimization easily overcomes the potential barriers; this causes the desorption of H_2O molecules, resulting in an O-terminated surface [Fig. 4.4(b)].

Figures 4.6(a) and 4.6(b) show the electronic structures of OH- and O-terminated SiO_2/Si, respectively. The calculated unit cell is indicated by the dotted rectangles in Fig. 4.4. Both the SiO_2/Si models have band gaps of E_g = 1.5 eV. For OH-terminated SiO_2/Si, some nearly flat band states are found in the band gap,

although the model has no dangling bonds; these states are localized around the OH groups on the SiO_2/Si surface. The localized states might be ascribed to the not fully relaxed geometry for the OH-terminated SiO_2/Si surface. Figure 4.6(c) shows the wave function of the highest occupied state, which is one of the nearly flat band states, at the Γ point. The electron affinity χ, which is defined as the energy difference between the vacuum level of the OH- or O-terminated side and the lowest unoccupied state, is 5.7 eV for the OH-terminated surface and 4.8 eV for the O-terminated surface. These values, E_g and χ, are closer to those of Si (E_g = 1.1 eV and χ = 4.05 eV) rather than those of SiO_2 (E_g ~9 eV and χ = 0.95 eV).

By comparing Fig. 4.1(d) with Fig. 4.6(b), we can find that the LUMO of the SiO_2/Si band is occupied by the electron transfer from the graphene to the substrate. Since the main amplitude of the LUMO state is distributed on the Si-layer as well as other states of SiO_2/Si around the Fermi level, the state is not expected to affect the transport properties of graphene.

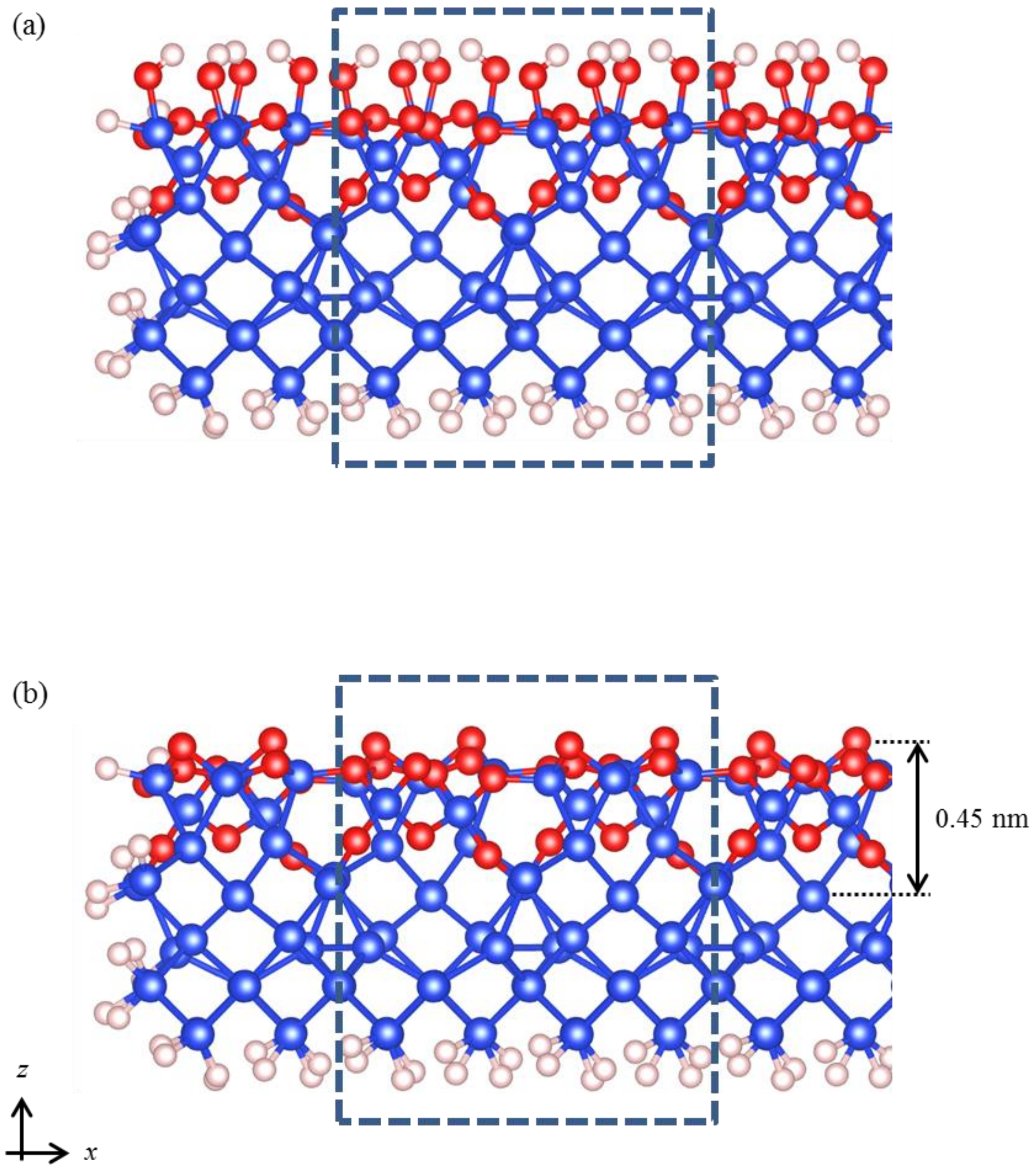

Fig. 4.4: Models of SiO_2/Si with (a) OH-terminated (silanol) and (b) O-terminated (siloxane) surfaces. The left edges are illustrated. The dashed rectangles indicate the unit cell of the periodic SiO_2/Si structure. The blue and red spheres represent silicon and oxygen atoms, respectively.

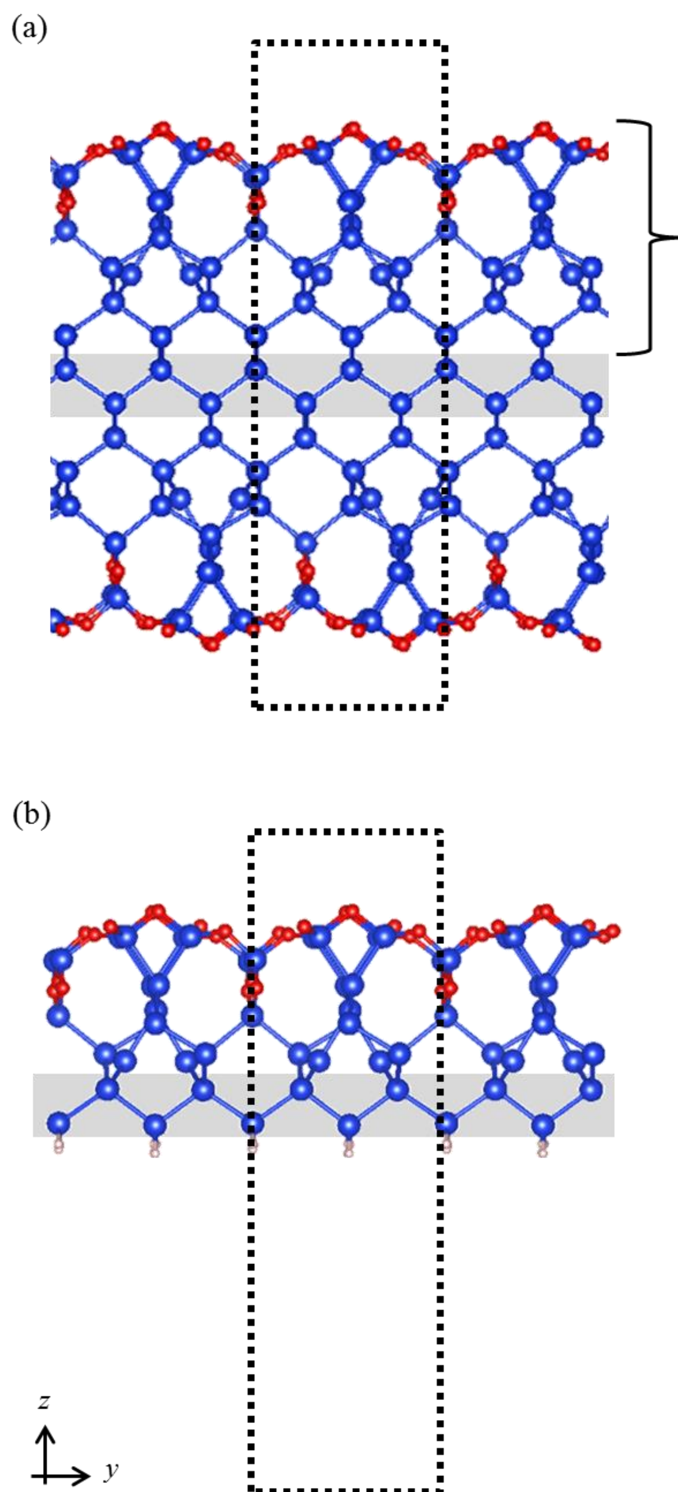

Fig. 4.5: (a) Our slab model of SiO_2/Si surface. (b) The original model of SiO_2-Si-SiO_2 in Ref. [139] whose geometry data is provided by Dr. T. Yamasaki. The dotted rectangles represent the unit cell. The gray areas indicate the fixed atom in the geometry optimization for each structure.

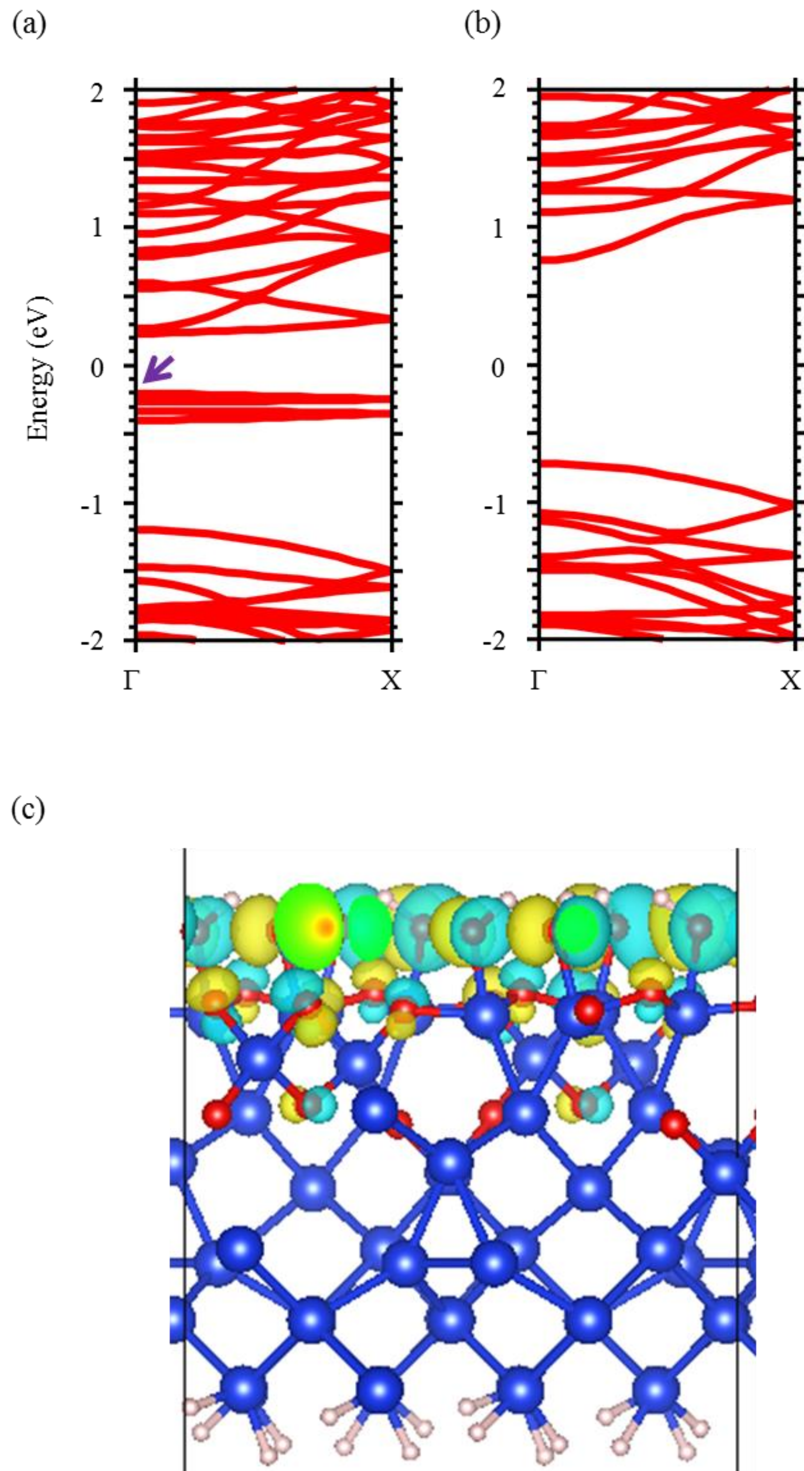

Fig. 4.6: Band structures of (a) OH- and (b) O-terminated SiO_2/Si for the unit cell of the periodic structures shown as the dashed rectangles in Fig. 4.4. The Fermi level of each SiO_2/Si model is set to 0 eV. (c) Wave function of the highest occupied state at the Γ point indicated by the arrow in (a). The yellow and cyan areas in the isosurfaces denote different signs of the states.

4.3.3. AGNRs on SiO_2/Si

AGNRs are adsorbed on SiO_2/Si (Fig. 4.7). The spacing between the AGNRs and SiO_2/Si was determined such that the total energy can be minimized in the model for the channel length of 9.91 nm. The geometries of the AGNRs and SiO_2/Si were fixed to the optimized structures. The lateral configuration is randomly selected based on no site selectivity [135, 136] for graphene/SiO_2 interfaces. The spacing between the AGNRs and the topmost atoms in SiO_2/Si is 0.25 nm for the OH-terminated surface and 0.31 nm for the O-terminated surface. The spacing for the OH-terminated surface corresponds to the silanol density. The obtained value is intermediate between the values reported in Ref. [135] (0.29 nm) and Ref. [136] (0.22 nm). For the O-terminated surface, the spacing is almost the same as those reported in Refs. [135] and [136], being employed in the model for L = 15.1 nm.

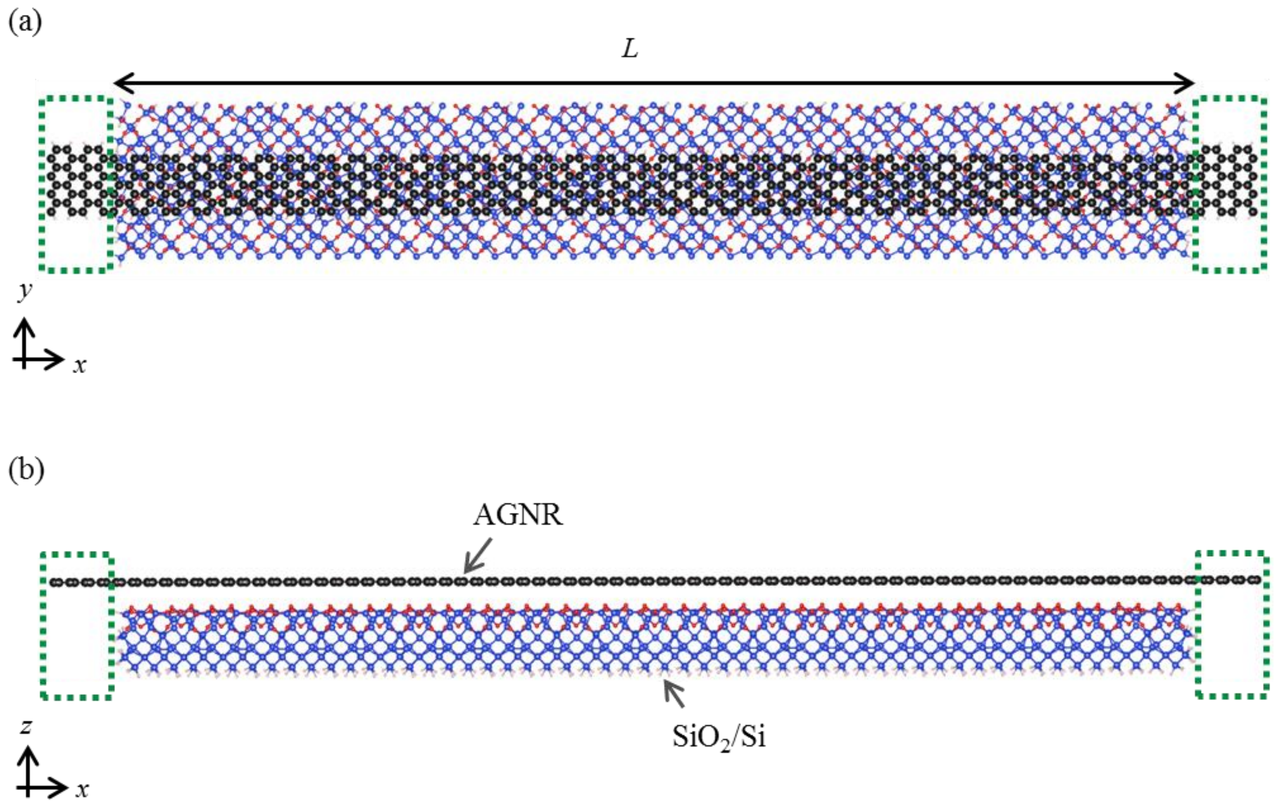

Fig. 4.7: A model of AGNRs on SiO_2/Si used for transport calculations (channel length L = 15.1 nm): (a) top and (b) side views. Although both sides in the transport direction (x) are connected to a semi-infinite AGNR in the actual calculations, only atoms in the center region are shown. In the y-direction, only atoms of the unit cell are shown, and they are actually repeated periodically. The details and enlarged figures of the AGNRs and SiO_2/Si are presented in Figs. 4.3 and 4.4, respectively.

4.4. Results and discussions

4.4.1. Effect of different SiO_2 surface terminations to transport properties

We investigate the transport properties of AGNRs with L = 9.91 nm on OH- and O-terminated SiO_2/Si. For comparison, we also investigate the transport properties of freestanding AGNRs. The electronic structure is determined self-consistently using the NEGF method. Figure 4.8(a) shows the transmission spectra obtained at a bias voltage of 0 V in a linear scale for AGNRs on OH- and O-terminated SiO_2/Si and freestanding AGNRs. All models have a transmission gap of 1.6 eV, which agrees with the energy band gap of AGNRs with N = 7. The transmission gaps for AGNRs on both SiO_2/Si are shifted upward by 0.7 eV. Despite the upward shift of the electronic states of AGNRs no doping effect was found on graphene using the fully O-terminated SiO_2 slab models [135, 136]. The hole doping to the graphene from our O-terminated SiO_2/Si model may originate from the electron affinity level of SiO_2/Si (4.8 eV) and the Fermi level of graphene (4.2 eV). For freestanding AGNRs, the transmission is increased from 2 to 6 at almost regular energy ranges, indicating the quantum conductance. However, for AGNRs on both SiO_2/Si, the energy range with a transmission of about 2 is narrower on the n side (around 1.6 eV). Moreover, the transmission shows discrete peak structures on the p side (below 0 eV). To highlight the difference in transmission gaps, the transmission spectra are also shown on a log scale in Fig. 4.8(b). The transmission spectra in the gap are very large for AGNRs on both SiO_2/Si compared with freestanding AGNRs, especially in the energy region just above 0 eV for the model with the OH-terminated surface.

To understand the transmission spectra, we first calculated the PDOS of each carbon atom in the AGNRs (Fig. 4.9). The lateral and vertical axes are the x axis in Fig. 4.7 and the energy relative to the Fermi level of the leads, respectively. For freestanding AGNRs [Fig. 4.9(c)], PDOS tails extend from the left side along the x axis; however, there is a clear gap of 1.6 eV in the middle of the channel around zero energy that corresponds well to the transmission gap. In contrast, for AGNRs on SiO_2/Si [Figs. 4.9(a) and 4.9(b)], multiple gap states are formed throughout the channel, especially on the p side for the OH-terminated surface. These states cause the multiple spiky transmission peaks in the gap and limits the tunneling transmission. We also observe Schottky barriers at the interface between the p-type semiconductor of AGNR channel and the

metallic graphene leads, as shown in Figs. 4.9(a) and 4.9(b). These Schottky barriers at both sides appear to form many discrete peaks in the transmission spectra on the *p* side.

To clarify the effect of the OH-terminated surface, we summarize the charge transfer for both of the SiO_2/Si models in Table 4.1, which shows the values for the unit cell of the periodic SiO_2/Si structure (shown as the dashed rectangles in Fig. 4.4) in the middle of the channel. For the geometry optimizations performed under periodic boundary conditions, the holes are injected into AGNRs from SiO_2/Si. The number of injected holes by the OH-terminated surface is larger than that by the O-terminated surface. For the transport calculations (NEGF), AGNRs are connected to the leads, and the holes in AGNRs are decreased. The OH groups have nearly flat band states within the band gap [Fig. 4.6(a)], which contribute the charge transfer. We also examine the PDOS of carbon atoms in AGNRs and oxygen atoms in the OH groups of the OH-terminated surface [Fig. 4.10(a)], that of carbon and oxygen atoms for the O-terminated surface [Fig. 4.10(b)], and that of a carbon atom of freestanding AGNRs [Fig. 4.10(c)]. We observe several PDOS peaks in the gaps of AGNRs for SiO_2 surfaces. In contrast, any peaks are not observed in the gap for freestanding AGNRs. Peak positions of the carbon atom correlate with those of the oxygen atoms, indicating a substantial interaction between the AGNRs and the SiO_2/Si surfaces despite the large spacing of about 0.3 nm. We also find large peaks around -0.5 eV and above 0 eV in the PDOS of the oxygen atoms in the OH groups; however, these peaks are not observed in the oxygen atoms of the O-terminated surface. These two peaks can be interpreted as the bonding and anti-bonding states originating from the interaction between the localized states around the OH groups in the unrelaxed geometry and the AGNRs. One of the peaks above the Fermi energy explains the larger transmission in the *p* side of the gap.

Here, we discuss the current characteristics shown in Fig. 4.11. Our transport calculations do not include actual gate structures or gate electric fields. We model a gate-controlled current by integrating the transmission in Fig. 4.8 over the energy range of 0.5 eV with respect to the central energy, which is corresponding to average of the chemical potential in the left and right leads, of the integration region. We assume that a back-gate voltage produces a uniform voltage drop on the entire AGNR, including source and drain leads. It should be noted that the voltage drop is not identical to the gate voltage because both the

voltages are related through the quantum capacitance of the AGNR and the gate electrodes. The eigen values of the AGNRs on SiO_2/Si are shifted downward by 0.7 eV from those of the pristine AGNRs. The currents are normalized to the AGNR width of 0.76 nm. The current in the *p* side (hole current) in AGNRs on both SiO_2/Si is smaller than that in freestanding AGNRs. The Schottky barriers for AGNRs on SiO_2/Si produce discrete transmission peaks on the *p* side, as described above; these discrete transmissions decrease the hole currents. However, the current in the *n* side (electron current) exhibits a steep rise for AGNRs on both SiO_2/Si. The steep increase in the electron current is ascribed to the narrower energy range with a transmission of 2 on the *n* side, as observed at around 1.6 eV in Fig. 4.8(b). The on/off current ratios for the AGNRs on OH- and O-terminated SiO_2/Si and the freestanding AGNRs are 10^4, 10^5 and 10^{13}, respectively. Here, we define the maximum and minimum currents in Fig. 4.11(b) as the on and off currents, respectively. Since on currents do not depend on the substrate environments, the off currents limit the on/off current ratios. The small ratios (large off currents) for AGNRs on both SiO_2/Si originate from the large transmissions in the gap, as shown in Fig. 4.8(b). The off current in the gap for the OH-terminated surface is larger than that of the O-terminated surface in the *p* side of the gap. This difference is ascribed to the large PDOS peaks on the *p* side for OH-terminated SiO_2/Si. These results may explain the degraded mobility of graphene sheets on SiO_2 with silanol groups [132].

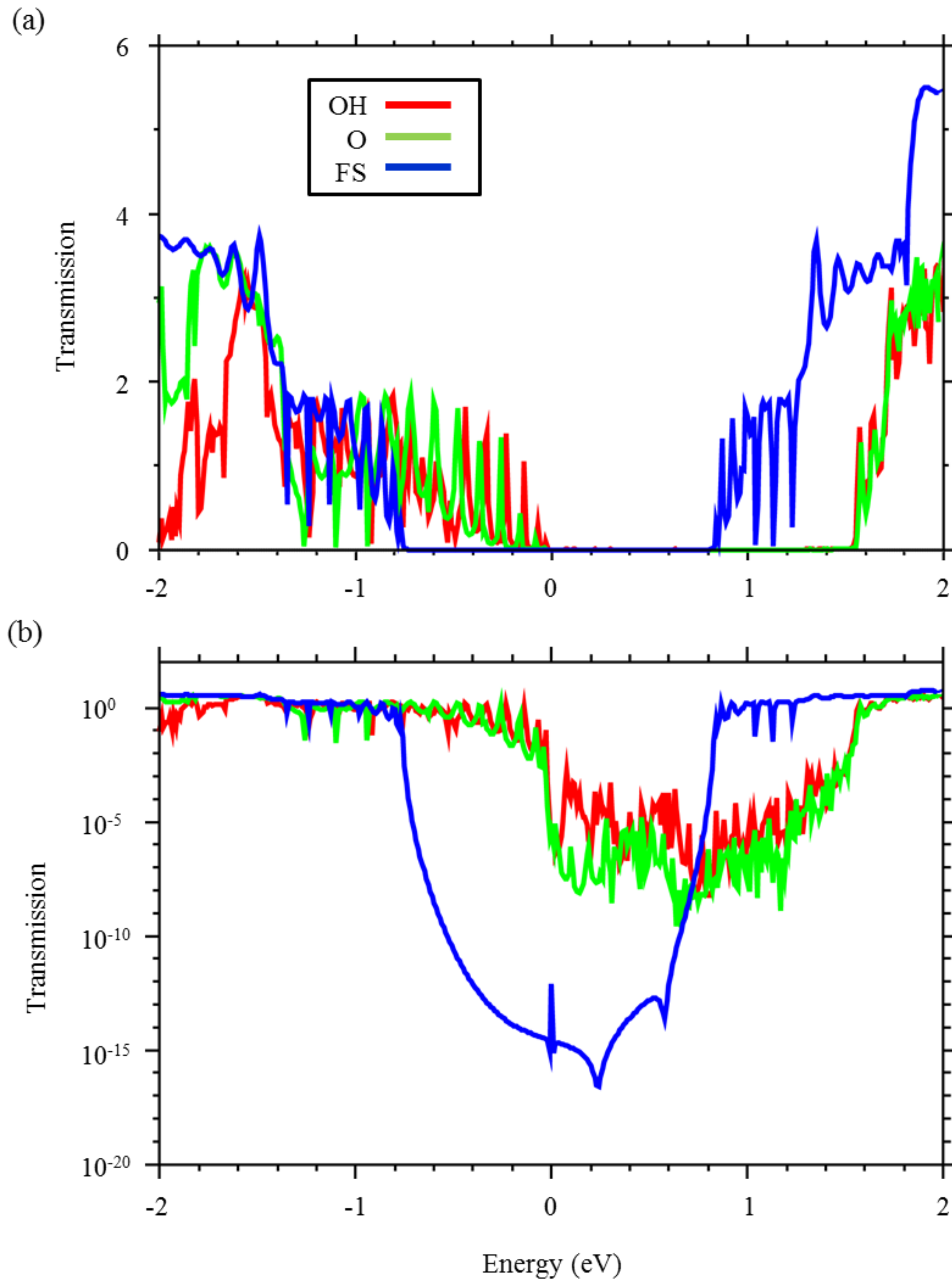

Fig. 4.8: Transmission spectra at a bias voltage of 0 V on (a) linear and (b) log scales for the AGNR on OH-terminated (OH) and O-terminated (O) SiO_2/Si, and the freestanding AGNR (FS) with the channel length L = 9.91 nm.

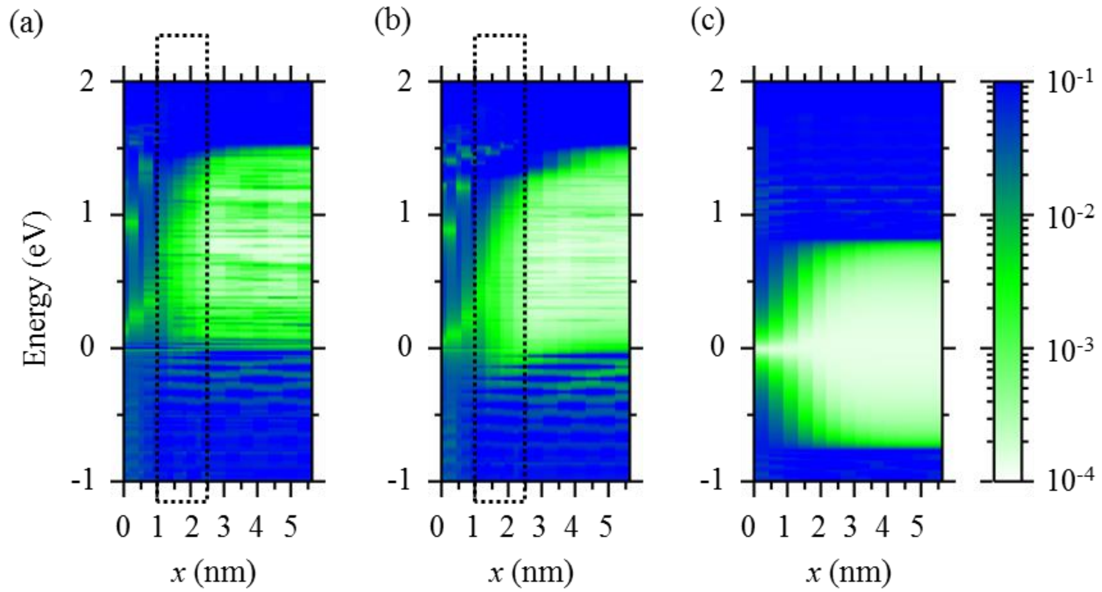

Fig. 4.9: PDOS of each carbon atom in AGNRs with the channel length L = 9.91 nm for three models: AGNRs on (a) OH- and (b) O-terminated SiO_2/Si, and (c) freestanding AGNRs. The lateral axis indicates the x position of the carbon atoms shown in Fig. 4.7. The left lead extends from x = 0 to x = 0.86 nm. Only the left half region is shown because of the symmetry between the left and right half regions. The vertical axis is the energy relative to the Fermi level of the leads. The right color bar shows the PDOS value. The Schottky barriers are found in the dotted regions in (a) and (b).

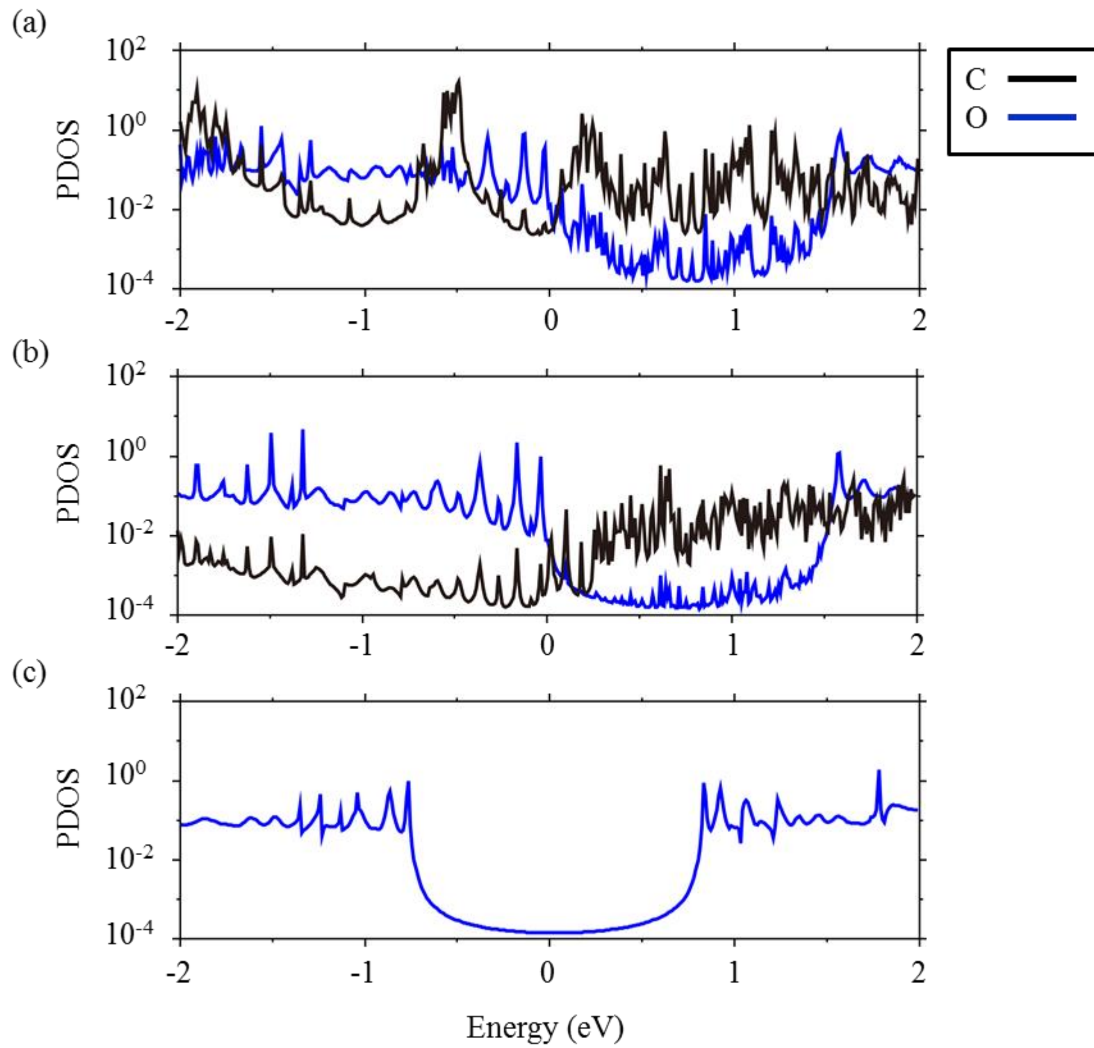

Fig. 4.10: PDOS (arb. unit) of a carbon (C) atom in AGNRs and an oxygen (O) atom of an OH group in the middle of the channel for AGNRs on (a) OH- and (b) O-terminated SiO_2/Si, and (c) freestanding AGNRs.

Table 4.1. Charge transfer in units of elementary charge for AGNRs on (a) OH- and (b) O-terminated SiO_2/Si. The methods O(N), NEGF, and ΔQ indicate geometric optimizations with periodic boundary conditions, transport calculations, and the difference between them, respectively. The values for the unit cell of the periodic SiO_2/Si structure, which is shown as the dashed rectangles in Fig. 4.4, in the middle of the channel are given.

Methods	O(N)		NEGF		ΔQ	
Model	(a)	(b)	(a)	(b)	(a)	(b)
AGNRs	+0.519	+0.223	+0.408	+0.108	−0.111	−0.115
OH group	−0.389	-	−3.251	-	−2.862	-
SiO_2/Si	−0.130	−0.223	+2.883	−0.111	+3.013	+0.112
Total	0.000	0.000	+0.040	−0.003	+0.040	−0.003

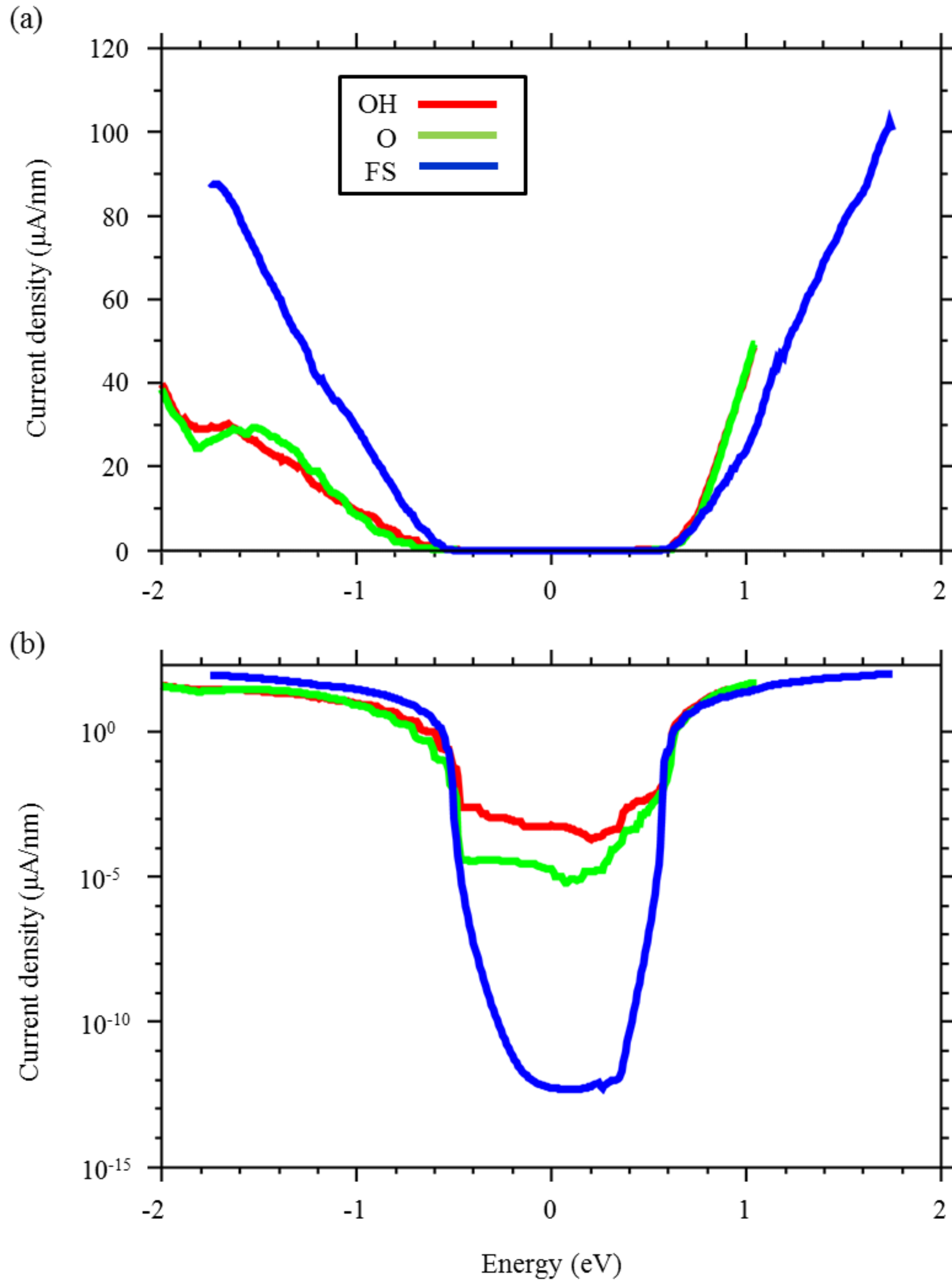

Fig. 4.11: Current densities on (a) linear and (b) log scales for AGNRs on OH- and O-terminated SiO_2/Si, and freestanding (FS) AGNRs. The transmission is integrated over the energy range of 0.5 eV to obtain the current for each energy value as the center. The current is normalized to the AGNR channel width of 0.76 nm. The energy values for AGNRs on O-terminated SiO_2/Si were shifted downward by 0.7 eV for comparison.

4.4.2. Channel length dependence of transport properties

We examine the transport properties of AGNRs on O-terminated SiO_2/Si and of freestanding AGNRs under two different channel lengths: L = 9.91 and 15.1 nm. Figures 4.12(a) and 4.12(b) shows the transmission spectra obtained at a bias voltage of 0 V of AGNRs on O-terminated SiO_2/Si and of freestanding AGNRs, respectively. We could not find any pronounced difference between the transmission spectra of the models with the two different channel lengths. The energy intervals of the discrete peaks due to the Schottky barriers are 0.11 eV for L = 9.91 nm and 0.07 eV for L = 15.1 nm. The interval is found to be inversely proportional to L. To highlight the difference in transmission gaps, the transmission spectra are also shown on a log scale in Fig. 4.12(c). The transmission spectra in the gap decrease exponentially with L for the freestanding AGNRs. The minimum values of the transmission are 10^{-16} for L = 9.91 nm and 10^{-24} for L = 15.1 nm. However, for AGNRs on O-terminated SiO_2/Si, the transmissions in the gap are independent of L, and multiple spiky peaks are also found in the gap, as discussed in Sec. 4.4.1.

To understand the transmission spectra, we discuss the PDOS of each carbon atom in the AGNRs in Fig. 4.9. The transmission gap can be seen as the potential barrier to tunneling from the left lead to the right lead. The height of the potential barrier is independent of L for freestanding AGNRs, because the band gap is also independent of L. However, the range of the potential barrier depends on L; the transmission gap decreases exponentially with increasing L for the freestanding AGNRs. In contrast, the simple assumption of the tunneling barrier is inapplicable to the AGNRs on O-terminated SiO_2/Si; gap states are observed throughout the channel, generating the spiky transmission peaks. As a result, the transmission in the gap does not depend on L. The interaction between the AGNRs and the SiO_2/Si surface affects the tunneling transmission regardless of L.

Figure 4.13 shows the current evaluated in the same way as in Sec. 4.4.1. The on currents do not depend on L for the both model, but the off currents depend on L only for the freestanding AGNRs. The on/off ratio of freestanding AGNRs increases to 10^{20} at L = 15.1 nm due to the exponential decay of the tunnel transmission within the gap. For AGNRs on O-terminated SiO_2/Si, however, the ratios of 10^5 are independent of L arising from L-independent transmission spectra within the gap. Thus, we have found that the SiO_2/Si

substrates limit the off currents of AGNRs.

Electrical transport experiments on sub-10-nm GNRs on SiO_2 have been performed [130]. The FET using GNRs with widths of 5 nm showed an on current of 2 μA and an on/off ratio of 10^5 at a source-drain voltage of 0.5 V, which is the same value as the integration region in our current calculations. Although the GNR width is still wider than in our calculations, the on/off ratio is consistent with our results. The smaller on current is mainly attributed to the contacts with actual metal leads.

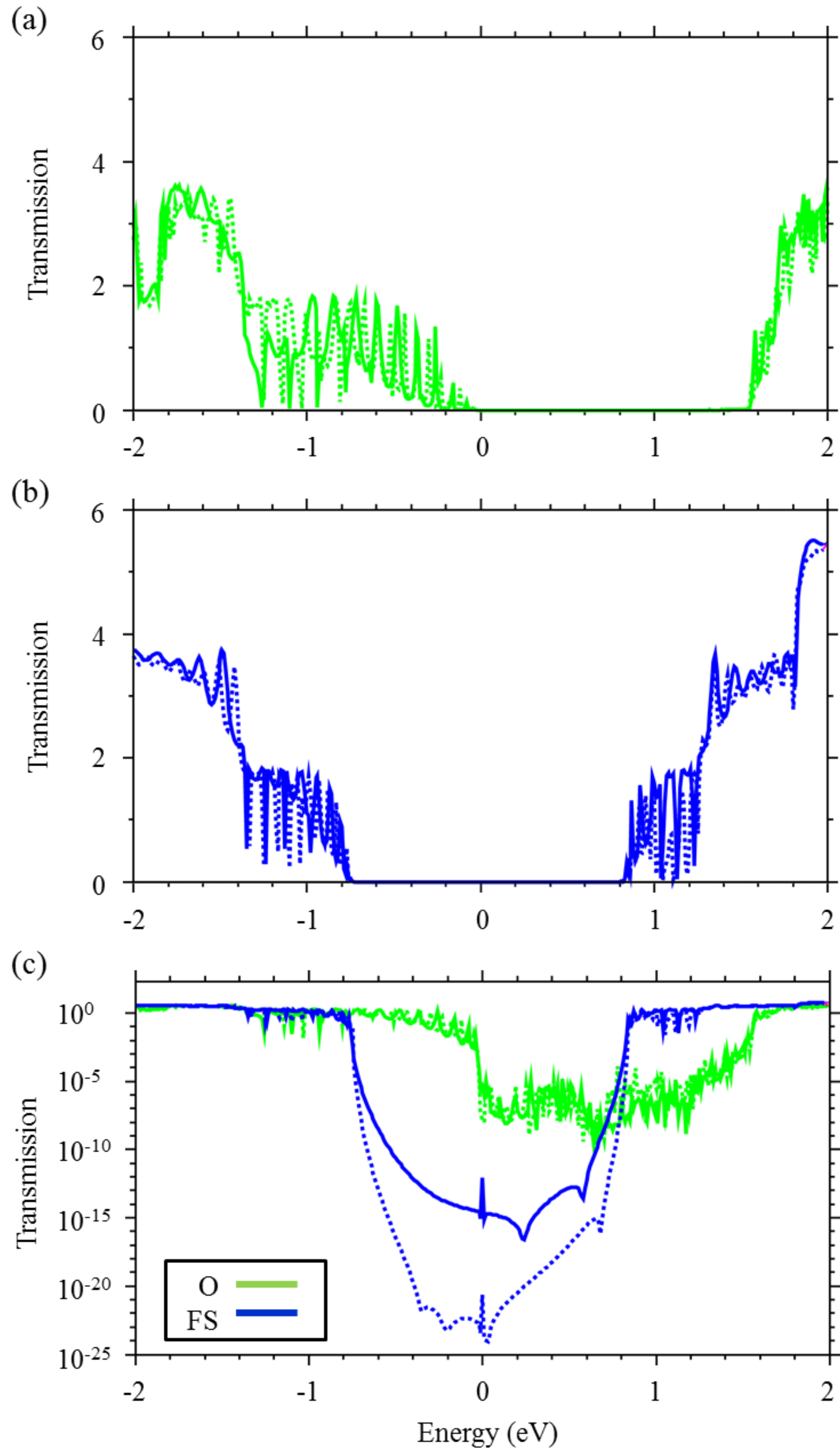

Fig. 4.12: Transmission spectra at a bias voltage of 0 V in (a, b) linear and (c) log scales for AGNRs on O-terminated SiO_2/Si (green lines) and freestanding AGNRs (blue lines). The solid and dotted lines indicate the transmissions for the models with L = 9.91 and 15.1 nm, respectively.

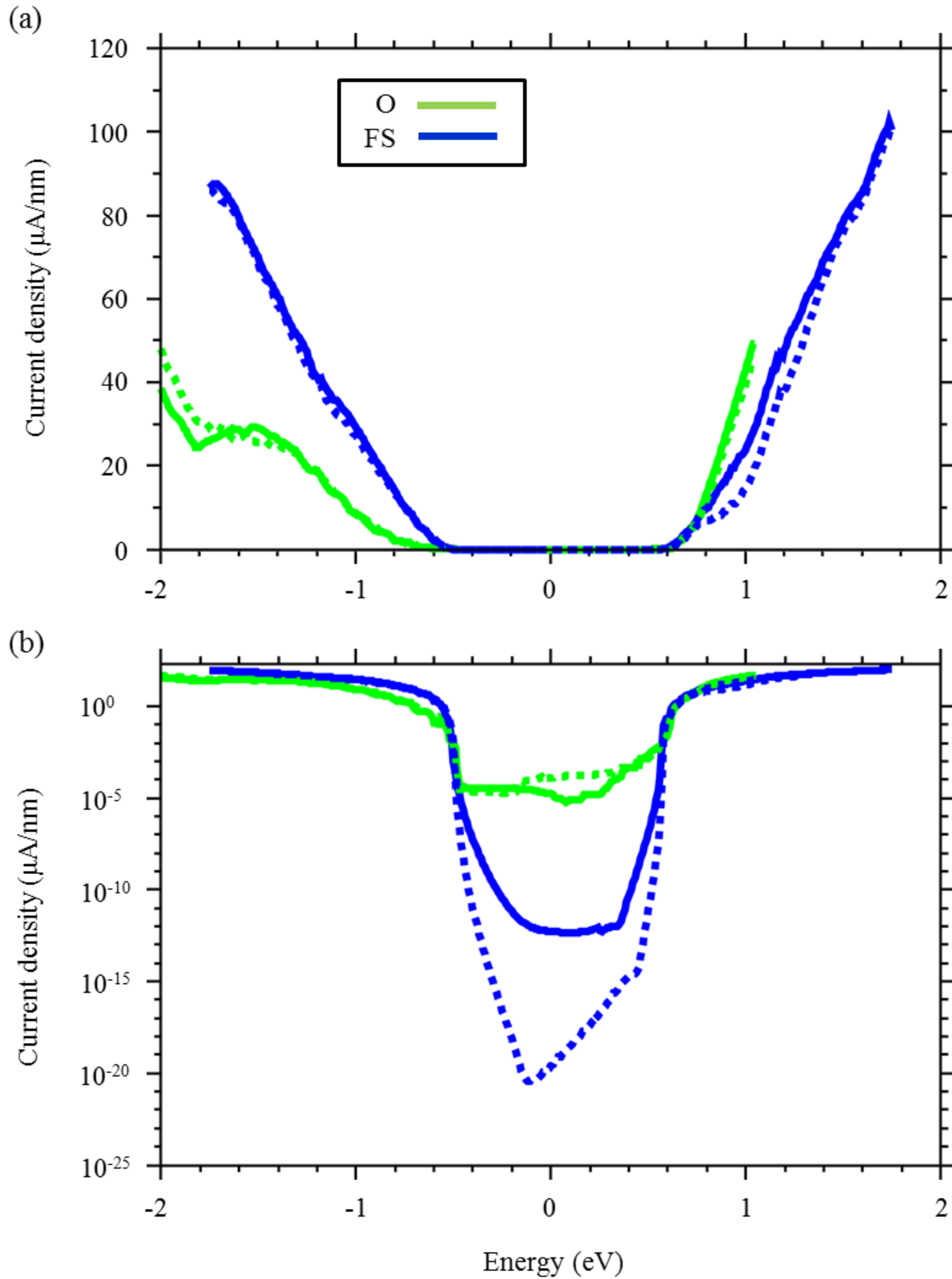

Fig. 4.13: Current densities on (a) linear and (b) log scales for AGNRs on O-terminated SiO_2/Si (green lines) and freestanding (blue lines) with channel lengths of 9.91 (solid) and 15.1 (dotted) nm. The transmission is integrated over the energy range of 0.5 eV to obtain the current for each energy value as the center. The current is normalized to the AGNR channel width of 0.76 nm. The eigen values of AGNRs on O-terminated SiO_2/Si were shifted downward by 0.7 eV for comparison.

4.5. Conclusions

We study the electronic transport properties of AGNRs with width corresponding with the number of C_2 dimer rows N = 7 adsorbed on OH-terminated (silanol) SiO_2/Si and O-terminated (siloxane) SiO_2/Si. We consider two AGNRs with two different channel lengths of 9.91 and 15.1 nm for the AGNRs on O-terminated SiO_2/Si. The AGNRs on both SiO_2/Si surfaces show *p*-type conduction. The number of injected holes by the substrate with OH is larger than that by the surface with O. The hole current in AGNRs on SiO_2/Si is smaller than that in freestanding AGNRs due to Schottky barriers. The off current in AGNRs on O-terminated SiO_2/Si is independent of channel length L due to the PDOS peaks within the band gap, although it exponentially decreases with increasing L for the freestanding AGNRs. The off current is even larger on the *p* side for the silanol SiO_2. The OH groups with the unrelaxed geometry cause nearly flat band states around the valence band maximum of the AGNRs and are considered to increase the charge transfer. Thus, we find that the gap states originating from the interaction between the AGNRs and the SiO_2/Si surface limits the off currents. We can conclude that for graphene-based electronic devices, it is important to control the surface structure of the insulating substrates.

Chapter 5. Summary

One atom thickness of graphene is one of the greatest advantages utilizing them in nanoscale devices. It simultaneously leads to problems arising from the fragility of the fundamental properties of graphene against the other foreign materials, such as metal electrodes, and insulating substrates. In this thesis, we study electronic transport properties of AGNRs bridged between two metal electrodes and supported on SiO_2/Si using first-principles calculations.

We investigate the electronic transport properties of the hybrid structures of graphene/metal electrodes. The models consist of AGNRs width up to 12 nm bridged between two metal electrodes of Au and Ti. For the Au electrodes, the current densities sensitively depend on the ribbon width, even though the width reaches 12 nm. We have found that the energy band structure and the symmetry of π state of the graphene play the important role for determining the transport properties because of the weak interaction between the π state of graphene and the *s* state of the Au surface. These results suggest that the width of graphene materials should be precisely controlled for designing the graphene-based FET devices with Au electrodes. For the Ti electrodes, in sharp contrast, the strong π-d coupling modifies the electronic structure of graphene and substantially enhances the electron transfer through the Ti-graphene contact. As the results, the current densities for the Ti electrodes are about 10 times as large as those for the Au electrodes in the AGNRs with the ribbon width of about 12 nm. We have found that the transport properties of the hybrid structures of graphene/metal electrodes decisively depend on the amount of the hybridization between them.

We also investigate the electronic transport properties of the hybrid structures of graphene/insulators. The models consist of AGNRs on OH- and O-terminated SiO_2/Si with two channel lengths (L = 9.91 and 15.1 nm). The AGNRs on both SiO_2/Si surfaces show the *p*-type transport property. The hole current in AGNRs on SiO_2/Si is smaller than that in the freestanding GNRs due to Schottky barriers. The off current for AGNRs on O-terminated SiO_2/Si is independent of channel length L due to the PDOS peaks within the band gap. The off current is even larger on the *p* side for the OH-terminated SiO_2. The OH groups have localized states around the valence band maximum of the AGNRs and are considered to increase the charge transfer. The gap

states originating from the interaction between the AGNRs and the SiO_2/Si surface limits the off currents. Thus, for graphene-based electronic devices, it is important to control the surface structure of the insulating substrates.

To obtain further theoretical insight for realizing the graphene-based electronic devices, we should employ more realistic model of the interface including effects of contaminations, annealing processes, and surface morphologies. In the future, we would like to develop the comprehensive understanding on the interfaces associated with the 2D thin film materials.

Bibliography

[1] K. S. Novoselov, A. K. Geim, A. V. Morozov, D. Jiang, Y. Zhang, S. V. Dubonos, I. V. Grigorieva, and A. A. Firsov, Science 306, 666 (2004).

[2] A. Nagashima, N. Tejima, Y. Gamou, T. Kawai, and C. Oshirna, Phys. Rev. Lett. 75, 3918 (1995).

[3] K. Watanabe, T. Taniguchi and H. Kanda, Nature Mat. 3, 404 (2004).

[4] A. Fleurence, R. Friedlein, T. Ozaki, H. Kawai, Y. Wang, and Y. Yamada-Takamura, Phys. Rev. Lett. 08, 245501 (2012).

[5] T. Li and G. Galli, J. Phys. Chem. C 111, 16192 (2007).

[6] A. Splendiani, L. Sun, Y. Zhang, T. Li, J. Kim, C. -Y. Chim, G. Galli, and F. Wang, Nano Lett. 10, 1271 (2010).

[7] B. Radisavljevic, A. Radenovic, J. Brivio, V. Giacometti1 and A. Kis, Nature Nanotech. 6, 147 (2011).

[8] H. W. Kroto, J. R. Heath, S. C. O'Brien, R. F. Curl, and R. E. Smalley, Nature 318, 162 (1985).

[9] S. Iijima, Nature 354, 56 (1991).

[10] M. S. Dresselhaus and G. Dresselhaus, Adv. Phys. 30, 139 (1981).

[11] J. W. McClure, Phys. Rev. 104, 666 (1956).

[12] J. C. Slonczewski and P. R. Weiss, Phys. Rev. 109, 272 (1958).

[13] T. Ando and T. Nakanishi, J. Phys. Soc. Jpn. 67, 1704 (1998).

[14] T. Ando, T. Nakanishi, and R. Saito, J. Phys. Soc. Jpn. 67, 2857 (1998).

[15] T. Nakanishi and T. Ando, J. Phys. Soc. Jpn. 68, 561 (1999).

[16] K. S. Novoselov, Z. Jiang, Y. Zhang, S. V. Morozov, H. L. Stormer, U. Zeitler, J. C. Maan, G. S. Boebinger, P. Kim, and A. K. Geim, Science 315, 1379 (2007).

[17] M. I. Katsnelson, K. S. Novoselov, and A. K. Geim, Nature Phys. 2, 620 (2006).

[18] A. F. Young and P. Kim, Nature Phys. 5, 222 (2009).

[19] K. S. Novoselov, A. K. Geim, S. V. Morozov, D. Jiang, M. I. Katsnelson, I. V. Grigorieva, S. V. Dubonos, and A. A. Firsov, Nature, 438, 197 (2005).

[20] Y. Zhang, Y.-W. Tan, H. L. Stormer, and P. Kim, Nature, 438, 201 (2005).

[21] K. S. Kim, Y. Zhao, H. Jang, S. Y. Lee, J. M. Kim, K. S. Kim, J. –H. Ahn, P. Kim, J. –Y. Choi, and B. H. Hong, Nature 457, 706 (2009).

[22] D. Kondo, S. Sato, K. Yagi, N. Harada, M. Sato, M. Nihei, and N. Yokoyama, Appl. Phys. Express 3, 025102 (2010).

[23] X. S. Li, W. W. Cai, J. H. An, S. Kim, J. Nah, D. X. Yang, R. Piner, A. Velamakanni, I. Jung, E. Tutuc, S. K. Banerjee, L. Colombo, and R. S. Ruoff, Science 324, 1312 (2009).

[24] A. Reina, X. Jia, J. Ho, D. Nezich, H. Son, V. Bulovic, M. S. Dresselhaus, and J. Kong, Nano Lett. 9, 30 (2009).

[25] Q. Yu, J. Lian, S. Siriponglert, H. Li, Y. P. Chen, and S. –S. Pei, Appl. Phys. Lett. 93, 113103 (2008).

[26] C. Berger, Z. Song, T. Li, X. Li, A. Y. Ogbazghi, R. Feng, Z. Dai, A. N. Marchenkov, E. H. Conrad, P. N. First, and W. A. de Heer, J. Phys. Chem. B 108, 19912 (2004).

[27] K. V. Emtsev, A. Bostwick, K. Horn, J. Jobst, G. L. Kellogg, L. Ley, J. L. McChesney, T. Ohta, S. A. Reshanov, J. Rohrl, E. Rotenberg, A. K. Schmid, D. Waldmann, H. B. Weber, and T. Seyller, Nature Mater. 8, 203 (2009).

[28] H. Hibino, H. Kageshima, F. Maeda, M. Nagase, Y. Kobayashi, and H. Yamaguchi, Phys. Rev. B 77, 075413 (2008).

[29] C. Riedl, C. Coletti, T. Iwasaki, A. A. Zakharov, and U. Starke, Phys. Rev. Lett. 103, 246804 (2009).

[30] A. J. Van Bommel, J. E. Crombeen, and A. Van Tooren, Surf. Sci. 48, 463 (1975).

[31] T. Ohta, A. Bostwick, T. Seyller, K. Horn, and E. Rotenberg, Science 313, 951 (2006).

[32] N. Harada, M. Ohfuti, and Y. Awano, Appl. Phys. Exp. 1, 024002 (2008).

[33] S. Y. Zhou, G.-H. Gweon, A. V. Fedorov, P. N. First, W. A. De Heer, D.-H. Lee, F. Guinea, A. H. Castro Neto, and A. Lanzara, Nat. Mater. 6, 770 (2007).

[34] F. Varchon, R. Feng, J. Hass, X. Li, B. N. Nguyen, C. Naud, P. Mallet, J.-Y. Veuillen, C. Berger, E. H. Conrad, and L. Magaud, Phys. Rev. Lett. 99, 126805 (2007).

[35] Y. –J. Kang, J. Kang, and K. J. Chang, Phys. Rev. B 78, 115404 (2008).

[36] J. Bai, X. Zhong, S. Jiang, Y. Huang, and X. Duan, Nat. Nanotech. 5, 190 (2010).

[37] H. Jippo, M. Ohfuchi, and C. Kaneta, Phys. Rev. B 84, 075467 (2011).

[38] M. Y. Han, B. Özyilmaz, Y. Zhang, and P. Kim, Phys. Rev. Lett. 98, 206805 (2007).

[39] J. Bai, X. Duan, and Y. Hung, Nano Lett. 9, 2083 (2009).

[40] D. V. Kosynkin, A. L. Higginbotham, A. Sinitskii, J. R. Lomeda, A. Dimiev, B. K. Price, and J. M. Tour: Nature 458, 872 (2009).

[41] L. Jiao, L. Zhang, X. Wang, G. Diankov, and H. Dai, Nature 458, 877 (2009).

[42] J. Cai, P. Ruffieux, R. Jaafar, M. Bieri, T. Braun, S. Blankenburg, M. Muoth, A. P. Seitsonen, M. Saleh, X. Feng, K. Mullen, and R. Fasel, Nature 466, 470 (2010).

[43] K. Nakada, M. Fujita, G. Dresselhaus, and M. S. Dresselhaus, Phys. Rev. B 54, 17954 (1996).

[44] V. Barone, O. Hod, and G. E. Scuseria, Nano Lett. 6, 2748 (2006).

[45] Y. –W. Son, M. L. Cohen, and S. G. Louie, Phys. Rev. Lett. 97, 216803 (2006).

[46] L. Yang, C. –H. Park, Y. –W. Son, M. L. Cohen, and S. G. Louie, Phys. Rev. Lett. 99, 186801 (2007).

[47] M. Born and R. Oppenheimer, Annalen der Physik 389, 457 (1927).

[48] P. Hohenberg and W. Kohn, Phys. Rev. 136, B864 (1964).

[49] W. Kohn and L. J. Sham, Phys. Rev. 140, A1133 (1965).

[50] D. M. Ceperley and B. J. Alder, Phys. Rev. Lett. 45, 566 (1980).

[51] J. P. Perdew, K. Burke, and M. Ernzerhof, Phys. Rev. Lett. 77, 3865 (1996).

[52] M. C. Payne, M. P. Teter, D. C. Allan, T. A. Arias, J. D. Joannopoulus, Rev. Mod. Phys. 64, 1045 (1992).

[53] T. Ozaki, Phys. Rev. B 67, 155108 (2003).; http://www.openmx-square.org/.

[54] O. F. Sankey and D. J. Niklewski, Phys. Rev. B 40**,** 3979 (1989).

[55] P. Ordejon, E. Artacho, J. M. Soler, Phys. Rev. B 53, R10441 (1996).

[56] J. M. Soler, E. Artacho, J. D. Gale, A. Garcia, J. Junquera, P. Ordejon, and D. Sanchez-Portal, J. Phys.:Condens. Matter 14**,** 2745 (2002).

[57] B. Delly, J. Chem. Phys. 92, 508 (1990).

[58] T. Ozaki and H. Kino, Phys. Rev. B **69**, 195113 (2004).

[59] G. B. Bachelet, D. R. Hamann, and M. Schluter, Phys. Rev. B **26**, 4199 (1982).

[60] N. Troullier and J. L. Martins, Phys. Rev. B **43**, 1993 (1991).

[61] I. Morrison, D. M. Bylander, and L. Kleinman, Phys. Rev. B 47, 6728 (1993).

[62] T. Ozaki, K. Nishio, and H. Kino, Phys. Rev. B 81, 035116 (2010).

[63] R. Landauer, IBM J. Res. Dev. 1, 223 (1957).

[64] M. Büttiker, Y. Imry, R. Landauer, and S. Pinhas, Phys. Rev. B 31, 6207 (1985).

[65] S. Datta, "Quantum Transport: Atom to Transistor", Cambridge University Press (2005).

[66] M. P. Lopez Sancho, J. M. Lopez Sancho, J. M. L. Sancho, and J. Rubio, J. Phys. F: Met. Phys. 15, 851 (1985).

[67] T. Ozaki, Phys. Rev. B 75, 035123 (2007).

[68] G. Giovannetti, P. A. Khomyakov, G. Brocks, V. M. Karpan, J. van den Brink, and P. J. Kelly, Phys .Rev. Lett. 101, 026803 (2208).

[69] K. Pi, K. M. McCreary, W. Bao, Wei Han, Y. F. Chiang, Yan Li, S.-W. Tsai, C. N. Lau, and R. K. Kawakami, Phys. Rev. B 80, 075406 (2009).

[70] B. Huard, N .Stander, J. A. Sulpizio, and D. Goldhaber-Gordon, Phys. Rev. B 78, 121402 (2008).

[71] F. Xia, V. Perebeinos, Y. –M. Lin, Y. Wu, and P. Avouris, Nature Nanotech. 6, 179 (2011).

[72] R. Nouchi, M. Shiraishi, and Y. Suzuki, Appl. Phys. Lett. 93, 152104 (2008).

[73] K. Nagashio and A. Toriumi, Jpn. J. Appl. Phys. 50, 070108 (2011).

[74] K. Nagashio, T. Nishimura, K. Kita, and A. Toriumi, Appl. Phys. Lett. 97, 143514 (2010).

[75] J. A. Robinson, M. LaBella, M. Zhu, M. Hollander, R. Kasarda, Z. Hughes, K. Trumbull, R. Cavalero, and D. Snyder, Appl. Phys. Lett. 98, 053103 (2011).

[76] R. Nouchi, T. Saito, and K. Tanigaki, J. of Appl. Phys. 111, 084314 (2012).

[77] R. Ifuku, K. Nagashio, T. Nishimura, and A. Toriumi, Appl. Phys. Lett. 103, 033514 (2013).

[78] A. Venugopal, L. Colombo, and E. M. Vogel, Appl. Phys. Lett. 96, 013512 (2010).

[79] E. Watanabe, A. Conwill, D. Tsuya, and Y. Koide, Diamond & Related Materials 24, 171 (2012).

[80] S. M. Song, J. K. Park, O. J. Sul, and B. J. Cho, Nano Lett.12, 3887 (2012).

[81] J. T. Smith, A. D. Franklin, D. B. Farmer, and C. D. Dimitrakopoulos, ACS Nano 7, 3661 (2013).

[82] T. Moriyama, K. Nagashio, T. Nishimura, and A. Toriumi, J. Appl. Phys. 114, 024503 (2013).

[83] W. S. Leong, H. Gong, and J. T. L. Thong, ACS Nano 8, 994 (2014).

[84] P. A. Khomyakov, G. Giovannetti, P. C. Rusu, G. Brocks, J. van den Brink, and P. J. Kelly, Phys. Rev. B 79, 195425 (2009).

[85] Q. Ran, M. Gao, X. Guan, Y. Wang, and Z. Yu, Appl. Phys. Lett. 94, 103511 (2009).

[86] Y. Takagi and S. Okada, Jpn. J. Appl. Phys. 51, 100203 (2012).

[87] Y. Gamo, A. Nagashima, M. Wakabayashi, M. Terai, and C. Oshima, Surf. Sci. 374, 61 (1997).

[88] G. Bertoni, L. Calmels, A. Altibelli, and V. Serin, Phys. Rev. B 71, 075402 (2004).

[89] M. Fuentes-Cabrera, M. I. Baskes, A. V. Melechko, and M. L. Simpson, Phys. Rev. B 77, 035405 (2008).

[90] C. Gong, G. Lee, B. Shan, E. M. Vogel, R. M. Wallace, and K. Cho, J. Appl. Phys. 108, 123711 (2010).

[91] Z. Xu, and M. J. Buehler, J. Phys.: Condens. Matter 22, 485301 (2010).

[92] M. Vanin, J. J. Mortensen, A. K. Kelkkanen, J. M. Garcia-Lastra, K. S. Thygesen, and K. W. Jacobsen, Phys. Rev. B 81, 081408(R) (2010).

[93] I. Hamada and M. Otani, Phys. Rev. B 82, 153412 (2010).

[94] P. A. Khomyakov, A. A. Starikov, G. Brocks, and P. J. Kelly, Phys. Rev. B 82, 115437 (2010).

[95] A. Varykhalov, M. R. Scholz, T. K. Kim, and O. Rader, Phys. Rev. B82, 121101(R) (2010).

[96] Y. Takagi and S. Okada, Jpn. J. Appl. Phys. 51, 085102 (2012).

[97] S. M. Kozlov, F. Viñes, and A. Görling, J. Phys. Chem. C 13, 116 (2012).

[98] M. Andersen, L. Hornekær, and B. Hammer, Phys. Rev. B 86, 085405 (2012).

[99] M. Hasegawa, K. Nishidate, T. Hosokai, and N. Yoshimoto, Phys. Rev. B 87, 085439 (2013).

[100] K. Toyoda, K. Nozawa, N. Matsukawa, and Shigeo Yoshii, J. Phys. Chem. C 16, 117 (2013).

[101] S. Barraza-Lopez, M. Vanevic´, M. Kindermann, and M. Y. Chou, Phys. Rev. Lett. 104, 076807 (2010).

[102] S. Barraza-Lopez, M. Kindermann, and M. Y. Chou, Nano Lett. 12, 3424 (2012).

[103] S. Barraza-Lopez, J. Comp. Electron 12, 145 (2013).

[104] J. Maassen, W. Ji. And H. Guo, Appl. Phys. Lett. 97, 142105 (2010).

[105] I. Deretzis, G. Fiori, G. Iannaccone, and A. La Magna, Phys. Rev. B 82, 161413(R) (2010).

[106] K. Stokbro, M. Engelund, and A. Blom, Phys. Rev. B 85, 165442 (2012).

[107] S. Yamacli, Comp. Mat. Sci. 81, 607 (2014).

[108] B. Ma, C. Gong, Y. Wen, R. Chen, K. Cho, and B. Shan, J. Appl. Phys. 115, 183708 (2014).

[109] T. Kaneko, and T. Ohno, Jpn. J. Appl. Phys. 53, 05FD07 (2014).

[110] H. Liu, H. Kondo, and T. Ohno, Phys. Rev. B 86, 155434 (2012).

[111] H. Liu, H. Kondo, and T. Ohno, J. Chem. Phys. 139, 074703 (2013).

[112] T. V. T. Duy and T. Ozaki, Comp. Phys. Comm. 185, 153 (2014).

[113] T. V. T. Duy and T. Ozaki, Comp. Phys. Comm. 185, 777 (2014).

[114] S. G. Louie, S. Froyen and M. L. Cohen, Phys. Rev. B 26, 1738 (1982).

[115] S. G-. Gil, A. García, N. Lorente, and P. Ordejón, Phys. Rev. B79, 075441 (2009).

[116] T. Hayashi, Y. Morikawa, and H. Nozoye, J. Chem. Phys. 114, 7615 (2001).

[117] C. Kittel, Introduction to Solid State Physics, 7th ed., Wiley, New York, 1996.

[118] D. Connetable, J. Huez, E. Andreiu, and C. Mijoule, J. Phys.: Condens. Matter 23, 405401 (2011).

[119] G. Verite, F. Willaime, and C. C. Fu, Solid State Phenom. 129, 75 (2007).

[120] L. Li, S. Reich, and J. Robertson, Phys. Rev. B 72, 184109 (2005).

[121] Y. Baskin and L. Meyer, Phys. Rev. 100, 544 (1955).

[122] J. Sławińska, P. Dabrowski, and I. Zasada, Phys. Rev. B 83, 245429 (2011).

[123] Z. Klusek, P. Dabrowski, P. Kowalczyk, W. Kozlowski, W. Olejniczak, P. Blake, M. Szybowicz, and T. Runka, Appl. Phys. Lett.95, 113114 (2009).

[124] http://www.itrs.net/Links/2013ITRS/Home2013.htm.

[125] A. D. Franklin, M. Luisier, S. –J. Han, G. Tulevski, C. M. Breslin, L. Gignac, M. S. Lundstrom, and W. Haensch, Nano Lett. 12, 758 (2012).

[126] E. J. H. Lee, K. Balasubramanian, R. T. Weitz, M. Burghard, and K. Kern, Nat. Nanotechnol.3, 486 (2008).

[127] K. I. Bolotin, K. J. Sikes, Z. Jiang, M. Klima, G. Fudenberg, J. Hone, P. Kim, and H. L. Stormer, Solid State Commun. 146, 351 (2008).

[128] X. Du, I. Skachko, A. Barker, and E. Andrei, Nature Nanotech. 3, 491 (2008).

[129] M. –W. Lin, C. Ling, Y. Zhang, H. J. Yoon, M. M. -C. Cheng, L. A. Agapito, N. Kioussis, N. Widjaja1 and Z. Zhou, Nanotechnology 22, 265201 (2011).

[130] X. Li, X. Wang, L. Zhang, S. Lee, H. Dai, Science 319, 1229 (2008).

[131] L. T. Zhuravlev, Colloid Surf. A 173, 1 (2009).

[132] K. Nagashio, T. Yamashita, T. Nishimura, K. Kita, and A. Toriumi, J. Appl. Phys. 110, 024513 (2011).

[133] M. Z. Hossain, Appl. Phys. Lett. 95, 143125 (2009).

[134] P. Shemella and S. K. Nayak, Appl. Phys. Lett. 94, 032101 (2009).

[135] N. T. Cuong, M. Otani, and S. Okada, Phys. Rev. Lett. 106, 106801 (2011).

[136] C. -J. Yang, S. -J. Huang, and C. -L. Kuo, Appl. Phys. Lett. 101, 253107 (2012).

[137] T. Ozaki, Phys. Rev. B 74, 245101 (2006).

[138] H. Jippo, and M. Ohfuchi, J. Appl. Phys. 113, 183715 (2013).

[139] Y. Lu, and J. Guo, Nano Res 3, 189 (2010).

[140] T. Yamasaki, K, Kato, and T. Uda, Phys. Rev. Lett. 91, 146102 (2003).